

JYU DISSERTATIONS 235

Maciej Slupecki

The Fast Interaction Trigger for the ALICE Upgrade



UNIVERSITY OF JYVÄSKYLÄ
FACULTY OF MATHEMATICS
AND SCIENCE

JYU DISSERTATIONS 235

Maciej Slupecki

The Fast Interaction Trigger for the ALICE Upgrade

Esitetään Jyväskylän yliopiston matemaattis-luonnontieteellisen tiedekunnan suostumuksella
julkisesti tarkastettavaksi
kesäkuun 12. päivänä 2020 kello 12.

Academic dissertation to be publicly discussed, by permission of
the Faculty of Mathematics and Science of the University of Jyväskylä,
on June 12, 2020 at 12 o'clock noon.



JYVÄSKYLÄN YLIOPISTO
UNIVERSITY OF JYVÄSKYLÄ

JYVÄSKYLÄ 2020

Editors

Timo Sajavaara

Department of Physics, University of Jyväskylä

Päivi Vuorio

Open Science Centre, University of Jyväskylä

Copyright © 2020, by University of Jyväskylä

Permanent link to this publication: <http://urn.fi/URN:ISBN:978-951-39-8186-0>

ISBN 978-951-39-8186-0 (PDF)

URN:ISBN:978-951-39-8186-0

ISSN 2489-9003

Preface

The work presented in this dissertation has been done at the Department of Physics of the University of Jyväskylä during the years 2014–2020. First and foremost, I would like to express my gratitude to my supervisor, Doc. Wladyslaw Trzaska. Simple words cannot express how much his support affected my professional development since the time we first met, back in 2008. I would like to thank him for his patient guidance, countless vivid discussions and to-the-point comments. The reviewers of this work: Prof. Pietro Antonioli and Prof. Panja-Riina Luukka deserve thanks for their valuable input, which helped to finalise the thesis.

Furthermore, my thanks go to members of the ALICE FIT collaboration, especially to Dr. Jesus Guillermo Contreras Nuno, Dr. Varlen Grabski, Dr. Tatiana Karavicheva, Dr. Yury Melikyan, Dr. Solangel Rojas and Dr. Dmitry Serebryakov for reading this manuscript and for providing valuable comments and corrections. I would also like to also mention Mr. Dmitry Finogeev and thank him for sharing his insight on the complex hardware issues, including details on readout electronics design. I would like to thank Dr. Alla Maevskaya for hints on using the ALICE software framework. I would like to express my thanks to the whole ALICE research group in Jyväskylä, especially to Dr. Sami Räsänen and Dr. DongJo Kim for a decent supply of motivation and pointing my research in the right direction. My thanks go to Ms. Heidi Rytönen, Mr. Oskari Saarimäki. I would also like to mention Prof. Ian Bearden, Dr. Andrea Dainese, Dr. Jacek Otwinowski and thank them for the help they provided. A separate thanks is due for Dr. Timo Enqvist, Dr. Pasi Kuusiniemi, Dr. Tomi Räihä, Dr. Juho Sarkamo, Dr. Kai Loo, Mr. Jari Joutsenvaara, Mr. Antto Virkäjärvi and other members of the CUPP team. The opportunities and atmosphere you created was crucial in shaping my professional development even before I started my PhD studies. Throughout the years I have been privileged to work with many brilliant, enthusiastic and helpful people, that are not explicitly mentioned here. My thanks go to them as well.

Finally, I would like to thank my family. My fiancée, for her support and patience in this demanding time. Thank you for reminding me that there is life besides work. My parents, for their guidance, answering my never-ending questions and for the never-waning pool of encouragement that I could always draw upon. My sister for proofreading and providing occasional stress relief with humorous anecdotes.

Jyväskylä, May 2020
Maciej Shupecki

Author	Maciej Slupecki Department of Physics University of Jyväskylä Finland
Supervisor	Adj. Prof. Wladyslaw Henryk Trzaska Department of Physics University of Jyväskylä Finland
Reviewers	Adj. Prof. Pietro Antonioli Department of Physics and Astronomy University of Bologna Italy Prof. Panja-Riina Luukka Lappeenranta-Lahti University of Technology Finland
Opponent	Prof. Agnieszka Zalewska Institute of Nuclear Physics Polish Academy of Sciences Krakow, Poland

Acknowledgements

The author expresses gratitude for the financial support to the rector of the University of Jyväskylä during the majority of the study period and to the Helsinki Institute of Physics for securing the funding for the final year.

Abstract

The Fast Interaction Trigger for the ALICE Upgrade

Maciej Śtupecki

As a part of the preparations for the LHC Run 3 and 4, the ALICE experiment at CERN is undertaking a thorough upgrade of the setup. In particular, all ALICE subsystems have to cope with the increased interaction rate of 50 kHz in Pb–Pb and up to 1 MHz in pp collisions. Compared to Run 2, this is up to two orders of magnitude more collisions. Although the solution for the majority of ALICE detectors is to switch to a continuous readout, several of the older systems (TRD, CPV, HMPID, EMCAL, DCAL, and PHOS) would still need an external trigger or a wakeup signal.

The Fast Interaction Trigger (FIT) will generate a minimum-bias and a multiplicity trigger with the maximum latency below 425 ns. It will also measure the collision time with a resolution of $\lesssim 40$ ps and serve as the main ALICE luminometer, providing direct, real-time feedback to the LHC for the beam tuning. In the offline analysis, FIT will aid in the reconstruction of the vertex position, assess forward particle multiplicity, centrality, and event plane, and will be used for the study of diffractive physics at forward rapidity.

FIT consists of three subsystems: a fast Cherenkov detector array using MCP-PMTs as photosensors, a large scintillator ring employing a novel light collection system, and a scintillator-based Forward Diffractive Detector. In this thesis, the detector design is presented and verified. The description of detector components, along with the key test results of individual components, component assemblies, and of the full detector simulation are presented and discussed. They show that FIT has been optimized to fulfill all of the required functionalities and operate efficiently within the imposed constraints.

Contents

1. Introduction	1
1.1. Standard Model	1
1.2. Quantum Chromodynamics	3
1.3. Quark-gluon plasma	5
1.4. Experimental observables in heavy-ion physics	7
1.5. ALICE	9
1.6. Author's contribution	12
1.6.1. Publications	14
1.6.2. Other activities	15
2. ALICE at the LHC	18
2.1. The LHC and infrastructure	18
2.1.1. The LHC as a collider	19
2.1.2. The beam structure, stability and focusing	20
2.1.3. The beam life cycle	22
2.1.4. The LHC operation during Run 1 and Run 2	24
2.1.5. Operational parameters of the LHC in Run 3	24
2.2. ALICE highlights in LHC Run 1 and 2	26
2.3. The ALICE upgrade	27
2.3.1. Motivation	27
2.3.2. Detector and system upgrades	28
2.4. Particle collisions – parameters and properties	29
2.4.1. The importance of energy and luminosity for physics	29
2.4.2. The pseudorapidity	32
2.4.3. Impact parameter and centrality	33
2.4.4. Reaction plane and anisotropic flow	34
2.5. Background sources	36
2.5.1. Introduction	36
2.5.2. Detector- and electronics-specific noise	36
2.5.3. Cosmic rays	37
2.5.4. Natural radioactivity and material activation	38
2.5.5. Beam halo and beam-gas events	38

2.5.6. Ultraperipheral collisions (UPC) and QED pair production	39
3. The Fast Interaction Trigger (FIT)	41
3.1. Motivation	41
3.1.1. ALICE trigger distribution	41
3.1.2. Minimum-bias trigger detector	43
3.1.3. Multiplicity trigger detector	45
3.1.4. Luminometer	46
3.1.5. Expected contribution to offline analyses	47
3.2. General design concept	48
3.2.1. Forward location	52
3.2.2. Environmental considerations	52
3.2.3. Comparison with FIT predecessors from Run 2	56
3.3. The FT0	58
3.3.1. Motivation for detector module R&D at CERN PS	59
3.3.2. Selection and optimization of the photosensor	61
3.3.3. Cross-talk tests	64
3.3.4. Choice of radiator material	67
3.3.5. Optimization of quartz radiators	68
3.3.6. Further tests of oversized radiator	70
3.3.7. Angular response	72
3.3.8. Response to the particles travelling in the opposite direction	73
3.3.9. Optical grease	75
3.3.10. Contribution of the entrance window to signal amplitude	75
3.3.11. Gain scan	76
3.3.12. Simulated occupancy and dynamic range of FT0 pixels	78
3.3.13. Ageing of photosensors	79
3.3.14. Assembly and batch tests of XP85002/FIT-Q	85
3.3.15. Real-life tests at ALICE	99
3.3.16. Sensitivity to magnetic field	101
3.3.17. Laser calibration system (LCS)	105
3.3.18. Final detector design	107
3.4. The FV0	110
3.4.1. Motivation for an upgrade	111
3.4.2. General design	112
3.4.3. Detector R&D	114
3.4.4. Plastic scintillator	117
3.4.5. Light collection system	118
3.4.6. Photosensor	124

3.4.7. Laser calibration system	125
3.5. The Forward Diffractive Detector (FDD)	126
3.5.1. General detector layout	126
3.5.2. Plastic scintillator and light collection system	127
3.5.3. Photosensor	129
3.5.4. Laser calibration system	130
3.6. Detector performance	131
3.6.1. Simulation environment	131
3.6.2. Centrality resolution	131
3.6.3. Event plane resolution	135
3.6.4. QED background study	136
4. Summary and outlook	140
A. List of presentations and publications	142

1. Introduction

As a civilization, we are both proud of and dependent on our technological advancements. They make our lives easier, safer and generally more enjoyable. They have become an inseparable component of our culture. To continue developing at such a high rate, we need to push the frontiers of knowledge further and further. This is the role of fundamental research, which forms the basis for any technological advancements leading to practical applications. The fundamental research aims at improving our understanding of the natural phenomena and developing theoretical models capable of their description and a further prediction.

1.1. Standard Model

One of the branches of science performing fundamental research is the particle physics. It studies the nature of the smallest constituents of matter and energy and their interactions. Currently, the leading theory of particle physics is the Standard Model (SM).

According to the SM the Universe is made of a limited number of elementary particle species: 12 fermions (spin $\frac{1}{2}$), their antiparticles, 12 force-carrying gauge bosons (spin 1) and one scalar Higgs boson (spin 0). Among fermions, there are 6 quarks grouped by their mass into 3 generations: up (u) and down (d), charm (c) and strange (s), top (t) and bottom (b). The remaining fermions can be similarly classified into: electron (e) and electron neutrino (ν_e), muon (μ) and muon neutrino (ν_μ), tau (τ) and tau neutrino (ν_τ). The SM recognizes three fundamental forces or interactions, mediated by gauge bosons: electromagnetic interaction carried by photon (γ), weak interaction – W^+ , W^- and Z bosons, strong interaction – eight types of gluons. The existence of the scalar Higgs boson, responsible for the generation of masses, has recently been verified experimentally [3, 4]. See Figure 1.1 for details about the SM elementary particles and the interactions. The one outstanding shortcoming of the SM is that it does not include the fourth fundamental force – the gravity. Therefore, the link between small, particle-scale and large-scale astrophysical phenomena is missing.

Elementary particles in the Standard Model

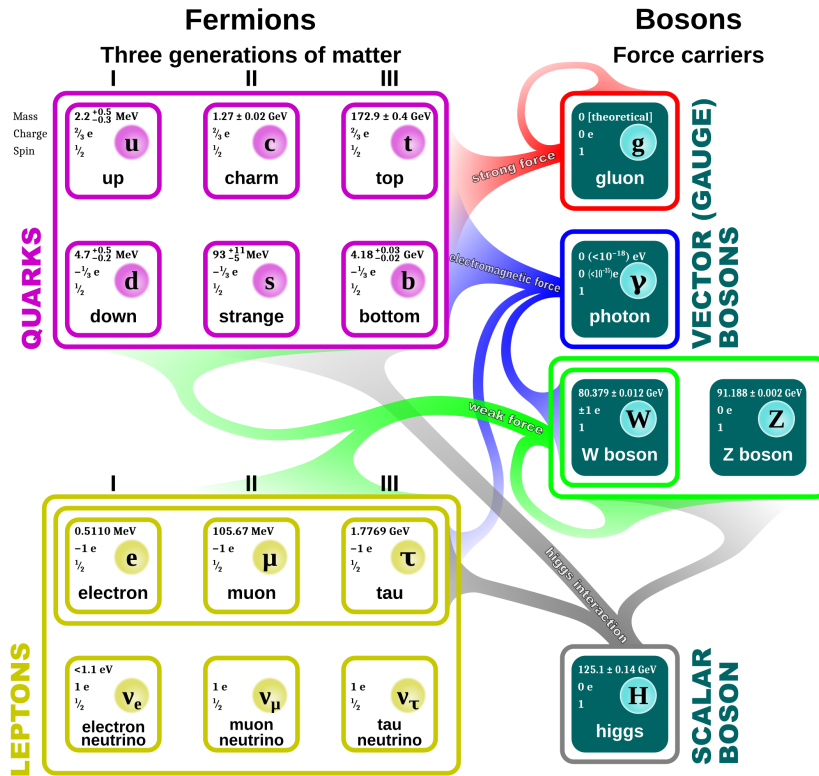


Figure 1.1.: Elementary particles of the Standard Model and the corresponding interactions. The particle masses are taken from [1, 2]

The quark content of the SM is supported by two observations [5]. Firstly, in high energy particle collisions, a multitude of different hadrons is detected. Their existence and properties are explained if they are composed of a group of three quarks (baryons) or quark-antiquark pairs (mesons). Considering quarks are fermions and they have to adhere to the Pauli exclusion principle, 6 quark flavours, together with two possible spin states and several radial excitation states of each quark can be combined to form thousands of final-state particles. These combinations include uud and udd triplets, that correspond to the most commonly recognized hadrons: the proton (p) and the neutron (n) respectively.

Secondly, the presence of the spin $\frac{1}{2}$ point-like partons inside nucleons is indicated by measurements of inelastic scattering of electrons off nucleons. The spectra are best modelled by partons, which behave as free particles within the volume of a nucleon [6]. Additionally, in e^-p^+ deep inelastic scattering experiments well-collimated jets of particles are observed [7, 8]. The natural explanation involves the scattering of a single parton from the collision region, which then forms a subsequent directional particle shower.

1.2. Quantum Chromodynamics

Despite such a good agreement of the quark model with experimental observations, no single free quark has ever been observed [9, 10]. This can be explained by introducing the strong interaction described by the Quantum Chromodynamics (QCD) as the main force affecting the behaviour of quarks. According to the QCD, the attractive strong force is caused by the exchange of gluons. Gluons are spin 1, massless particles found inside hadrons, binding them together. Like quarks, they are coloured, and together they are called partons [11]. Unlike quarks, they carry zero baryon number. Their existence is confirmed by triple-jet particle collision events, in which two jets originate from a quark-anti-quark pair and the source of the remaining jet is a gluon [12–14].

To explain why quarks are commonly bound into (i) quark-anti-quark, (ii) three-quark or (iii) three-anti-quark system an additional *colour charge* quantum number has been introduced. There are three colours: red, green, blue and their anti-colours. Quarks can only form neutral net colour bound states (colour singlets), i.e., baryons consist of red, green and blue quark, while mesons are formed by any combination of colour-anticolour quark pairs. This property is called colour confinement [15]. Introduction of the additional colour quantum number [16, 17]

is justified by the experimental observation of baryons, which otherwise could not exist due to the Pauli exclusion principle. For example, $\Delta^{++}(1232)$ consists of three same-flavour quarks uuu , which is the only combination of (u, d, s) , that were considered in the early quark model, which makes up the double charge. Its spin is $\frac{3}{2}$, that can only be the result of 3 aligned spins of each u quark. Without colours, all three constituent quarks would have the same set of quantum numbers and could not form the baryon.

While quarks carry one of only three available colour charges, gluons carry one of eight colour-anticolour charge combinations. In principle, there are nine possible pairs of colour-anticolour charges, but the one representing colour singlet has to be removed. If gluons in colour-singlet state existed, they would not be confined [14]. This implies they could be observed as free particles, which has not been the case.

Because gluons are strong force mediators and colour charge-carriers they can interact both with themselves and with other gluons [18]. A short-range strong interaction between two quarks can be represented as a direct exchange of gluons. However, when the distance between quarks increases, so does the probability of two-gluon interaction or gluon self-interaction. This branching effect complicates calculations to such extent that at distance scales $\gtrsim 0.5$ fm practical QCD results rely on numerical simulations [5]. They are based on the QCD equations that are formulated for regions of the discretely-divided space and time [19,20]. They form a 4-dimensional grid or lattice. However, this approach is quite limited, because such a simulation is very demanding in terms of computer resources [1]. Still, up to date, quite a few significant results were obtained with the help of lattice QCD, though with non-negligible numerical uncertainties.

The potential between a quark-antiquark pair at the distance r can be described as [5,21]:

$$V(r) = -\frac{A(r)}{r} + Kr \quad (1.1)$$

The first term resembles the Coulomb law and dominates at short distances, while the second one means that at large distances the potential increases linearly with the distance. It is worth to note the A is not constant, but mildly depends on r [5]:

$$A(r) \sim -\frac{1}{\ln(r)} \quad (1.2)$$

Altogether, such a potential results in two outstanding properties of the strong interaction. Firstly, at small distances quarks behave as almost free particles. This property is called the asymptotic freedom [15, 22]. Secondly, the linear rise of potential at larger distances means, that it is not possible to effectively separate them. An attempt to separate two quarks would lead to the rise of potential, which would eventually reach a point, at which it would become more energetically favourable to create a quark-antiquark pair in between. The created pair would act then as a sink or source, reducing the potential [5].

1.3. Quark-gluon plasma

Despite quarks are confined in the ordinary matter, they are predicted to behave as free particles if certain combination of high pressure, density and energy is applied. They form a strongly interacting soup of free quarks and gluons called the Quark-Gluon Plasma (QGP) [23, 24]. The QGP is a distinct state of matter, which can exist only at extremely high temperatures or densities. Many cosmological questions [25] draw our attention to the very early Universe – to about the time when the QGP was the dominant medium (between a picosecond and a microsecond after the Big Bang [26, 27]) and its properties affected the development of the Universe. For instance, quantum fluctuations, that are believed to have appeared earlier during the inflation [28], may have led to the formation of large-scale structures [29], like galaxies and clusters. After the inflation these fluctuations needed to propagate through the QGP, so it is important to study the properties of the QGP in order to improve our understanding of the present large-scale structure of the universe and its development. The moment of transition between the QGP and the hadronized matter [30] is of equal interest. This phase transition is the only experimentally accessible one in a quantum field theory, so it is an excellent proving ground for its verification.

During the phase transition from hadronized matter to the QGP the mean distance between interactions of quarks and gluons shortens as the temperature is raised. Upon reaching the critical temperature ($T_c \sim 150 - 175$ MeV for $\mu_B \rightarrow 0$) [31] they become screened against long-range interactions [32], i.e., partons are no longer bound to hadrons, but can be described as free (deconfined) particles. The resulting state of matter behaves like a near ideal liquid [33, 34]. On the other hand, if the mean distance between quarks were shorter the strong interaction would essentially disappear, as a result of the asymptotic freedom, and they would interact only weakly. Such a mean distance can be expressed

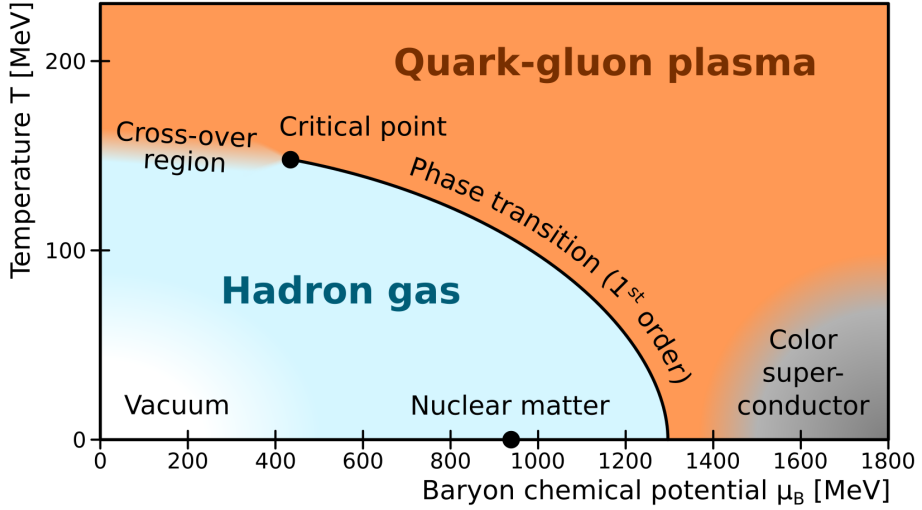


Figure 1.2.: The phase diagram of known matter. The control parameters are the temperature T and the chemical potential μ . The figure is based on data from [5, 36]

as the baryon chemical potential (μ_B). It is the variable of choice since it holds the thermodynamically relevant meaning of a rate of free energy change with respect to the change in the number of particles within the system. The chemical potential refers in this case to the baryon number, which is a conserved quantity in the QCD. It can be calculated as the difference between numbers of baryons and antibaryons in the system.

It is worth to note that because the QCD is a relativistic theory the rest mass of particles should be taken into account. Because each quark flavour has different mass it is associated with its own chemical potential. However, in the first-order approximation these multiple dimensions can be omitted and it can be assumed there exists only one chemical potential related to the three lightest quarks: up, down and strange [35]. The masses of these three quark flavours are lower than the QGP formation temperature, which means only they contribute to its properties at an equilibrium. Out of the three lightest quarks the strange quark is the heaviest one, so it needs to be treated carefully close the QGP phase transition temperature.

The two major control parameters needed to construct a phase diagram describing the QGP phase transition are identified as temperature and chemical potential. The sketch of such a phase diagram is shown in Figure 1.2. The two known phases are the hadronic gas, within which the ordinary nuclear matter is located, and the QGP. At some non-zero chemical potential, there is a critical point, above which the first-order phase transition is expected. For the lower chemical potential the phase transition occurs as a crossover [37] due to non-identical quark masses. This is the region probed by ultrarelativistic heavy-ion collisions. The higher the collision energy the more quark-antiquark pairs are produced. In the pair production process, the net baryon number is not changed, so these experiments probe the phase diagram region, where chemical potential is close to zero. On the other hand, in lower-energy collisions, the quarks inside the colliding nuclei constitute a significant fraction of detected matter and their baryon number becomes significant globally. Therefore, such collisions probe the region of the larger chemical potential, but at a lower temperature. Efforts are made to probe lower baryon-number regions of the phase diagram by Beam Energy Scan programme at RHIC [36], by the NA61/SHINE at CERN [38], and by future facilities, i.e., CBM at FAIR [39] and MPD at NICA [40]. The aim of these experiments is to search for the critical point presented in Figure 1.2.

In the phase diagram, there can be more theoretically possible phases. As an example, the region with the high chemical potential and the relatively low temperature could be a colour superconductor [41]. An experimental confirmation of such additional phases must rely on studying large astrophysical objects, like neutron stars [42,43] or black holes [44], where matter is squeezed by gravity overcoming the strong force to reach necessary densities. Construction of an experiment capable of probing this region in a laboratory testbench seems impossible. The QGP is different in this respect as it can be studied in the well-controlled laboratory conditions.

1.4. Experimental observables in heavy-ion physics

The only known way to produce the QGP artificially is through high-energy particle collisions. Colliding heavy ions (HI) is advantageous compared to light ions or protons because such collisions on average form a larger system, which translates into a larger amount of the produced QGP [34,45]. It is only possible to produce minute and extremely short-lived portions of the QGP, which quickly expand, lose the required energy density and transform back into the hadronic

matter.

In heavy-ion collisions, the number of experimental observables is very limited. At best the yields of identified particles as a function of the transverse momentum, the azimuth angle and the pseudorapidity are available. These observables can be used to calculate the luminosity, which is needed for the determination of cross sections. Invariant mass distributions may also be derived.

Other derived quantities, that can serve as probes of the QGP formation [46] have been found. One of the phenomena, indicating the QGP is formed in heavy-ion collisions, is the flow. Initially, the radial flow was identified as the change of a slope in the momentum spectra of a given particle species [47]. Then the azimuthal anisotropies of detected particles were observed. If a collision happens to be non-central, then the collision region is not spherical, but rather almond-shaped. And such is the initial shape of the expanding QGP droplet. Hydrodynamical flow converts the spatial anisotropies into momentum anisotropies, which translate directly into azimuthal anisotropies of outgoing particles [34, 47]. The experimental observation of the angular distribution of particles consistent with this picture shows that a droplet of low-viscosity liquid is formed in heavy-ion collisions [48–50].

The second relevant phenomenon, that indicates the early-state droplet is strongly-interacting, is the jet quenching [51, 52]. In case a pair of heavy quark-antiquark is produced early after a collision, the momentum conservation stipulates that two jets of approximately equal total momenta should emerge on the opposite sides. It, however, assumes both jets are subject to similar further interactions when traversing the medium between their point of creation and detection. It is likely, however, that the jets originate from the periphery of a collision region. In this case, one of the jets may escape the collision region almost immediately, while the other jet traverses most of the medium created during the collision. Only if the medium is transparent for a heavy quark, the other jet would emerge unaffected. In fact, it has been observed that the other jet is quenched [33, 53]. This means that the medium, which it had to pass through, is strongly-interacting and during this transition, the jet's momentum is transferred to the medium and spread across a large number of less energetic particles.

The yields of quarkonia provide additional information on the formation and properties of the QGP [54]. Heavy quarkonia can be produced either in a primary collision or at a later stage via recombination. Additionally, their signatures can be suppressed by the interaction with the QGP medium in the fashion similar to jets. These three mechanisms influence the final yields of the charmonia and the

bottomia, that carry information about all of the underlying physics, especially about the QGP medium interactions. Therefore, the formation of the QGP can be inferred from the observed increased production of strange quark pairs [55], ultimately detected as single- or multi-strange hadrons. It has been shown that mainly the gluon component is responsible for this strangeness enhancement [56] and in the QGP there is an abundance of free gluons available.

Finally, electromagnetic signals, i.e., photons and dileptons are insensitive to strong interaction and so they can be used to probe the initial stages of the QGP formation [57], its evolution and some of the properties, like the temperature of the fireball [58].

Historically strangeness enhancement was the first signal indicating the formation of the QGP [59]. Then jet quenching and anisotropic flow was observed. Presently, while ALICE, as well as STAR and PHENIX perform detailed studies of these three basic phenomena, the focus is slowly shifting towards the precise measurement of the last two groups of observables, i.e., the heavy quarkonia, leptons and photons. The interest in the heavy-ion community is best shown in the physics motivation behind the ALICE Upgrade [60]. It concentrates on the significant increase of the statistics and on implementing detector upgrades allowing to measure leptons and study charm and beauty also at very low transverse momenta, which were out of reach until now. The forward photon and electron studies are considered for another upgrade in the further future [61,62].

1.5. ALICE

Particle colliders are machines capable of accelerating charged particle beams and directing them to move along trajectories that lead particles to collide with each other. The Large Hadron Collider (LHC) is the largest element in a complex of particle accelerators at CERN, located in Geneva region in Switzerland. During its Run 2 operation, it has routinely achieved the highest particle beam energy in the world of 6.5 TeV/ c for proton beam and 2.51 TeV/ c for lead ions, which translates into the maximum collision energies of 13 TeV/ c and 5.02 TeV/ c respectively. Along the LHC there are four intersection points, where particles can collide. Complex detector systems are built around them.

A Large Ion Collider Experiment (ALICE) [64] has its detector at the LHC interaction point 2. A photograph of the opened experiment is shown in Figure 1.3. The experiment is dedicated to study the QGP, by analysing the properties of par-

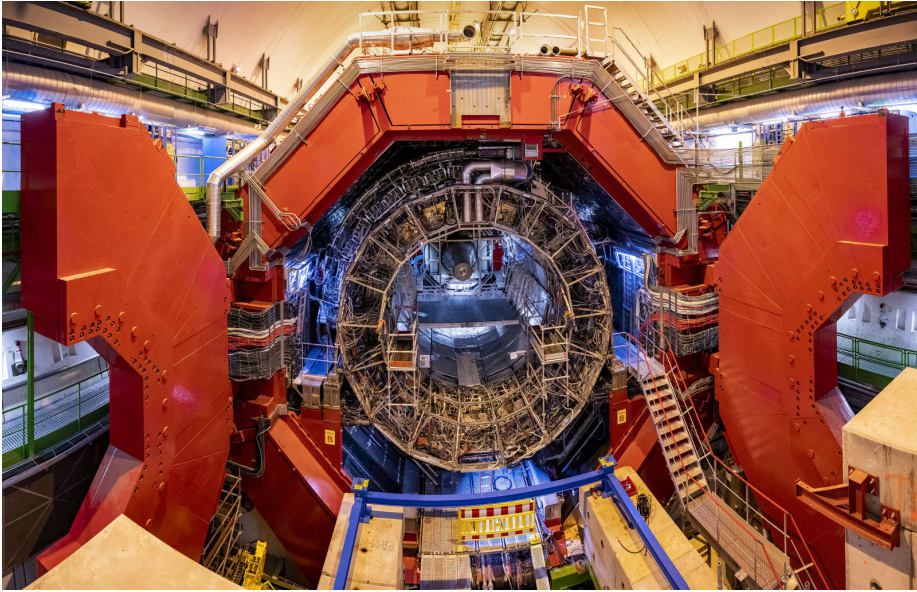


Figure 1.3.: Photograph of ALICE taken on 23.01.2020 [63]. The experiment is undergoing an upgrade so the magnet doors are open and the inner detectors are removed

ticles emerging from the interaction point, where the QGP forms after collisions. To achieve this goal, ALICE has to utilize multiple particle detection techniques in several subdetectors. They can be grouped into the following categories:

- **Trackers**, extracting the particle momentum and charge;
- **Calorimeters**, providing energy of selected particle species;
- **Time-of-Flight**, reconstructing particle masses, contributing to the particle identification (PID);
- **Transition radiation detector**, measuring particle momenta, participating in PID;
- **Muon arm**, focusing on properties of highly-penetrating muons;
- **Forward and trigger**, detecting global collision properties independently from the others.

ALICE has been collecting data since the start of operation of the LHC, during Run 1 (2009-2013) and Run 2 (2015–2018). The runs were separated by the Long Shutdown 1 (LS1) which lasted for two years. The LHC and its pre-accelerators were upgraded to improve performance at that time. During the LS1 the ALICE upgraded its electromagnetic calorimeter system, by adding a second subdetector, DCAL, with azimuthal coverage of 60° , as an extension of already existing EMCAL covering the opposite 120° [65]. Also, PHOS was upgraded and the first CPV module was installed [66]. The TRD also installed the remaining 10 supermodules [67]. The TPC readout was upgraded [68], as well as hard drives, operating systems and online software [69].

At the end of 2018, the LHC entered its second Long Shutdown (LS2), after which the Run 3 will start. The LS2 upgrades of the LHC require a major upgrade or replacement of multiple subdetectors in ALICE. One of the new subdetectors is the Fast Interaction Trigger (FIT) [70]. It will replace the T0, V0, FMD and AD subdetectors that were used before the LS2. It will serve as the trigger, main ALICE luminometer and it will play a major role in the collision classification in terms of unbiased charged-particle multiplicity, centrality and reaction plane. This information is a very important starting point for more detailed studies of the QGP flow and other phenomena.

1.6. Author's contribution

The author has been full-time involved with the FIT project since 2014 when the first detector module prototype was tested at the T10 beamline at CERN. He participated in 7 out of 8 prototype beam tests in the detector R&D phase (2014–2018), contributing to the following areas of activity related to the beam tests:

- **Hardware installation, alignment and management at the experimental site**

It resulted in the gain of experience in handling of high-voltage devices, NIM electronics and a laser alignment system, and becoming familiar with running procedures at the industrial-scale facility of the T10 beamline. Additionally, the author has been qualified to control the beam properties at the T10. The beam energy, polarity and focus point could be selected by adjusting the currents flowing through the dipole and quadrupole magnets. The beam collimators were also adjusted to control the size and spread of the beam. In the last four beam tests, the author also performed the duties of a safety officer with permission to patrol the beam test site and confirm the area is secure. Such a confirmation was needed before the beam could be released.

- **Pulse shape and data analysis**

The experimental data was collected with a digitizer. A special analysis software was created, with significant participation of the author, to convert the raw waveforms to time, amplitude and charge signals. The next analysis step involved devising appropriate quality cuts to filter out the background and plotting the selected quantities.

- **Development of cross-talk mitigation technique**

Because an unexpected behaviour of the initial versions of the tested sensors was encountered an extensive analysis of the problem was performed by the author. It was finally identified as the time-delayed cross-talk between channels. While a moderate optical cross-talk was expected, its time-shift was surprising. The analysis showed that the majority of cross-talk was electrical, not optical. It allowed our collaborators from the INR to introduce the hardware modifications to the sensor, that eliminated the problem of electrical cross-talk. More details are presented in subsection 3.3.2 and subsection 3.3.3.

- **Approval of the novel FV0 light collection system**

The author helped in the quantification of the performance improvement of the new FV0 light collection system, that reaches a factor of 2 in time resolution with respect to the design used by the V0 (its predecessor).

In terms of topics unrelated to the beam tests the author has been involved in the following activities:

- **T0 on-call expert**

Since 2016 the author has covered in total 83 24-hour shifts split into four periods. It resulted in the gain of hands-on experience related to practicalities of running a large and complex system, like ALICE. It led to a deeper understanding of the experimental setup and the complicated interconnections between many ALICE subsystems, including the Detector Control System (DCS), Data Quality Monitoring (DQM), readout, trigger etc.

- **Characterization of MCP-PMTs**

The author has been responsible for the assembly, characterization and running the acceptance tests of approximately half of the PLANACON[®] MCP-PMT photosensors delivered for FIT. He has created the software to automatically analyse collected data to obtain single photoelectron spectra and the gain curves [71]. He has also created a software to plot the CAEN Gecko logs [72], used to monitor high-voltage channels and their current consumption. The details of assembly steps, analysis procedures and example results are described in subsection 3.3.14.

- **ALICE software development**

The author has implemented the realistic optical properties to the FT0 detector simulation code in the ALICE analysis frameworks: AliRoot and O² (see subsection 3.6.1 for details). For this purpose, the extensive data, that is not readily available for the public, had to be collected from manufacturers of photosensors and quartz radiators. The data required proper conversion and adjustment to be used with either of the ALICE software frameworks. In 2020, the author has become responsible for the FV0 detector software development in the O².

- **Performance simulations**

The detector design has been validated at different stages also using simulations. The author has run all of the simulations and analysed the resulting data described in subsection 3.3.12 and Section 3.6.

- **Organizer of the weekly FIT software meeting**

Since the beginning of 2020, the author has become FIT software meetings organizer. They have been held weekly to discuss the progress in the development of the part of O² framework, that is related to the three FIT detectors: FT0, FV0 and FDD.

- **FT0 run coordinator**

Since the beginning of 2020, the author has been assigned the role of the FT0 run coordinator. The job of a run coordinator is to be the interface between the people involved with the subdetector and the global ALICE Run Coordination team. The responsibilities related to this position include ensuring the detector's readiness for operation and reporting the recent status and developments in the weekly meetings.

- **Student supervision**

The author has organized the tutorial for new students in 2016, concerning the practicalities of running the FIT beam test and introducing the hardware and software tools to them. He has also been supervising the summer students at CERN in 2019. It resulted in one student implementing the three-dimensional geometry of the FV0 into O² during the 3 months of his internship. The other students, who visited CERN for a shorter time, were involved in the MCP-PMT assembly and characterization, preparation of detector mock-up needed for integration tests and analysis of the simulated data.

The latest developments and intermediate results related to this work have been presented regularly in conferences and meetings. The two most relevant conferences, where the author has given an oral presentation, that was followed by the publication of proceedings, were the EPS Conference on High Energy Physics (HEP-EPS 2017) [73] and the XXXIX International Conference on High Energy Physics (ICHEP 2018) [74]. The list of the most relevant publications and conferences is included in Appendix A.

1.6.1. Publications

As of 20.04.2020, he has co-authored 211 publications related to heavy-ion particle physics as a member of the ALICE collaboration and the following three technical papers.

[1] E.V. Antamanova et al. Anode current saturation of ALD-coated Planacon®

MCP-PMTs. *JINST*, 13(09):T09001, 2018.

- [2] D.A. Finogeev et al. Performance study of the fast timing Cherenkov detector based on a microchannel plate PMT. *J. Phys. Conf. Ser.*, 798(1):012168, 2017.
- [3] V.A. Grigoryev et al. Fast timing and trigger Cherenkov detector for collider experiments. *J. Phys. Conf. Ser.*, 675(4):042015, 2016.

1.6.2. Other activities

Because the PhD topic has changed, the author has also been involved in other activities, which are not part of this thesis, namely:

- The activities in the Pyhäsalmi mine in Finland (related mainly to the EMMA experiment)
- The Muon Monitor experiment in the LSC, Canfranc, Spain

The two presentations on the related topics were given by the author in two national conferences and a poster was presented at one international summer school:

- Physics Days 2014, Tampere, 2014.03.11–13
Poster: *Extension of EMMA with Limited Streamer Tube detectors*
- Particle Physics Day 2013, Helsinki, 2013.10.24
URL: https://www.mv.helsinki.fi/home/hitu_www/hituday_2013.html
Talk: *Recent multiplicity distributions in EMMA experiment*
- Intelligent Front-End Signal Processing for Frontier Exploitation in Research and Industry (INFIERI 2013), Oxford, 2013.07.10–16
URL: <http://www.physics.ox.ac.uk/inferi2013/>
Poster: *Data acquisition system for the EMMA experiment*

These activities resulted in co-authorship of the following publications:

W. H. Trzaska, M. Slupecki et al. Cosmic-ray muon flux at Canfranc Underground Laboratory. *Eur. Phys. J.*, C79(8):721, 2019.

P. Kuusiniemi et al. Performance of tracking stations of the underground cosmic-ray detector array EMMA. *Astropart. Phys.*, 102:67–76, 2018.

S. K. Agarwalla et al. The mass-hierarchy and CP-violation discovery reach of the LBNO long-baseline neutrino experiment. *JHEP*, 05:094, 2014.

- S. K. Agarwalla et al. The LBNO long-baseline oscillation sensitivities with two conventional neutrino beams at different baselines. 2014.
- S. K. Agarwalla et al. Optimised sensitivity to leptonic CP violation from spectral information: the LBNO case at 2300 km baseline. 2014.
- I. De Bonis et al. LBNO-DEMO: Large-scale neutrino detector demonstrators for phased performance assessment in view of a long-baseline oscillation experiment. 2014.
- A. Stahl et al. Expression of Interest for a very long baseline neutrino oscillation experiment (LBNO). 2012.
- P. Kuusiniemi et al. Underground multi-muon experiment EMMA. *Astrophys. Space Sci. Trans.*, 7:93–96, 2011.
- T. Kalliokoski et al. Can EMMA solve the puzzle of the knee? *Prog. Part. Nucl. Phys.*, 66:468–472, 2011.
- A. F. Yanin et al. Multichannel Data Acquisition System for Scintillation Detectors of the Emma Experiment. 2011.

Additionally, they resulted in co-authorship of the following conference proceedings:

- W.H.Trzaska, et al. High-multiplicity muon events observed with EMMA array. *J. Phys. Conf. Ser.*, 1468:012085, 2020.
- W. H. Trzaska et al. Acoustic detection of neutrinos in bedrock. *EPJ Web Conf.*, 216:04009, 2019.
- W. H. Trzaska et al. Possibilities for Underground Physics in the Pyhasalmi mine. In *13th Conference on the Intersections of Particle and Nuclear Physics (CIPANP 2018) Palm Springs, California, USA, May 29-June 3, 2018*.
- L. B. Bezrukov et al. New Low-Background Laboratory in the Pyhäsalmi Mine, Finland. *Phys. Part. Nucl.*, 49(4):769–773, 2018.
- I. Bandac et al. Calculation of total muon flux observed by Muon Monitor experiment. *J. Phys. Conf. Ser.*, 934(1):012019, 2017.
- S. Lubsandorzhiev et al. A New Low Background Laboratory in the Pyhäsalmi Mine: Towards ^{14}C free liquid scintillator for low energy neutrino experiments. *PoS, ICRC2017:1044*, 2018.
- T. Enqvist et al. Measuring the (^{14}C) content in liquid scintillators. *J. Phys. Conf. Ser.*, 718(6):062018, 2016.

P. Kuusiniemi et al. Muon multiplicities measured using an underground cosmic-ray array. *J. Phys. Conf. Ser.*, 718(5):052021, 2016.

J. Sarkamo et al. EAS selection in the EMMA underground array. *J. Phys. Conf. Ser.*, 409(1):012086, 2013.

P. Kuusiniemi et al. Underground cosmic-ray experiment EMMA. *J. Phys. Conf. Ser.*, 409(1):012067, 2013.

2. ALICE at the LHC

2.1. The LHC and infrastructure

At CERN the extreme particle collision energies required for QGP studies are reached using an infrastructure of several machines arranged in stages. In the beginning of the chain, there is an electron cyclotron resonance (ECR) ion source, where an isotopically pure lead sample is heated up to about 800°C to vaporize it. The vapour is then subjected to high-frequency electromagnetic field superimposed with a static magnetic field, which strips away some of the electrons from lead atoms. Thus, they become ions and can be accelerated using the electric field in the linear accelerator called Linac3. They gain energy of 4.2 MeV per nucleon there. Subsequently, they travel through the Low Energy Storage Ring (LEIR), which performs two functions. It accelerates ions to 72 MeV and partitions the beam into tight bunches consisting of $2.2 \cdot 10^8$ ions. Such a beam structure is suitable to be injected into the 628 m long Proton Synchrotron (PS). The last electrons are stripped away from lead ions there, as their energy per nucleon is increased up to 5.9 GeV. The further boost, up to 177 GeV, is provided by the 7 km long Super Proton Synchrotron (SPS). Finally, the ions reach the 27-km long Large Hadron Collider (LHC), where they collide at the centre of mass energy of 5 TeV. The last three stages of the acceleration, i.e., the PS, the SPS and the LHC are common also for proton beams, while in the initial stages different machines are used: proton source, Linac 2 (Linac 4 after 2018) and the Proton Synchrotron Booster (PSB). The map of LHC-related accelerators at CERN is shown in Figure 2.1. The right-side picture shows the layout of larger accelerators and the left-side focuses on the smaller devices, corresponding to the early stages of acceleration, up to the PS. The red colour denotes elements used only for protons. The blue colour corresponds to the devices used for accelerating heavy-ions. Black parts are common. The dashed line corresponds to the new hardware available after the Long Shutdown 2 (2019-2020).

The LHC incorporates two beam pipes, in which particles are circulating in the opposite directions. The beam pipes cross only in four sections, called intersection points, where collisions can take place. Around these points, four large detector

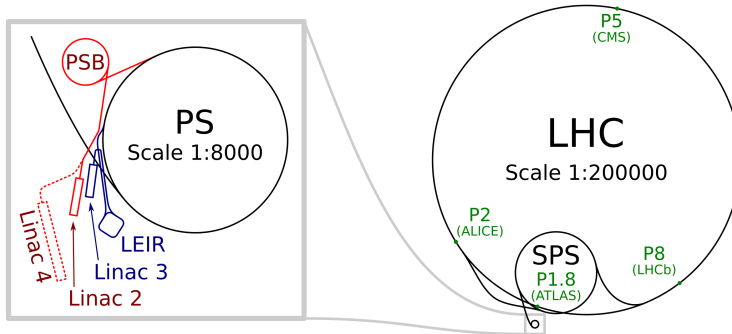


Figure 2.1.: Map of accelerators at CERN [75–77]

systems are built. The ATLAS and the CMS are general-purpose detectors, designed to study a wide range of phenomena. One of their prominent contributions was the experimental discovery of the Higgs boson [3, 4]. The LHCb experiment investigates rare decays used to study the CP violation, a phenomenon that can shed light on the asymmetry between matter and anti-matter in the Universe. The ALICE focuses on studying the QGP.

2.1.1. The LHC as a collider

The LHC is a collider [78, 79], a machine which performs the functions of synchrotron and storage ring. A synchrotron is a type of a cyclic accelerator, that keeps particles in similar, stable orbits independently of the particle energy. This is achieved by synchronising the growth of magnetic field of bending magnets (dipoles, placed along the beamline) with increasing energy. The energy boost is provided by a series of radio-frequency (RF) cavities, generating variable electric field which is tuned to accelerate and maintain grouping of particles into bunches. Once dipoles reach their maximum magnetic field, particles cannot be accelerated any further, otherwise the radius of their orbit would increase and eventually the whole beam would lose stability and dissipate in the beam pipe walls. To avoid it, when the particle beam reaches maximum energy the role of a collider shifts from the synchrotron to the storage ring. The storage ring can keep the particle beam circulating at its design energy with minimal beam intensity losses for at least several hours. Due to Coulomb force, a tightly-packed bunch of similarly-charged particles tends to spread. Focusing magnets (quadrupoles, octupoles)

are used to maintain the preferable size and structure of the beam. After the maximum energy is reached trajectories of two beams circulating in the opposite directions are slightly shifted until they cross in the designated intersection points, where collisions start occurring. Every collision diminishes the intensity of beams and therefore the collision rate decreases as well. This decrease is also due to beam-gas collisions, that happen with the particles of residual gas present in the imperfect vacuum of the beam pipes. In time, when the collision rate drops below some threshold, it becomes more efficient to dump the beams and start another cycle from scratch.

2.1.2. The beam structure, stability and focusing

The particle acceleration at a synchrotron is performed using a device known as RF-cavity. Inside it, an electric field oscillates at radio frequency. The incoming particles need to encounter the right direction of the field to be accelerated and not decelerated. Therefore, the arrival time of particles at the cavity is crucial. An RF-cavity also helps to stabilize the beam by focusing it longitudinally both in the acceleration phase and during operation at full energy. At full energy the particles arriving slightly ahead of the bunch centre are decelerated, while the late-arriving particles are accelerated.

This implies the beam must be composed of relatively tightly squeezed bunches. A single bunch must be short enough to pass the cavity within half a period of the oscillating field, otherwise it will be split into several consecutive bunches. In practice, the beam is never ideal and the particle distribution within any single bunch has some tails. After going through RF-cavity they are slightly separated from the main bunch and form the so-called satellite bunches or satellites.

At the LHC the RF-cavity is tuned to oscillate at 400 MHz, corresponding to the period of 2.5 ns, which is the distance between the positions of the main bunch and the first satellite. The collision time distribution measured by the T0 detector at ALICE is shown in Figure 2.2. The plot represents a subsample of raw data from the first three hours of pp run (#288806) at the $E_{\text{CMS}} = 13$ TeV, containing $2.2 \cdot 10^6$ events. The main collisions are centered at time = 0. The collisions between the preceding bunches and the triggering bunches are at time = -12.5 ns. The vertex of such collisions is shifted with respect to the nominal interaction point by approximately 3.75 m along the beam direction. The Figure 2.2 clearly shows that the majority of collisions originate from the bunch-bunch interaction. Bunch-satellite or satellite-satellite events also occur, but their timing is shifted

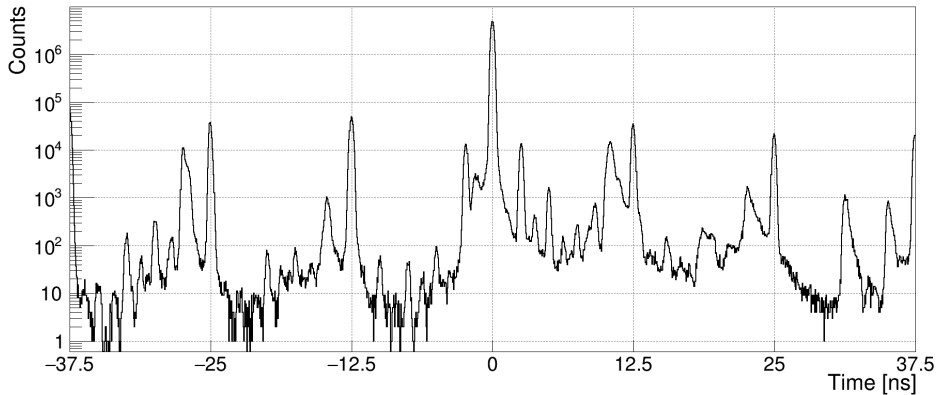


Figure 2.2.: Example of beam bunch structure and satellites recorded at ALICE

with respect to the expected bunch crossing time by 2.5 ns. The position of vertices corresponding to such events is also shifted along the beam direction.

The pp bunches are separated from each other by a multiple of 10 periods (25 ns) of RF-cavity field. They form trains separated by slightly longer time gaps. There is also a single beam-abort gap of 3 μ s, equivalent to 900 meters. It is the time required for a kicker magnet to power up when the beam needs to be dumped. The size and arrangement of trains depends on the earlier stages of accelerators, i.e., their size (defining the maximum number of bunches) and bending magnets used at injection. It is continuously optimized to maximize the delivered luminosity and machine efficiency.

Apart from the longitudinal beam focusing also the transversal one is necessary. It is achieved mainly by the quadrupole magnets, but higher multipole magnets are also used. A single quadrupole focuses the beam in one plane, but also slightly defocuses it in the other plane, so a pair or more of quadrupoles is needed to maintain desirable beam profile. The transversal size of the beam along the majority of the circumference of the LHC is kept relatively large, at 0.2 mm, to avoid strong Coulomb repulsion and minimize the required power of focusing magnets. Close to the intersection points a much stronger *inner triplet* of quadrupoles is used to decrease the beam size to 16 μ m. This increases the particle density within a bunch and the probability for collision, which directly affects the collision rate.

2.1.3. The beam life cycle

The beam life cycle at the LHC can be split into distinct phases, tightly connected with the state of the machine. The most common states, constituting a single fill during normal operation are described in order [80]:

- **Injection probe / setup beam**
Injection of a low-intensity beam from SPS to test the configuration of various components of the LHC and their ability to stabilize it
- **Injection physics beam**
Injection of high-intensity beam used for physics
- **Prepare ramp**
Injection is successfully completed, ongoing preparation for ramp-up of magnets
- **Ramp**
The beam is being accelerated, the magnetic field of dipoles is gradually increasing
- **Flat top**
The beam reached the target energy
- **Squeeze**
Squeezing the beam profile (or β^*) at the intersection points
- **Adjust**
Adjusting the beams after squeeze, during this phase the experiments start registering first collisions
- **Stable beams**
Only after declaration of stable beams the experiments start recording collision data
- **Beam dump**
The beam intensity dropped below threshold and it is being, will be or has been dumped; alternatively, there was a problem and emergency beam dump was performed
- **Ramp down**
The magnets are ramped down to prepare for the injection of the next fill

Stable beams state constitutes the majority of time during normal LHC operation,

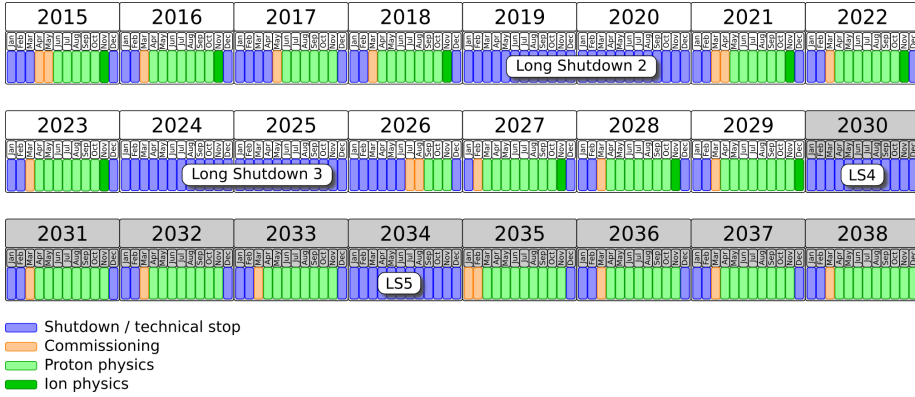


Figure 2.3.: Scheme of LHC operational timeline as of 2019/2020 [82]. The operation until 2029 is fully approved; beyond that the plan is approximate, which is indicated by the grey background. The COVID-19 outbreak is expected to cause significant delays from 2021 on

excluding maintenance breaks and shutdown periods. A single physics fill lasts usually between 4 and 12 hours. While the time from beam dump to the next stable beams can theoretically be slightly over one hour, in practice it usually exceeds 2 or 3 hours. The additional time is spent to make more checks or, in some cases, the beam is dumped prematurely never reaching *stable beam* state, for example, due to misinjection or beam instabilities during the ramp-up.

The injection from the PS to the SPS runs just over 10 s and the acceleration duration at the SPS is 4.3 s. The total time from the moment of particle leaving the ion source to the LHC injection is below 20 s [81]. Comparison of these numbers with those for the LHC shows the complexity and scale of the LHC operation. The injection from the SPS to the LHC takes almost 10 minutes for both beamlines, then the beam has to wait for 20 minutes before the 25-minute-long ramp-up of energy. The rate at which energy can be increased is limited by the properties of dipole magnets and extreme strength of the magnetic field, that they must reach. Finally, Squeeze and Adjust stages take another dozen of minutes.

2.1.4. The LHC operation during Run 1 and Run 2

After the initial incident with superconducting magnet quench in 2008, the LHC management opted for an incremental approach, increasing its operational parameters gradually. In the first five years of a stable operation (2009-2013), called Run 1, many machine components were tested, while the beam energy and luminosity was being increased. Following that, the machine was switched off to perform maintenance and upgrade to allow for further increase of these two most important parameters. This two-year-long period is called the Long Shutdown 1 (LS1). In 2015 the LHC was restarted into Run 2 and soon the latest standing world record in pp collision energy of 13 TeV was reached.

Over the three years of operation during Run 2, the LHC has exceeded the design pp integrated luminosity of 100 fb^{-1} by 65%. In Run 2 ALICE recorded the Pb–Pb integrated luminosity of 1.15 nb^{-1} , which corresponds to over an order of magnitude increase with respect to Run 1. In 2019 the LHC has entered the next Long Shutdown 2 (LS2) to further improve its performance. The following Run 3 is scheduled to last for 3 years, after which another upgrade period starts (LS3). The long-term LHC schedule is shown in Figure 2.3.

2.1.5. Operational parameters of the LHC in Run 3

The main component limiting the collision energy is the size of the collider and achievable beam bending radius. Since the LHC occupies the old LEP 27-km long tunnel, which defines the radius, the length of the collider cannot be increased. On the other hand, the beam-bending radius depends on the dipole magnets installed along the beamline. The LHC consists of 1232 superconducting dipoles, which constitute a substantial cost fraction of the whole machine, so they cannot be easily replaced. They are designed to operate at the current of 11.8 kA and generate the magnetic field of 8.3 T, corresponding to pp collision energy of 14 TeV, which is slightly larger than the maximum achieved in Run 2. After the last warm-up and cool-down cycle, which was performed during the LS1, the superconducting magnets were trained up to the slightly lower field, limiting the LHC energy to 13 TeV. It was deemed to be too time-consuming to train them fully, as more time dedicated to magnet training would mean less time for physics beam. The full magnet training is scheduled for the Long Shutdown 2 (LS2) [83], which will bring the LHC to its maximum design beam energy.

Similarly to beam energy, instantaneous luminosity has not reached the ultimate

design value yet. However, while the beam energy can be further raised by only a fraction of 8%, the luminosity can be increased significantly with only modest upgrades. In 2017 the instantaneous pp luminosity of $1.5 \cdot 10^{34} \text{ cm}^{-2}\text{s}^{-1}$ was routinely achieved, with a single test fill exceeding $2.0 \cdot 10^{34} \text{ cm}^{-2}\text{s}^{-1}$ [84]. While the maximum beam energy is related to the LHC hardware alone, the luminosity increase requires careful investigation, hardware tuning and upgrades at every step from the ion source, through linear accelerators, PS, SPS, LHC and interfaces between them, i.e., extractors and injectors. The major changes in the accelerator complex scheduled for LS2 are related to the proton (P) or heavy ion (HI) chain and include [85]:

- Replacement of Linac2 with Linac4 (P)
- Increase of the PSB magnetic field and upgrade of its power supply and RF systems to allow for higher proton injection energy of 2 GeV/c to the PS (P)
- At ion source and Linac3 (HI): modernization of beam monitoring equipment
- At Linac3 (HI): increase of injection rate to LEIR from 5 to 10 Hz
- At LEIR (HI): reduction of beam losses and installation of external beam dump
- At the PS (both (P) and (HI)): bunching improvements, installation of additional beam monitoring instrumentation (longitudinal and transversal feedback)
- At the SPS (both (P) and (HI)): upgrade of RF power supplies and cavities; mitigation of pp beam intensity losses due to electron cloud also during ion injection and energy ramp-up; reduction of the length of the bunch trains injected from the SPS to the LHC allowing for a larger number of ion bunches at LHC; reduction of injection kicker rise time at the SPS from 225 to 150 ns; adaptation of machine protection equipment and beam dumps to the increased beam intensity

As of 2020 the maximum Pb–Pb instantaneous luminosity recorded by ALICE on 13.12.2015 was $1.1 \cdot 10^{27} \text{ cm}^{-2}\text{s}^{-1}$ (capped by limited readout capabilities). Maximum instantaneous luminosity delivered by the LHC was recorded by ATLAS at $3.7 \cdot 10^{27} \text{ cm}^{-2}\text{s}^{-1}$.

Table 2.1.: Amount of data collected by ALICE in LHC Run 1 and 2 [86]

Run	Year	System	$\sqrt{s_{\text{NN/pN}}}$ [TeV]	\mathcal{L}_{int} [$\sim\text{nb}^{-1}$]
1	2009-2013	pp	0.9, 2.76, 7, 8	0.2, 100, 1500, 2500
	2010-2011	Pb–Pb	2.76	0.075
	2013	p–Pb	5.02	15
2	2015-2018	pp	5.02, 13	1300, 35000
	2015	Pb–Pb	5.02	0.25
	2016	p–Pb	5.02, 8.16	3, 25
	2017	Xe–Xe	5.44	0.0003
	2018	Pb–Pb	5.02	0.55

2.2. ALICE highlights in LHC Run 1 and 2

ALICE is dedicated to studying properties of the QGP (see Section 1.3), such as degrees of freedom, speed of sound, transport coefficients, equation of state and the critical temperature, at which the phase transition between the QGP and hadronic matter occurs. The summary of statistics collected by ALICE during LHC Run 1 and 2 is listed in Table 2.1. ALICE results can be divided into three categories: soft probes, hard probes and production of exotic nuclei.

The soft probes are sensitive to collective phenomena of QGP, allow to reconstruct its thermal features and shed light on the production mechanism of hadrons. At LHC energies in ALICE the produced QGP medium size is measured to be $V = 300 \text{ fm}^3$ and its lifetime is 20% longer than at RHIC energies [87]. Thanks to its excellent particle identification capabilities, ALICE has also provided new data on p_{T} dependence of production of several hadron species [88] and baryon-to-meson ratios [89]. These results are consistent with our understanding of collective phenomena and interplay between mechanisms of hadron production, i.e., hadronization and recombination of quarks [86]. Strangeness enhancement has also been confirmed by ALICE in heavy-ion collisions of Pb–Pb [55]. Also, observing similar trend for other collision systems [90] has broadened our knowledge. Furthermore, ALICE has quantified the collective flow phenomena by mea-

asuring the anisotropic flow separately for different particle species and collision systems [91]. Thanks to ALICE experimental results it became possible to constrain the shear and bulk viscosities as a function of the QGP temperature [92,93].

The QCD implies that the hard probes should lose energy in QGP via gluonstrahlung [94]. ALICE has observed this phenomenon and compared it quantitatively in different collision systems and energies [95,96]. The charm and beauty quarks are excellent probes of properties of QGP since they can be produced only in the initial stages of the collision. The measurements of the nuclear modification factor of open charm states were performed by ALICE [97]. It has been found that in Pb–Pb collisions the interaction of these states with the QGP is as strong as that of all charged particles, i.e., their suppression was similar. On the other hand, when compared to the p–Pb collisions, no charm suppression is visible [98]. This indicates that the suppression is due to the interaction of heavy quarks with the medium and it is not related to cold nuclear matter effects.

ALICE has also contributed to the understanding of the coalescence and thermal models [99] by studying the production of light nuclei and antinuclei. The coalescence parameter is observed to decrease with increasing multiplicity [100]. This points to the shortcoming of the model, that does not account for the change of the size of the emitting volume.

The wealth of data obtained by ALICE in LHC Runs 1 and 2 confirms the basic picture of QGP being strongly-interacting hadronic matter. It also extends the precision of previous measurements and their kinematic range, as it operated at the highest temperatures achieved experimentally up to date, at wide p_T range and with excellent particle identification capabilities.

2.3. The ALICE upgrade

2.3.1. Motivation

In Runs 1 and 2, ALICE also observed a few unexpected phenomena with charmonia and other charm mesons [60]. The upgraded ALICE will focus on rare probes, their coupling with the QGP and hadronization processes, and on their correlations with other probes. At the LHC energies, these rare probes are produced more abundantly than at previous machines and include: heavy-flavour particles, quarkonia, photons, jets. However, selection of collisions including these rare probes is non-trivial and in most cases they are untriggerable.

One of the major Run 3 upgrade requirements imposed on all detectors, the DAQ and computing infrastructure is, therefore, related to improvement in collision rate handling capabilities. All major detectors, except TRD, are expected to record in continuous readout mode all Pb–Pb interactions at the rate of 50 kHz. In pp and p–Pb collisions the rates will reach up to a few MHz. Another important upgrade goal concerns the improvement of the tracking resolution at very high particle multiplicity environment of Pb–Pb collisions of about 1600 particles per unit of pseudorapidity. The upgraded trackers will be able to resolve secondary vertex position with a precision better than 50-100 μm , even for very low transverse momenta. Such resolution is essential to properly identify heavy-flavour decays. Additionally, further extension of the kinematic range, especially towards low transverse momentum, is also required. The experimental results from this kinematic region are essential to verify and tune different models. At the same time, the excellent ALICE particle identification has to be preserved.

Summarizing, the increase in statistics of two orders of magnitude and improvement in tracking resolution will allow access to these rare probes and the aforementioned precision measurements.

2.3.2. Detector and system upgrades

To achieve these physics goals and to adapt to change in LHC running conditions, ALICE will upgrade its subsystems during the LS2 [73, 74, 101]. Afterwards, it will be able to cope with the increased luminosity, trigger rate and irradiation. The layout of the upgraded ALICE subsystems is presented in Figure 2.4. The ALICE Upgrade consists of 6 main elements:

- **New Inner Tracking System** [102]
CMOS pixels, MAPS technology, better resolution, less material, faster readout
- **New Muon Forward Tracker** [103]
CMOS pixels, MAPS technology, forward vertex tracker
- **New readout chambers for the TPC** [104]
GEM technology, new front-end electronics, continuous readout
- **New Fast Interaction Trigger** [70, 105–109]
A hybrid of Cherenkov and scintillation detector technology, luminosity measurement, trigger, interaction time, centrality, reaction plane, background veto

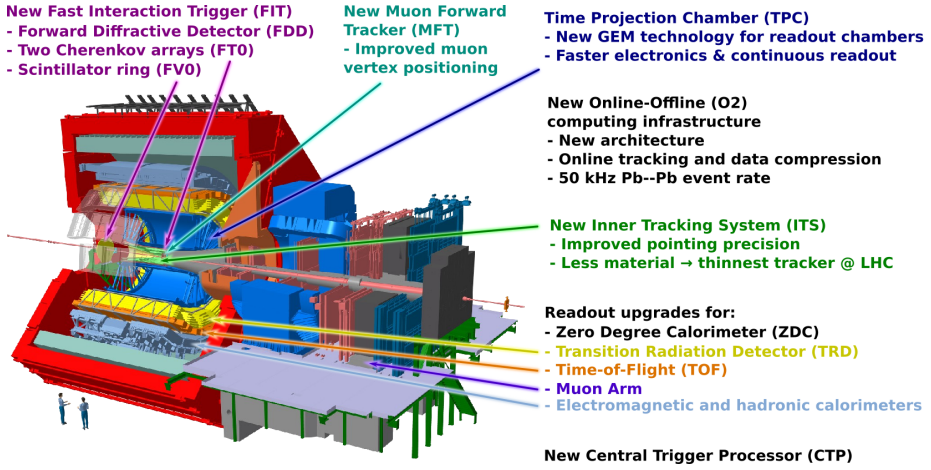


Figure 2.4.: ALICE upgrades

- **Readout upgrade** [70]
TOF, TRD, Muon Spectrometer, ZDC, calorimeters
- **Integrated Online-Offline (O²) system** [110]
Data acquisition and analysis framework, records minimum-bias Pb–Pb data at 50 kHz

2.4. Particle collisions – parameters and properties

2.4.1. The importance of energy and luminosity for physics

In a particle physics experiment, the collision energy at the centre-of-mass (E_{CM} or \sqrt{s}) is an important parameter defining the range of physical processes that are likely to occur [111]. It can be calculated from a kinematical sum of two colliding four-vectors:

$$E_{\text{CM}}^2 = (\mathbf{p}_1 + \mathbf{p}_2)^2 = (E_1 + E_2)^2 - (\vec{p}_1 + \vec{p}_2)^2 \quad (2.1)$$

Therefore, during the LHC Run 3 the maximum of $\sqrt{s_{pp}} = 14$ TeV, $\sqrt{s_{p-Pb}} =$

8.79 TeV and $\sqrt{s_{\text{Pb-Pb}}} = 5.52$ TeV will be available for the particle production. With such energies, every known Standard Model particle can be produced during a collision in any of the three main collision systems. In terms of the QGP phase diagram, the particles produced in collisions at such energies around the transverse plane, probe the region of the relatively high temperature of more than 180 MeV. At the same time, the baryon chemical potential is very low because the vast majority of particles detected around zero-rapidity originate from pair-creation processes, which generate the same number of particles and antiparticles. In other words, such conditions best resemble the quark epoch, $10^{-12} - 10^{-6}$ s after the Big Bang (see Section 1.3).

Moreover, a collision at higher energy probes shorter time-scales or smaller sizes and gives access to lower Bjorken- x . It allows to experimentally narrow down the upper limits of the size of fundamental particles described in the SM as point-like. It is worth stressing that the LS2 upgrade will result only in a modest increase in collision energy for Run 3.

Luminosity is a second important parameter dictated by an accelerator's design and influencing the physics performance. Luminosity measures the number of particles, that can be squeezed within the unit of cross section per unit of time. It is defined as:

$$\mathcal{L} \equiv NK \iint \int_{-\infty}^{\infty} \rho_1(x, y, s, -s_0) \rho_2(x, y, s, s_0) dx dy ds ds_0 \quad (2.2)$$

Where ρ_1 and ρ_2 are time-dependent density distribution functions of the two colliding beam bunches, $s_0 = c \cdot t$ is a *time* variable, $K = \sqrt{(\vec{v}_1 - \vec{v}_2)^2 - (\vec{v}_1 \times \vec{v}_2)^2} / c^2$ is a kinematic factor and N is the number of possible collisions per second.

Following the first-order approximations that a collision is head-on, densities are Gaussian and uncorrelated in all planes and the beams meet at $s_0 = 0$, it can be simplified to:

$$\mathcal{L} = \frac{N_1 N_2 f N_b}{4\pi\sigma_x\sigma_y} \quad (2.3)$$

The luminosity is proportional to the number of ions per bunch in each of the colliding beams, the number of orbiting bunches and the revolution frequency. The frequency is dictated by the circumference of the machine and the speed of par-

ticles. At the LHC particles move nearly at the speed of light, the circumference is 26659 m, so frequency reaches 11.2455 kHz.

The number of colliding bunches depends on the filling scheme. The bunches cannot be separated evenly for technical reasons. The first one is the need to reserve time slots to account for delays in the activation of the injection and extraction kicker magnets. Another challenge is to adjust the luminosity independently for different interaction points. This can be achieved by devising such a filling scheme, which results in a different number of bunch crossings at different IPs. Therefore, the filling scheme reflects (i) partly the requirements of pre-accelerators, (ii) partly these of the LHC and (iii) those of luminosity requirements at different IPs. For Pb–Pb run in 2015 at the LHC the most optimal filling scheme consisted of 518 bunches [112].

The maximum number of ions per bunch is limited by the focusing capabilities and beam losses along the whole accelerator chain. The higher the beam intensity the more losses due to impedance, synchrotron radiation, imperfect vacuum and electron cloud effects. Beam losses result in heating up of the beam pipe and instrumentation around it, including superconducting magnets, which can quench under such conditions. The ultimate limit is the amount of power the cryogenic systems can dissipate. Currently, at the LHC, it is about 7.5 kW per arc.

The instantaneous luminosity can be used to calculate the rate of collisions of a given type with a given cross section (σ_{coll}).

$$\mathcal{R}_{\text{coll}} = \mathcal{L} \cdot \sigma_{\text{coll}} \quad (2.4)$$

The integrated luminosity (\mathcal{L}_{int}) is another term, which directly relates to the number of interesting events, that an experiment can observe in a given time, providing the cross section (σ) for a given process is known.

$$\mathcal{L}_{\text{int}} = \int_0^T \mathcal{L}(t) dt \quad (2.5)$$

$$N_{\text{ev}} = \mathcal{L}_{\text{int}} \sigma \quad (2.6)$$

Therefore, luminosity is a convenient interface between the accelerator performance required by physics experiment and theorists or other experiments providing cross sections.

After the LS2 the instantaneous luminosity delivered by the LHC will increase almost by a factor of two with respect to the Run 1 [113] for Pb–Pb collisions. The effective gain will be even larger, because a new scheme of luminosity levelling will be applied. This scheme will extend the lifetime of fills while reducing the rate, at which instantaneous luminosity drops. Together with upgraded ALICE readout, it will make the data taking more efficient.

2.4.2. The pseudorapidity

The pseudorapidity is a spatial coordinate commonly used in the experimental particle physics. It only depends on the angle (θ) of particle's momentum with respect to the beam axis and is defined as:

$$\eta \equiv -\ln \left[\tan \left(\frac{\theta}{2} \right) \right] \quad (2.7)$$

As a function of three-momentum \vec{p} pseudorapidity is equivalent to:

$$\eta = \frac{1}{2} \ln \left(\frac{|\vec{p}| + p_z}{|\vec{p}| - p_z} \right) = \operatorname{atanh} \left(\frac{p_z}{|\vec{p}|} \right) \quad (2.8)$$

If the particle's mass is negligible pseudorapidity approximates the boost component of rapidity along the beam axis:

$$m \ll |\vec{p}| \implies \lim_{|\vec{p}| \rightarrow E} \eta = \frac{1}{2} \ln \left(\frac{E + p_z}{E - p_z} \right) = y_z \quad (2.9)$$

In special relativity the general equation for rapidity is:

$$y = \frac{1}{2} \ln \left(\frac{E + |\vec{p}|}{E - |\vec{p}|} \right) \quad (2.10)$$

Since pseudorapidity describes the angle of a particle outgoing from the collision region it is a convenient parameter to describe a detector's coverage. Detector located at mid-rapidity, i.e., ($-1 \lesssim \eta \lesssim 1$) will be exposed to different particle fluxes than a forward-rapidity detector, ($-2 \gtrsim \eta \gtrsim 2$), located close to the beam

pipe or farther from the collision region along the beam axis. Furthermore, the available range of physics processes changes with rapidity.

In a collider experiment pseudorapidity, together with azimuth angle (ϕ) and transverse momentum denoted as p_T , i.e., momentum perpendicular to the beam axis, are commonly used to describe properties of detected particles.

Since LHC energies are generally very high the Equation 2.9 holds and the terms *pseudorapidity* and *rapidity* will be used interchangeably in the following chapters.

2.4.3. Impact parameter and centrality

A heavy-ion collision is not point-like, because the colliding nuclei are not point-like. In the simplest approximation, two relativistic nuclei can be treated as spheres, flattened along their velocity vector due to Lorentz contraction. They collide by overlapping at least partly. The transverse vector connecting the centres of nuclei at this point is called the impact parameter and denoted as \vec{b} . It characterizes the overlap area and thus it is related to the number of participants (N_{part}), i.e., nucleons, which participated in the collision and to the number of binary nucleon-nucleon collisions (N_{coll}). The remaining nucleons, which are assumed to propagate unaffected along their initial momentum, are called spectators. The length of the impact parameter is of the order of a few femtometers and therefore it is impossible to be controlled or measured directly. Similarly, the N_{part} cannot be measured because the energy of initial participants is used immediately after the collision to create thousands of particles. In a high-energy collider experiment, the direct measurement of the number of spectators (N_{spec}) is also difficult because they move at very high rapidity, close to the remaining beam.

The stochastic nature of such collisions is described by the Glauber model [114]. It provides a method of linking the distribution of the observable number of charged particles (N_{ch}) with distributions of geometrical parameters, listed in the previous paragraph by introducing the idea of centrality.

Centrality describes how central a given event is when compared to other events in the same sample. Technically, centrality can only be estimated by ordering a sample of HI events by the N_{ch} , which is the best-identified proxy for the centrality of a collision. Events with highest N_{ch} are caused by the most central collisions, in which \vec{b} and N_{spec} is low, while N_{part} and N_{coll} is high. The exact matching is obtained using the Monte Carlo method based on the Glauber model.

In practice, events are divided into centrality classes, where the centrality class of 0–10% means 10% of most central events, while most peripheral events are assigned the centrality of 80–100%.

The centrality is one of the most important parameters describing a collision, because it is related to the amount of energy available for physics processes and therefore forms a basis allowing to compare the measurements between different experiments, using different beam energies and collision systems.

2.4.4. Reaction plane and anisotropic flow

Following the simple HI collision model presented in the previous paragraph, in a non-central collision the overlap region in the transverse plane is not circular, but rather it is almond-shaped. There exists a preferred direction along \vec{b} . It is worth noting that, following the stochastic nature of HI collisions, the direction of \vec{b} is isotropic in different events, i.e., the distribution of its azimuth angle is uniform.

If a collective equilibrium is reached in the process governing the expansion of the fireball the initial geometry of the overlap region is transformed by physics processes (see Section 1.4) into anisotropies of outgoing particles momenta. This gives rise to azimuthal anisotropies [115, 116] of produced particles within a single event. The anisotropies are measured and can be quantified by expanding the distribution of azimuth angle of detected particles in a Fourier series of the following form:

$$\frac{dN}{d\phi} \propto 1 + 2 \sum_{n=1}^{\infty} v_n \cos(n(\phi - \Psi_n)) \quad (2.11)$$

In the equation above n is the harmonic number, while v_n and Ψ_n correspond to flow coefficients and symmetry planes. The elliptic flow coefficient (v_2) dominates, due to the shape of the initial overlap region. The experimentally measured non-zero values of directed flow (v_1) and higher-order coefficients are caused by fluctuations in the position and momenta distributions of nucleons participating in the collision. It is worth stressing that the symmetry plane is different for each harmonic.

Experimentally, flow coefficients can be calculated using event plane method. Firstly, the 2D flow vector \vec{Q}_n is:

$$[Q_{n,x} \quad Q_{n,y}] = \left[\sum_i w_i \cos(n\phi_i) \quad \sum_i w_i \sin(n\phi_i) \right] \quad (2.12)$$

Where ϕ_i and w_i are azimuth angle and weight of the particle with i -index. The usual choice for weight is particle's transverse momentum. The same vector can be represented using event planes characteristic to the whole single event:

$$[Q_{n,x} \quad Q_{n,y}] = \overrightarrow{Q}_n [\cos(n\Psi_n) \quad \sin(n\Psi_n)] \quad (2.13)$$

From here the event plane is:

$$\tan(\Psi_n) = \frac{Q_{n,y}}{Q_{n,x}} \quad (2.14)$$

$$\Psi_n = \text{atan2}(Q_{n,y}, Q_{n,x})/n \quad (2.15)$$

The observed flow coefficients can be calculated as:

$$v_n^{\text{obs}} = \langle \cos [n (\phi_i - \Psi_n)] \rangle \quad (2.16)$$

Where angle brackets mean an average over all particles in all events. It should be kept in mind that flow coefficients generally depend on centrality, transverse momenta and rapidity.

Several factors are limiting the resolution of flow coefficients. One of them is the fact that the number of available particles is finite. The others are related to the detection system, that is, to the limited angular resolution, acceptance or efficiency of a detector. Therefore, the observed flow coefficients have to be corrected by the event plane resolution:

$$\mathcal{R}_n = \langle \cos [n (\Psi_n - \Psi_{\text{RP}})] \rangle \quad (2.17)$$

Finally, the true flow coefficients are:

$$v_n = \frac{v_n^{\text{obs}}}{\mathcal{R}_n} \quad (2.18)$$

From the equations above it can be deduced, that a sufficient event plane resolution is required from a detector to properly perform flow-related physics analyses.

2.5. Background sources

2.5.1. Introduction

All detection systems are subject to some sort of noise, i.e., even in the absence of real or intended detection, an output signal can be generated. There are several generic noise sources, that exist for any kind of a detector, like ambient electronic noise or cross-talk between different channels. These noise sources form a background for any physics analysis. Additional background in a particle physics experiment is due to uninteresting events induced by natural radioactivity, like cosmic-ray interactions or decay chains, or artificial radioactivity coming from material activation within the particle beam site. Even more sophisticated background in a hadron collider experiment includes beam-gas interactions and QED e^+e^- pair production.

Depending on the nature of background, there exist different methods that aim to mitigate its influence on experimental data. The main background sources and background reduction methods are described below.

2.5.2. Detector- and electronics-specific noise

Design of most kinds of modern particle detector types is based on a relatively simple idea of converting an occurrence of physics phenomenon into an electric pulse. The physics phenomenon in case of optical detectors can be the scintillation light or Cherenkov light generation by a charged particle traversing the detector volume. For other detector types, it can also be the ionization of the detector material. In optical systems, the conversion from photon to electron happens on the photocathode of a photomultiplier. The electron is then transported and multiplied using an electrical field to the output terminal, where many secondary electrons form a charge which is large enough to be sent to the front-end electronics circuitry. The readout electronics further amplifies the signal and converts it to a digital form that can be collected and analysed by computers.

In this scheme of operation, there are a few possible sources of noise. Firstly, in the optical part, the light could come from an unintended source. Therefore,

detectors are often enclosed in light-tight casings and optical parts are separated from any materials that can cause sparking. Secondly, if the sensor is too sensitive during the photon-electron conversion process it could start extracting electrons from the photocathode due to their non-zero thermal energy. In some applications detectors even need to be cooled down before they operate properly. Thirdly, during the electron multiplication, atoms of residual gas are ionised. The ions start drifting in the direction opposite to electrons and collide with the photocathode. This results in the release of secondary electrons that cause afterpulses.

Since the effects mentioned above can only be minimized, but not eliminated, further mitigation techniques are applied at the later stages of signal processing. The readout electronics usually discriminates the signal incoming from the sensor. In the simplest case amplitude, timing or total charge of the signal is compared with some threshold values. The thresholds are adjusted in such a way that eliminates the majority of noise-induced signals, while the efficiency for the real signals is maintained. The accepted signals are amplified and shaped to match the input requirements of the digital part of the readout. At the readout stage, the most serious background comes from analogue transmission lines, which can act as antennae and pick up electromagnetic (EM) waves. The usual way to minimize this kind of noise is to shorten transmission lines and to surround them with adequate EM shielding. Once the signal is digitized it is much more robust and almost immune to such interferences. Nowadays, a single-chip approach is commonly used in which the sensor, analogue and digital readout are integrated into the single chip. While this approach is not feasible for all sensor types, less flexible and more expensive to develop, it helps to avoid the noise problems related to signal transmission.

2.5.3. Cosmic rays

The background signals induced by cosmic rays [117] are unavoidable. The majority of air-shower particles can be stopped in a few meters of shielding. This is one of the reasons why collider particle physics experiments are often built at the shallow depths below ground. The only air-shower component penetrating shielding are neutrinos and high-energy cosmogenic muons. Because the cross section for neutrino interaction is small their contribution to the background is negligible. On the other hand, muons are charged particles and ionize any material they traverse and therefore produce a strong signal in virtually any detector

type. Fortunately, the cosmogenic muon flux decreases steeply with the thickness of overburden and the final rate, even at a relatively shallow depth of a few dozens of meters, is many orders of magnitude lower than interaction rates produced by a collider. Once the rate of cosmogenic signals is low enough, it can ultimately be filtered out almost entirely using time-gating and tracking. The particles of interest originate from the vicinity of the collision point, so all particles not fulfilling this condition can be treated as background.

While cosmic-rays are considered to be background during normal operation, they can be used as free and ever-present calibration source and means to commission detectors before the beam is available.

2.5.4. Natural radioactivity and material activation

As natural or artificial radioactivity can disturb the measurement if it comes from within the sensitive volume of the detector, it usually is of no great concern. The particles emitted in the natural decay processes or due to material activation have much lower average momentum than these originating from the HI collision. They are also not correlated in time with the collision but happen randomly. Consequently, their signal is often weaker and falls below the threshold. If it is strong enough, it is still possible to measure the background in the absence of the beam and then subtract it from the actual experimental data.

2.5.5. Beam halo and beam-gas events

The beam optics is meant to keep the particles within a narrow beam, but the momenta of some of them deviate beyond the capability of beam optics to compensate it. While they are still affected by the magnetic fields of dipoles and quadrupoles, they tend to drift further and further away from the beam axis. To minimize the risk of damaging sensitive components located along the circumference of a collider, a set of collimators is commonly used to absorb such a peripheral beam component. The kinematics of the fixed-target collision of a particle with collimator dictates that most of the reaction products propagate at very high rapidities. Most of the secondary particles are absorbed within the collimator, but some may escape it causing the beam halo. A similar mechanism exists also with the walls of the beam pipe, that may act as a collimator in its absence.

Another contribution to the beam halo comes from the beam-gas interactions [118, 119]. They happen when the beam collides with residual gas of imperfect vacuum inside the beam pipe. The rate of these events depends on the quality of the vacuum and density of particles within the beam. Therefore, any increase in luminosity of a collider leads to increase of beam-gas background.

Kinematics of the beam halo hints at the possible method of rejection of this kind of events and suppressing background related to them. The beam halo event is essentially a fixed-target interaction at much lower E_{CM} than a corresponding collision could reach. As such the centre-of-mass frame of reference moves at close-to-relativistic speed along the beam direction. From the stationary collider experiment point of view, the vast majority of particles outgoing from the interaction caused by the beam halo moves at a small angle with respect to one of the beam directions. Therefore, a detector located on both sides of the interaction point, which is sensitive to particle direction can distinguish the collision at the nominal interaction point from a beam halo interaction.

Apart from generating background for experiments, the beam halo reduces the overall performance of a collider by limiting the maximum beam intensity and lifetime of fills.

2.5.6. Ultraperipheral collisions (UPC) and QED pair production

Every bunch crossing at a heavy-ion collider is associated with some probability for a collision. There are various kinds of physical processes that can occur during a collision and their rates are proportional to collider-specific luminosity and the cross section of a given process (see Equation 2.4). It is important to distinguish between well-understood soft processes of purely quantum electrodynamical (QED) origin and the interesting hadronic interaction [120]. The QED [121, 122] events occur more frequently because the cross section for QED e^+e^- pair production is five orders of magnitude higher than the cross section for hadronic interaction, i.e., for Pb–Pb at $\sqrt{s} = 5.5$ TeV

$$\sigma_{\text{QED},e^+e^-} \sim 230 \text{ kb} \gg \sigma_{\text{hadronic}} \sim 7.75 \text{ b}, \quad (2.19)$$

They form background, significant especially for ultraperipheral collisions with impact parameters larger than the sum of radii of colliding nuclei ($|\vec{b}| \gtrsim R_1 + R_2$), i.e., for centralities larger than 80%. The physical processes causing these UPCs

include Pomeron-Pomeron interactions and, for even larger impact parameters, photon-Pomeron interactions. There exists a broad diffractive physics programme focusing on these processes [123,124]. Experimentally, since the interacting nuclei remain intact, such low-multiplicity events tend to be very clean. The identification of a UPC event relies on the fact that it has very low charged particle multiplicity at central rapidity region compared to even a very peripheral hard hadronic interaction. However, the UPC triggers are largely contaminated by QED background events.

Because of much higher cross section, several QED processes are likely to occur during a single bunch crossing. This means any hadronic event is accompanied by many QED interactions. The probability to produce N electron-positron pairs follows the Poisson distribution:

$$P(N) = \frac{e^{-p} p^N}{N!} \quad (2.20)$$

Where p denotes probability to produce a single pair.

Within a hadronic event, it is essential to properly identify particles of pure QED origin. Only then they can be either rejected or used as additional probes. Otherwise, they contribute to the background. The identification methods are mainly based on precise tracking to differentiate the point of their origin from the primary hadronic vertex. Ultimately, to mitigate the effect of remaining, unidentified QED pairs within a hadronic event a background subtraction based on Monte-Carlo simulation is applied.

Additional QED pair filtering comes naturally in modern collider experiments due to the presence of the magnetic field. It is primarily used to identify particle momenta based on track curvature. The magnetic field sets a threshold for low- p_T electrons, which are unable to escape the central region of the experiment to reach the detectors. The differential cross section for QED pair production drops quickly with increasing e^+e^- momenta. Therefore, high enough magnetic field eliminates the most abundant low-energy pairs of e^+e^- at the central rapidity region.

3. The Fast Interaction Trigger (FIT)

3.1. Motivation

Following the goals of the ALICE upgrade (introduced in 2.3.1) and considering that the number of ALICE subdetectors cannot be feasibly upgraded to follow the continuous readout scheme [70, 125], the need for a fast trigger detector emerges. The Table 3.2 lists the trigger requirements of ALICE detectors. There are 6 detectors that require an external trigger for operation, three of them at level *minus one* (LM) and three at level 0 ($L0$). The latencies associated with each trigger level in ALICE are shown in Table 3.1 [126–131]. Six more detectors may utilize the triggers generated externally, but it is not technically required for their operation. Only TPC [104] and ACORDE [132] do not foresee any use of external trigger.

An external trigger is, therefore, either necessary or at least useful for the vast majority of ALICE detectors. By default, they expect a minimum-bias (MB) trigger and some, additionally, a multiplicity-based trigger. The need for such a set of triggers is the main motivation to add the FIT detector.

3.1.1. ALICE trigger distribution

Triggering in ALICE is handled by the Central Trigger Processor (CTP) [128, 133]. The scheme of devices and connections between the CTP and the detectors

Table 3.1.: Trigger levels and their latencies in ALICE in Run 3 [126]

Trigger level	Latency at the CTP input [ns]
LM	425
L0	1200
L1	6100

Table 3.2.: Trigger requirements of ALICE detectors (status on 11.2019)

Detector	Hardware trigger		
	Level	Type	Trigger essential
TRD	LM	MB	Yes
CPV	LM	MB, multiplicity	Yes
HMPID	LM	MB, multiplicity	Yes
EMCAL	L0	MB, multiplicity	Yes
DCAL	L0	MB, multiplicity	Yes
PHOS	L0	MB, multiplicity	Yes
ITS	LM	MB	No
MFT	LM	MB	No
ZDC	L0	MB	No
TOF	L1	MB	No
MCH	L1	MB	No
MID	L1	MB	No
TPC	-	-	No
ACO	-	-	No

is shown in Figure 3.1. The CTP collects trigger signals from many detectors and systems and processes them to form the triggers accepted by the Local Trigger Units (LTUs) and forwarded to the Common Readout Units (CRUs). The CRUs control data flow from the detector to the Online-Offline (O²) system [110]. The LTUs form an interface, that is common for all detectors, between the CTP and readout of the detectors. The LTUs can work in standalone mode, emulating the CTP. Such functionality is useful during trigger system integration in detector laboratories and during commissioning in standalone runs.

The system is highly versatile and remotely configurable. It can send different triggers to different systems while keeping track of all of them and allowing for later synchronization and event building. One of the outstanding functionalities is throttling of readout frequency individually for each subdetector. If a subdetector becomes busy the system will automatically stop sending triggers until the readout of the detector is ready to continue processing data. It is especially important considering the readout of several detectors is not upgraded after Run 2 and they will not be able to cope with very high interaction rates expected in Run 3. For them throttling will function as a safety valve, preventing local buffer overflows.

3.1.2. Minimum-bias trigger detector

One of the trigger types generated by FIT in pp and p–Pb is the MB trigger. Ideally, to eliminate bias the following conditions should be met:

- Only collision events should be accepted
- No collision event can be rejected based on its individual characteristics
- The observables (particles) used to generate trigger should not be directly reused in physics analyses

In practice, the bias can only be minimized, but not eliminated. The first item in the list can be translated into effective background-reduction measures. The second item prevents unknown correlations from affecting the collected data. It is commonly realised by maximizing detection efficiency and exercising care with any cuts. It is worth noting that this item allows for random rejection of events. Such technique is used in ALICE to reduce the trigger rate (see throttling in subsection 3.1.1) for detectors, that cannot process their data fast enough while allowing others to collect more MB statistics. The third item is often achieved by

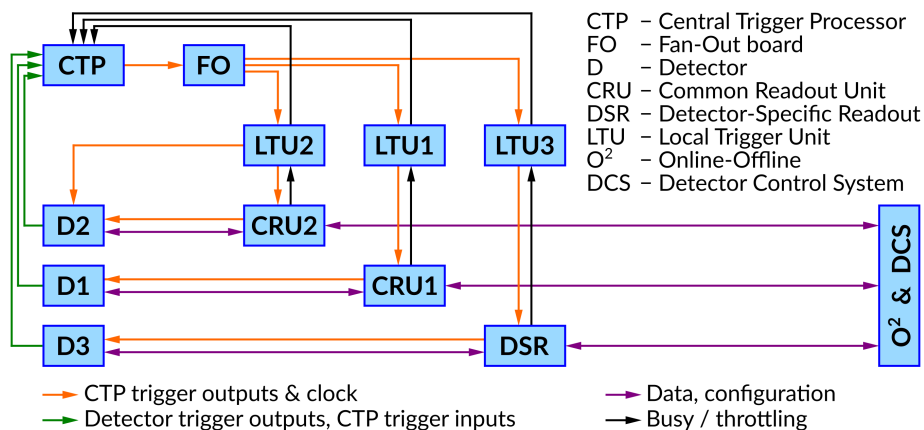


Figure 3.1.: Trigger and timing system of ALICE in Run 3. D1 represents the new configuration introduced for Run 3, default for most detectors; D2 is a special case of D1 designed for the Run 3 ITS, with the additional fast connection from LTU to the detector; D3 corresponds to a detector with old, Run 2 readout. Figure is based on information in [128]

positioning trigger detectors at different pseudorapidities than other detectors. This way the forward particles are used for triggering and mid-rapidity particles are available for physics.

In Run 2 the *OTVX* signal was produced by the T0 detector and used by ALICE as the MB trigger in pp and p–Pb runs. The T0 consisted of two arms of Cherenkov detectors located on both sides of the interaction point at distances of 681 mm on the C-side and 3741 mm on the A-side. The *OTVX* trigger was generated under the following conditions:

- A coincidence between the two detector arms was required, i.e., at least one minimum ionizing particle (MIP) had to be detected by the T0-A and at least one MIP – by the T0-C.
- The time of signals generated by each side had to fit within a narrow time window of ± 2.5 ns, synchronized with the LHC clock. The time of a side was defined as the first time from any of the sensors located at this side.
- Based on the time difference between the sides the z -component of vertex position was calculated. The vertex was required to be within ± 10 cm in Pb–Pb and ± 20 or 30 cm for pp.

The FT0 component of FIT will use a similar technique in Run 3 to purify its triggers. The major difference is related to the fact that FIT will perform all of these steps using integrated readout system. The signal from each channel will be digitized early and the gates will also be applied digitally. Thanks to that it will be possible to use the average timing of each side, not only the first arriving signal.

3.1.3. Multiplicity trigger detector

The FIT aims at providing also the multiplicity trigger, as the need for such trigger is declared by five ALICE detectors, listed in Table 3.2. The particle multiplicity is a useful observable, especially for detectors with limited readout-rate capabilities, that focus on highly energetic processes, for example, related to jet physics. The interest of such detectors in MB triggers is mainly to establish a baseline of unbiased reference data, while the majority of new physics observations is expected to come from high-multiplicity events.

To generate multiplicity triggers, FIT must be capable of providing a reasonable estimate of the total number of particles produced during a collision. This

requires the following conditions to be met:

- Multi-particle detection efficiency has to be maximized
- The dynamic range of each detection channel should be no less than the expected maximum number of particles

To fulfil them the detector could have high granularity, such that it is unlikely that more than one particle traverses the volume of one pixel. In such scenario pixel could be instrumented with binary readout: fired or not. However, for FIT such an approach is not feasible due to the large density of particles, and timing requirements discussed in subsection 3.1.2. The cost of readout would not be acceptable, as the total number of pixels would be high, translating into an equally high number of expensive timing channels. The only other approach is to build a detector with lower granularity, but with its pixels capable of detecting the number of charged particles that hit them. This approach requires careful optimization of the amplitude resolution, signal shape and dynamic range of each pixel and readout channel. The required dynamic range depends on the final size of the pixel or cell and its location, so it varies for different parts of the detector. To retain high detection efficiency for single MIPs, the multiplicity in the most central pixels of FIT may exceed the dynamic range in the most central Pb–Pb collisions. This topic is covered in subsection 3.3.12.

3.1.4. Luminometer

Apart from generating trigger, FIT will monitor luminosity in real-time and send the feedback directly to the LHC to help tune the beam. Although many small detector and feedback systems, including luminometers, are an integral part of the LHC, ALICE requested that in its vicinity such devices are not present. They could interfere with signals measured by ALICE. This concerns especially ZDC detector [134], which is located at high pseudorapidity regions, relatively far away from the interaction point. Instead of having a single-purpose luminosity detector, possibly interfering with signals measured by ALICE, it was decided that an additional functionality of luminosity measurement will be performed by an already existing or foreseen subsystem within ALICE. As the forward, MB trigger detector, FIT fulfils the requirements.

FIT will use similar technique to that used in Run 2 by the T0, V0 and AD detectors [135,136]. Using a set of van der Meer (vdM) scans [137,138] a visible cross section (σ_{vis}), that is valid for a given detector and trigger condition, can

be calculated. After transforming the general formula from Equation 2.4, the instantaneous luminosity measured by the detector is:

$$\mathcal{L} = \frac{\mathcal{R}_{\text{trig}}}{\sigma_{\text{vis}}} \quad (3.1)$$

The σ_{vis} already includes the detector efficiency and acceptance (ϵ):

$$\sigma_{\text{vis}} = \epsilon \cdot \sigma_{\text{inel}} \quad (3.2)$$

If the detector performance is stable in time, the visible cross section is constant for a given collision system at a specific collision energy. In practice, the vDM scans are performed infrequently, only when the detector performance deteriorates, or when a new collision system or energy is introduced. During routine runs the σ_{vis} is stored in a database and reused.

In Run 2 the *OTVX* signal was used as the main luminometer in pp and p–Pb collisions. While all of the *OTVX* signal requirements reduce the efficiency of the signal, it is already accounted for in σ_{vis} measured during a VdM scan. There is no need to know the efficiency or acceptance explicitly to measure luminosity.

3.1.5. Expected contribution to offline analyses

The FIT is expected to contribute to offline analyses, by recording the following information:

- particle multiplicity and hit time for each channel
- clean trigger, with minimal contribution from background (beam halo, beam-gas, QED)
- veto flag for the UPCs
- collision time and its resolution
- trigger rate

By combining this information a measurement of forward event multiplicity can be performed. Thanks to that FIT will reconstruct centrality and event plane. Moreover, by providing the collision time, FIT can participate in the reconstruction of particle masses with the Time-Of-Flight (TOF) detector. Its contribution

is especially important for low-multiplicity events, where the time resolution of FIT is expected to be better than that of TOF. This is based on the Run 2 experience, where in central p–Pb collisions (centrality $\leq 40\%$) both the T0 and TOF detectors were able to determine collision time efficiently. The T0 was superior for more peripheral events. In Pb–Pb system, the collision time reconstruction benefitted from T0 data only for the most peripheral events (centrality $\geq 80\%$).

As an extension of online luminosity monitoring, FIT will provide input for the integrated luminosity calculation, useful as a reference to calculate relative cross sections for various physics processes [139].

As a forward detector, FIT will contribute to diffractive physics [140, 141] and select ultra-peripheral events that are one of the cleanest tools to study the high-energy limit of QCD [124, 142].

With the precise timing of FIT, an additional functionality of detecting multiplicity of collision pile-up may be possible. Two or more collisions may happen within one bunch crossing. If their vertices are sufficiently separated in the (z) direction along the beamline and their products hit different FIT detector modules, FIT may be able to flag such pile-up events during offline data processing. This functionality is hypothetical and untested. The detected particles that are slower than light can blur the picture.

3.2. General design concept

To achieve a sufficient level of MB trigger purity the detector has to meet stringent timing requirements. The single-MIP time resolution of any individual pixel must be better than 50 ps, which limits the number of available detector technologies significantly. The aim to reach LM latency (Table 3.1) and requirement of magnetic field tolerance leaves only a Cherenkov detector as a viable option. On the other hand, to maintain the Run 2 performance the detector needs to be larger than could be achieved at a reasonable cost with Cherenkov technology alone. Therefore, a hybrid design, expanding acceptance of Cherenkov array with plastic scintillators, is used. The overall dependencies between design constraints, features and performance requirements are shown in Figure 3.2.

FIT design strikes a balance between performance and cost. It consists of 3 components: FT0, FV0 and FDD (see Figure 3.3 and Figure 3.4). Each of them is optimized for different function and operational regime. The Cherenkov

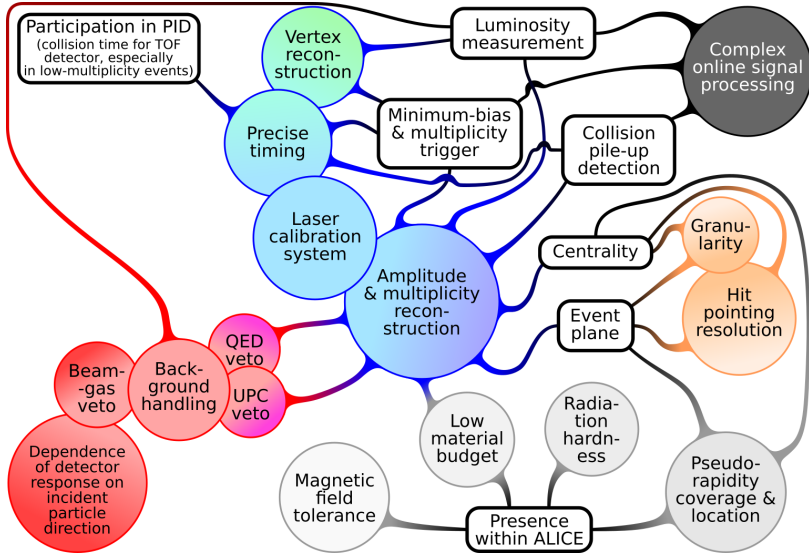


Figure 3.2.: FIT functional requirements and linked design features

detector array (FT0) has good timing properties and signal-to-background ratio. The sectorized scintillator ring (FV0) aims at enlarging FITs acceptance towards mid-rapidities. It improves trigger efficiency and dynamic range. The Forward Diffractive Detector (FDD) provides forward pseudorapidity coverage.

The FT0 and FDD detectors are composed of two arms each, located on both sides of the interaction point. Such design helps in filtering background since trigger can be generated only for events, in which there is a coincidence of signals from both arms. This triggering scheme, together with a timing gate allows the rejection of the vast majority of beam-gas interactions (see subsection 2.5.5). The mechanism is the following: if a beam-gas interaction happens between the arms then only one of them will register particle hits. This is because such an interaction is similar to a fixed-target experiment, where the centre-of-mass and products of the reaction move in one direction, along one of the beams mainly. There would be no coincidence between the arms. On the other hand, if a beam-gas interaction happens elsewhere both arms will register particle hits, but the arm on the side of the interaction will fire much earlier than the other arm. Therefore the gating based on the time difference between signals arriving from

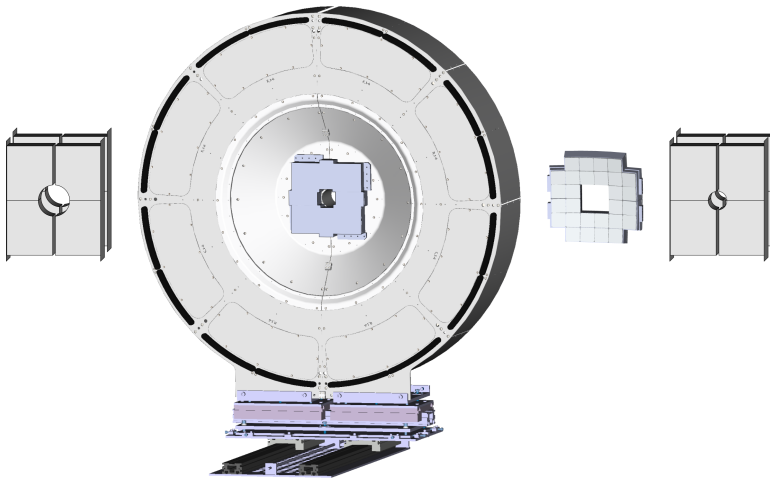


Figure 3.3.: Complete set of FIT subdetectors arranged side-by-side. The graphic reproduces correct relative sizes of the FIT elements. From left: FDD-A, FT0-A connected with FV0, FT0-C, and FDD-C are shown

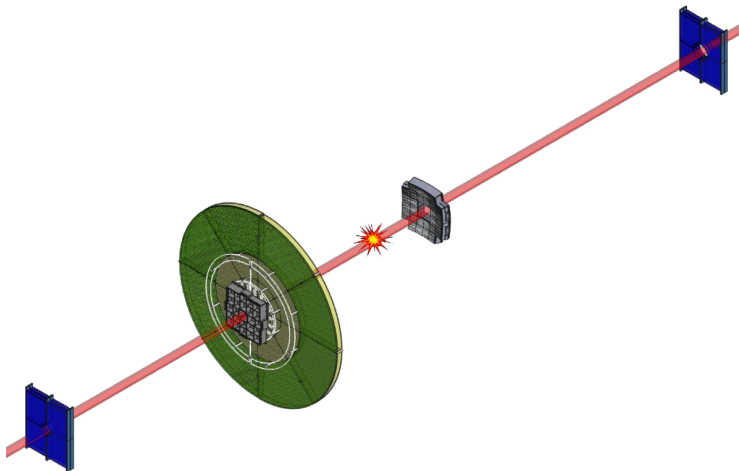


Figure 3.4.: FIT detectors aligned along the beamline. From bottom-left FDD-A, FT0-A connected with FV0, interaction point, FT0-C, FDD-C. The distances along the beamline are not up to scale

both arms is an effective way to eliminate this source of background.

Additionally, the total latency from the interaction to the arrival of FIT trigger signal to the CTP has to be below 425 ns to be in time to generate LM trigger signal. For the FT0 the time of flight from IP to the detector is ~ 11 ns, sensor delay is ~ 1 ns, cables to readout electronics are ~ 30 m long, which translates into 138 ns. The signal delay induced by the 7-m long cable from the FIT readout electronics to the CTP adds 30 ns. The processing time of prototype readout electronics, including digital trigger generation, is ~ 205 ns. The time adds up to 385 ns. The contingency against the maximum allowed trigger latency, dictated mainly by the timing constraints on the wake-up signal for the TRD, is about 40 ns. In case of the FV0, the contingency is smaller (18 ns) because the light collected from scintillator cells propagates along fibres, before it is read by the photosensors. The additional fiber length and slower FV0 photosensors increase the delay. The FDD will only generate L0 trigger, mainly because of its distance from the IP and the corresponding cable-induced delay. The total time delay for FDD, that takes into account the time of flight from the IP, the time delay introduced by the detector, the PMT and the 50-meter long signal cable, is approximately 290 ns.

The convention of naming the sides around the interaction point has been agreed within ALICE for all detectors and systems [143]. The **C**-side refers to the north-west side on which Muon Spectrometer is located, towards the town of Crozet or CMS experiment. The **A**-side is on the opposite side of the interaction point, where the L3 magnet doors are located, towards the south-east, the municipality of Meyrin and ATLAS experiment. This convention is used by FIT detectors to refer to their arms as FIT-A (including FT0-A, FDD-A, FV0) and FIT-C (including FT0-C and FDD-C).

Because there is very little space between the IP and the hadron absorber on the C-side, only the thin Cherenkov array without scintillator fits there. The length constraint excludes the use of fine-mesh PMTs as photosensors, which could be one of only a few alternatives, operational in a strong magnetic field and at high radiation level. Instead, Cherenkov arrays use much thinner MCP-PMT technology for light detection. On the A-side, further away from the IP, the dimensional constraints are more relaxed, so the Cherenkov array is accompanied by a large, sectorized scintillator ring.

3.2.1. Forward location

As an MB trigger detector FIT has to be located at high pseudorapidity region to measure unbiased collision properties. This location helps to avoid interference with very precise, low-material-budget trackers. It is also beneficial for the measurement of the centrality and event plane because such measurement is entirely independent from those performed by central-rapidity detectors. This way the division of pseudorapidity coverage between physics-oriented trackers, grouped with other particle-identification (PID) detectors, and servicing detectors, that trigger and provide global collision parameters, helps to avoid bias. The downside of such an arrangement is slightly lower statistics at the higher pseudorapidity comparing to the mid-rapidity. For reference see the distribution of primary particles produced by different collision systems as a function of rapidity in Figure 3.5.

The pseudorapidity coverages and dimensions of different FIT components are presented in Table 3.3. The radii and z -positions are in millimeters; z -position denotes the distance along the beamline direction with the nominal interaction point set as origin. For rectangular detector geometries (FT0 and FDD) r_{\min} represents the distance from the closest sensitive element of the detector to the beam axis (z -axis), which is along x or y axis. The r_{\max} is the distance of the furthest sensitive element from the beam axis, which is along the detector's diagonal. Similarly, two limits for η_{\min} and η_{\max} are presented. Within this η -range the detector does not have full azimuthal coverage. For the FV0 this distinction is irrelevant because the detector is azimuthally symmetric.

The graphical comparison of pseudorapidities of selected ALICE detectors, including FIT subdetectors, is shown in Figure 3.6. In the graph, the pseudorapidity ranges of ITS, MFT and TPC are provided as reference. For FV0 different shadings correspond to 5 detector rings. The FT0 and the FDD are rectangular, so their pseudorapidity coverage is not the same for all azimuth angles. The pseudorapidity ranges, that are not fully covered by one of these detectors, are marked with brighter colours. For the ITS the darker regions show where all 7 layers are present.

3.2.2. Environmental considerations

Further constraints in the design appear due to environmental conditions, at which the detector is expected to operate. Firstly it has to be radiation-hard. FIT will have to withstand the total dose of up to 100 krad. The Figure 3.7

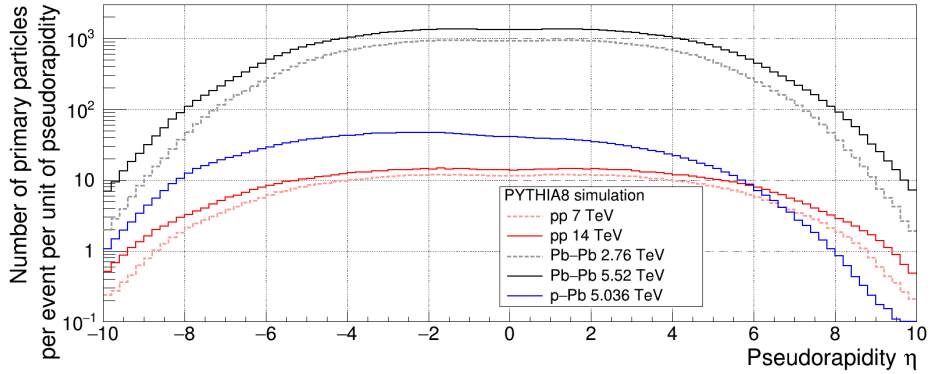


Figure 3.5.: Comparison of simulated particle densities as a function of pseudorapidity for different collision systems. All curves are based on PYTHIA8 [144,145]

Table 3.3.: Pseudorapidity coverages, dimensions and location of the front faces of sensitive elements of FIT subdetectors. For the FT0, a quartz radiator is a sensitive element. For FV0 and FDD, plastic scintillators are sensitive components.

Subdetector	z	r [mm]		η	
		r_{\min}	r_{\max}	η_{\max}	η_{\min}
FT0-A	3305	47.5	205.6	4.9	3.5
FV0-A, ring 1	3160	41	72.1	5.0	4.5
FV0-A, ring 2		73.9	128.1	4.4	3.9
FV0-A, ring 3		129.9	211.6	3.9	3.4
FV0-A, ring 4		213.4	386.1	3.4	2.8
FV0-A, ring 5		387.9	720.25	2.8	2.2
FDD-A	17000	62	282	6.3	4.8
FT0-C	-843 to -819	63.3	211.1	-2.1	-3.3
FDD-C	-19500	37	282	-4.9	-7.0

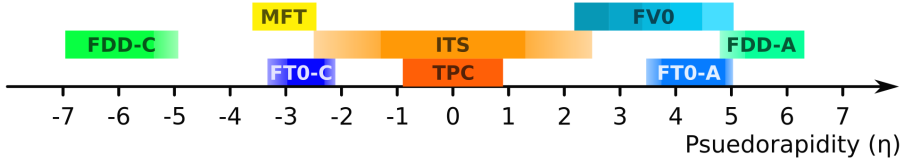


Figure 3.6.: Graphical representation of pseudorapidity coverage of selected ALICE subdetectors [102–104], focusing on the FIT elements

represents the spatial distribution of the dose. It takes into account the realistic uptime of the LHC, beam intensities and energy, and the QED background over the running period of Run 3 and Run 4. The left-side plot focuses on the C-side only and extends further in radius to see the possible cable route and patch-panels placement. Two right-side plots focus on the regions occupied by the inner FIT arrays. The overlay of the FIT active elements is marked and labelled. For the FV0, also the range of rings is marked, where $r1$ denotes ring 1, etc. The ring $r5$ is not shown, because it extends beyond the range of r -axis. The shape of FT0 is not circular, but rectangular-like, so FT0 does not cover azimuth angle uniformly. Therefore, the outer regions are only partially azimuthally covered by the detector. These regions are marked in grey. The MFT envelope is marked for reference.

While the sensing parts of the detector are more robust, most commercial electronics components would fail at such a dose. Therefore, in the vicinity of the interaction point, there is no active electronics. The analogue signal is sent with 40-m cables directly from sensors to the racks housing readout electronics.

The FIT has to tolerate the magnetic field of up to 0.5 T, as it is located inside a large L3 magnet, used otherwise for particle momentum reconstruction with trackers. The Figure 3.8 presents all three components of magnetic flux density vector ($\vec{B} = [B_x, B_y, B_z]$) in two z -positions, where the FT0-A and FV0 (top row) and the FT0-C (bottom row) are located. The figure is based on the set of measurements performed for the ALICE detector configuration in Run 2, that are interpolated to form the continuous B-field map and available in AliRoot framework [147, 148]. The magnet was set to operate at 0.2 T. In case of operation at 0.5 T the small non-uniformities visible for B_x and B_y scale proportionally. Such detailed maps are not available for the remote location of the FDD. Despite one arm of the FDD is attached to one of the LHC magnets, the sensors are located

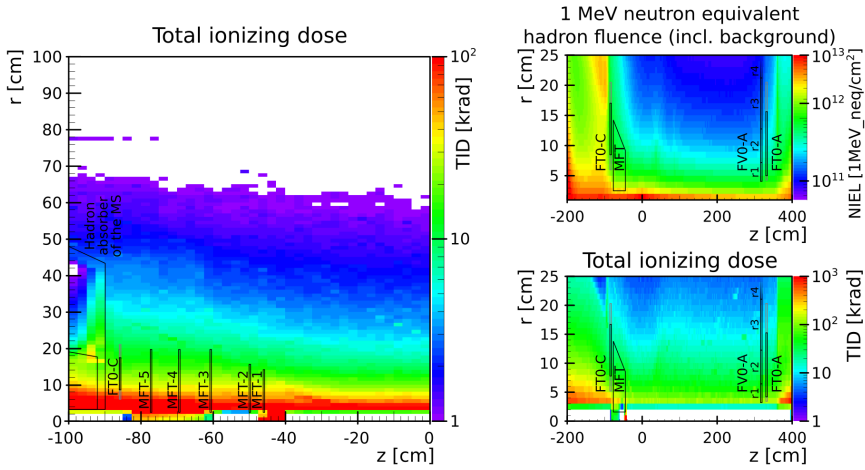


Figure 3.7.: Radiation maps based on simulations, focusing on regions occupied by the FIT components located closer to the IP (FT0 and FV0). The figure is based on [146]

at a considerable distance. The measurements show that on the A-side (C-side) the FDD photosensors will experience magnetic field up to 5.5 mT (2.2 mT).

Although the readout electronics is located at least a few meters from magnets, it can be exposed to stray magnetic fields. It means it should be well shielded to avoid the saturation of the cores in switching power supplies that could damage active electronic components. Additionally, a special procedure to switch off readout electronics before commencing any magnet state transition must be implemented.

As a general rule in complex, multilayer particle detectors the material budget should be minimized to avoid interfering of the detector with the detected signal. The forward location of a trigger detector makes this requirement less stringent since there are fewer detectors behind it.

Other constraints are related to the obvious dimensional limitations due to the presence of other detectors, beam pipe, support structure and services, such as cabling, cooling systems, etc. The total weight also has to be taken into account to ensure the support structure (miniframe) could hold it.

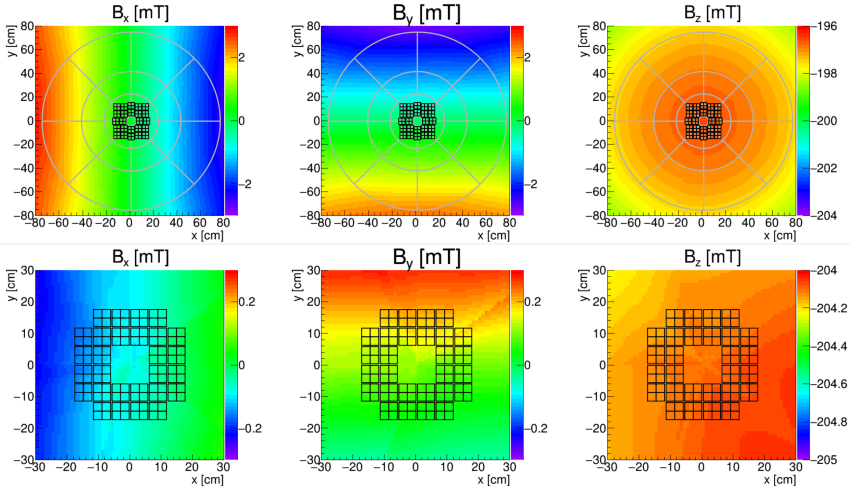


Figure 3.8.: Magnetic field maps in the z -positions, corresponding to the location of the FT0-A and FV0 arrays (top row), and the FT0-C array (bottom row)

3.2.3. Comparison with FIT predecessors from Run 2

The FIT detector replaces four forward detectors of the previous generation, that were decommissioned after Run 2 [149]: T0 [150–153], V0 [154, 155], FMD (Forward Multiplicity Detector) [156, 157] and AD (Alice Diffractive) [141]. The T0 detector used to be responsible for luminosity measurement and high-quality timing. The V0 generated minimum-bias trigger and reconstructed centrality and event plane. The FMD produced forward particle multiplicity spectra. The AD focused on background estimation and the physics of ultraperipheral and diffractive collisions.

The FT0 part of FIT is a similar detector type as the old T0, however the total area, number of sensors and the number of channels has been increased significantly. The FV0 derives some design features from V0, with one arm missing due to spatial constraints. To compensate for the loss of half the area, the remaining arm has been enlarged as much as possible. To improve timing FV0 developed a new light collection system, which does not rely on wavelength-shifting fibres. There is no single-detector replacement for FMD, that specialized in measuring

Table 3.4.: Comparison between old ALICE subsystems and their replacements within FIT

Detector	z [mm]		#channels	
	A-side	C-side	A-side	C-side
FT0	3305	-843 to -819	96	112
T0	3741	-681	12	12
FV0	3160	—	48	—
V0	3290	-871	40	40
FDD	17000	-19500	8	8
AD	17000	-19500	8	8

forward particle multiplicity. However, FT0-C and MFT cover similar pseudo-rapidities and aim to do a similar measurement with comparable quality. The AD is replaced by the FDD, which uses faster scintillator, wavelength shifter and photosensor. The differences in geometry and number of channels between the systems from the previous generation and FIT are listed in Table 3.4. The values for T0 and V0 were extracted from the AliRoot geometry simulation code used throughout Run 1 and Run 2. The distance to the interaction point (z) is measured from the middle of the sensitive volume (quartz radiator or scintillator) along the beam direction.

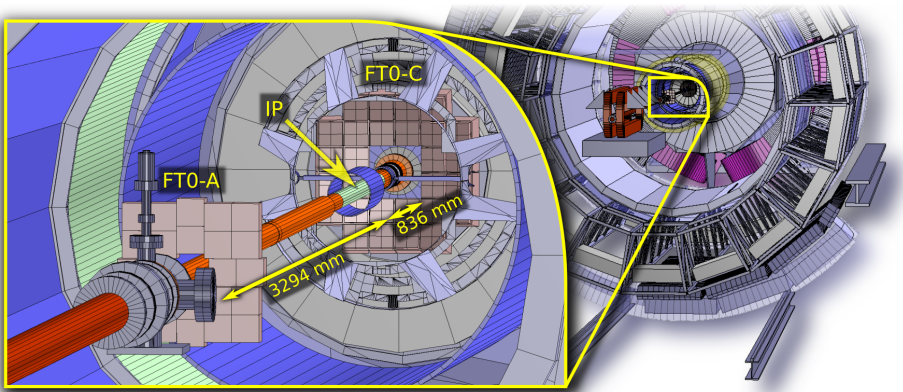


Figure 3.9.: Render of the FT0 geometry within ALICE in the simulation framework; most of the inner ALICE components are not visible for clarity

3.3. The FT0

The Cherenkov array consists of FT0 detector modules. On the C-side a single layer of 28 modules surround the beam pipe. The number of modules used there is the maximum that fits in the constrained space available. The modules are arranged in a concave shape to minimize the angle of incident particles, that equalizes the amplitudes. The distance between the IP and the front face of Cherenkov radiator of each detector module is kept approximately constant at ~ 845 mm. The z -position (along the beam direction) of the front faces is between -843 and -819 mm. Due to the presence of a flange around the beam pipe at that position the inner opening of FIT-C has to be at least 120 mm wide.

On the A-side, 24 FT0 modules are arranged in a single, planar layer surrounding the beam pipe. The distance from the IP to the detector plane, aligned to the front face of Cherenkov radiators, is 3305 mm.

The render of both FT0 detector arrays within ALICE is shown in Figure 3.9.

The backbone of the Cherenkov detector module consists of two elements: a photosensor and a Cherenkov radiator block made of a material transparent to ultraviolet light. These two elements should be optically coupled to maximize the efficiency of light transport from the radiator to the photosensor. The further

details of the design process of the FT0 module are presented in the following subsections. The final design is presented in subsection 3.3.18.

3.3.1. Motivation for detector module R&D at CERN PS

While the rudimentary detector module tests were performed in a laboratory with picosecond laser pulses, more exhaustive tests require a particle beam of sufficient energy to produce Cherenkov light inside the detector. The monochromatic laser light fed from a side of a radiator poorly corresponds to real-life detector operation, in which Cherenkov light is generated with characteristic anisotropy within the volume of radiators and with characteristic wavelength spectrum. The difference in wavelengths affects such material properties as refractive index and transparency. The quantum efficiency of a photosensor is also a function of wavelength. Together with the difference in position and direction of the light source, these factors are very relevant to design an optimal geometry of radiators, their granularity, coating, optical grease and to generally optimize the detector performance.

The FT0 detector module prototypes were tested at the T10 beamline at CERN's East Hall [158]. Secondary beams are delivered from the Proton Synchrotron to the T10. They consist mainly of pions, kaons and muons. To avoid excessive signal time dispersion, caused by contamination of the beam by the heavier, primary protons, the negatively-charged beam was chosen. The beam energy was set at the maximum value for this beamline of 6 GeV/ c to ensure clean Cherenkov response of the tested detectors. The experimental setup used across all the beam tests, performed between 2014 and 2017, is shown in Figure 3.10. The *T0C* and *T0D* are spare Cherenkov detectors from the T0. To ensure the measured signal originated from the beam and not from the background the hardware trigger was set as coincidence between *T0C* and *T0D*. The tested *MCP1* and *MCP2* detector prototypes were located downstream and the *XY* segmented scintillation detector registered hit-position information with resolution of about 1 cm.

The data from all detectors were collected by the CAEN 742 digitizer. The waveforms were analysed to extract the time and amplitude information for every acquisition channel. Subsequently, run-specific event cuts were applied to reduce background. Commonly, the main requirement was the presence of high amplitude pulse with appropriate timing in the trigger detectors (*T0C* and *T0D*). At the same time, pulses with too high amplitude were rejected, due to saturation of the readout and incorrect time and amplitude reconstruction. The left

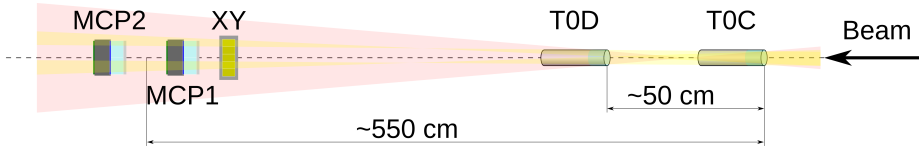


Figure 3.10.: Scheme of FT0 experimental setup at the T10 beamline at CERN's East Hall

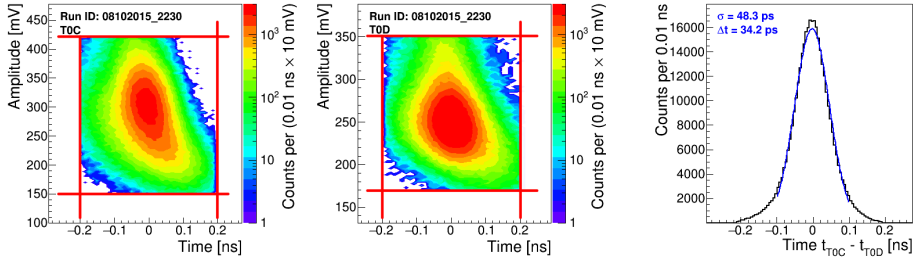


Figure 3.11.: Performance of the trigger detectors at the T10 beamline

and middle plots in Figure 3.11 show examples of amplitude vs. time counting rate plots of trigger detectors: $T0C$ and $T0D$ respectively. The event quality cut was applied so that only the events with the following properties were analysed further:

- amplitudes in mV are in range: $150 < A_{T0C} < 420$ and $170 < A_{T0D} < 350$;
- signal time has to be within 200 ps from the centre of the all-events peak.

The event quality cut is marked with red vertical and horizontal lines. The events, that fail this cut are not plotted. The position of the amplitude peak and the time distribution shape of $T0A$ and $T0D$ signals are slightly different. This is related to the different characteristics of these individual PMTs.

The spectrum of averaged time-of-flight (TOF) for trigger detectors, defined as $0.5 \cdot (t_{T0C} - t_{T0D})$ is shown in the right plot, in Figure 3.11. In case only a single MCP detector was tested, the TOF was used as time reference. The width of the distribution is represented as $\sigma = 48.3$ ps of the gaussian fit. The $\Delta t = 34.2$ ps shows single-trigger detector resolution, assuming both of them are the same.

3.3.2. Selection and optimization of the photosensor

Considering the constraints and requirements listed in Section 3.2, especially high detection efficiency, time resolution, operation in a magnetic field, high radiation levels and compact size, a Microchannel Plate Photomultiplier (MCP-PMT) technology was the natural candidate to be evaluated. Three MCP-PMT sensor models were initially tested:

- Photonis PLANACON[®] XP85012,
- Hamamatsu R10754(X)-00-L4,
- Hamamatsu R10754(X)-07-M16.

They were all found to perform similarly when used for Cherenkov detector application. The ratio of the sensitive area to the total area of the PLANACON[®] is better (81%) than the corresponding value for the Hamamatsu models (69%). The PLANACON[®] sensor has over 4 times larger area for a similar price as Hamamatsu models. Moreover, only Photonis expressed willingness to cooperate with our team to customize the sensor design and introduce the needed modifications.

One way to improve the MCP-PMT lifetime, is to cover the surface of the MCP with a layer of protective material using ALD (Atomic Layer Deposition) technique. Because the lifetime of the sensor is critical for FT0, two additional ALD-coated PLANACON[®] devices (XP85112/A1-Q-L) were tested and compared with their non-ALD-coated equivalents (XP85012/A1-Q). We have found the ALD-coated MCP-PMTs unsuitable for the application in the FT0 [159]. The main problems were:

- low anode current saturation level;
- long gain recovery time after saturation of the device, that is expected to occur frequently during Pb–Pb collisions.

Finally, the PLANACON[®] XP85012 sensor was selected for FT0 [160].

For the application in FIT, the important intrinsic parameter of the photosensor is its quantum efficiency. The high quantum efficiency for wider photon frequencies results in more photons being registered and higher amplitude and charge of the collected signal. The Figure 3.12 shows quantum efficiency as a function of photon energy, as declared by the manufacturer.

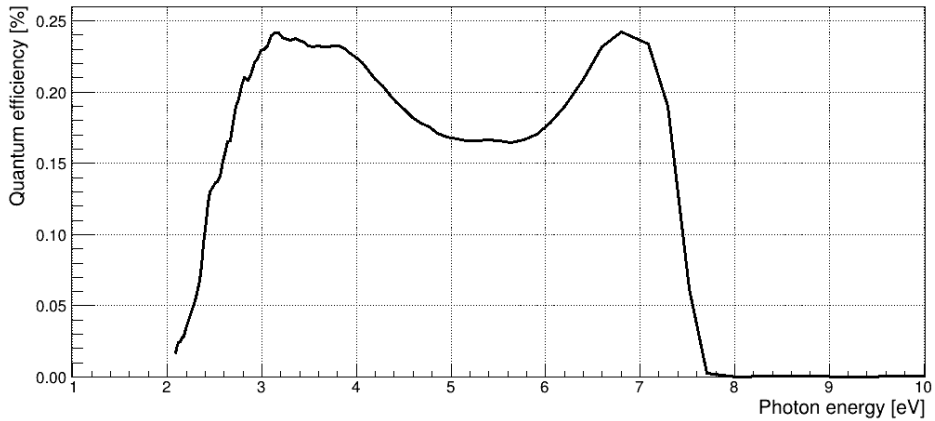


Figure 3.12.: Quantum efficiency of PLANACON[®] photosensors as a function of photon energy, as measured by the manufacturer

The standard PLANACON[®] XP85012 photosensor has 64 outputs, each corresponding to one anode plate, and one common output for the whole sensor. Such a construction makes the sensor quite universal for various applications, including imaging but at the cost of elevated capacitances and inductances between different anode plates and between anode plates and ground. This worsens the signal shape, timing and charge readout characteristics and makes it sub-optimal for the cutting-edge application in FIT:

- An additional PCB is needed to merge the 64 anode outputs into 4 groups. This increases overall capacitance and inductance along signal lines and leads to signal shape distortion, which is position-dependent.
- The MCP electrode is not decoupled by capacitors to prevent changes of the potential on the surface of the MCP block. These changes of anode-MCP capacitance are the source of the positive time-shifted cross-talk visible in the left oscillogram of Figure 3.13.
- The differences in anode trace lengths worsen the time resolution.

To improve the performance of the sensor, the following modifications were introduced by the members of the FIT collaboration from the INR in Moscow. The set of original back-mounted PCBs with 64 outputs was replaced by the three new

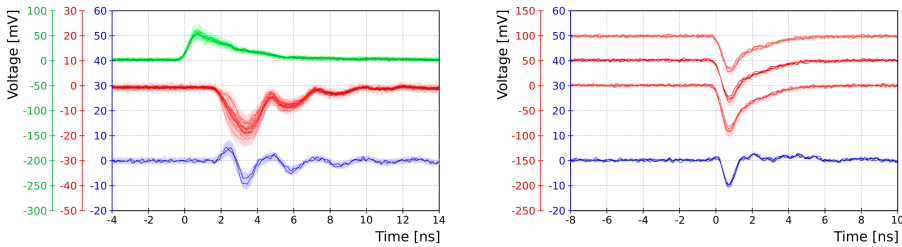


Figure 3.13.: Signal shape of a PLANACON[®] photosensor before (left) and after (right) the modification

PCBs, which directly connect anodes into 4 groups while keeping trace lengths equalized. The new design also uses the MMCX sockets, which are suitable for the RF signal transmission, as opposed to the original simple pin headers. Additionally, the common output was removed. The manufacturer assigned a new designation to the modified sensor, i.e., XP85002/FIT-Q. The modification resulted in the reduction of the capacitance between anode and ground to just 80 pF per quadrant (quarter of sensors active area) and 2 pF between quadrants. The effect in sensors performance is noticeable in the oscillograms presented in Figure 3.13. The left oscillogram shows a typical response of the off-the-shelf sensor. The red line represents the signal from the quadrant illuminated by the laser. The blue line shows the cross-talk in the non-illuminated neighbouring quadrant. The green line is the common signal. The three red lines in the right oscillogram in Figure 3.13 present the behaviour of three illuminated quadrants of the modified sensor. The blue line represents cross-talk visible in the non-illuminated fourth quadrant. Thanks to the modification the signal shape became clean: the positive cross-talk was eliminated, the overall cross-talk magnitude with respect to the amplitude of the main signal decreased by a factor of 5 and the tails don't show ringing anymore.

The reduction of anode capacitance caused the increase of the signal amplitude for the same incident light intensity by a factor of 2 at the same gain of 10^6 .

The outcome of modification of the photosensor is the alignment of the timing of the main signal and the cross-talk. The results of a beam test measurement dedicated to timing studies are shown in Figure 3.14. Based on it the time resolution of the modified sensor is 13 ps. This experimental setup consisted of two modified sensors, which allowed using one of them as time reference while

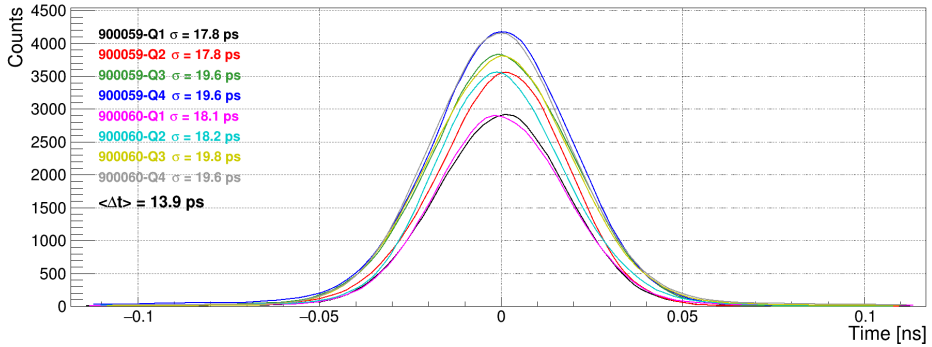


Figure 3.14.: Distributions of time differences between pairs of pixels of 2 modified MCP-PMT sensors, serial numbers: #900059 and #900060. The cross-talk between channels has been removed; the plots show single-MIP response. Assuming the time resolution of all pixels is similar, the resolution of a single pixel is calculated by dividing the widths of distributions by $\sqrt{2}$, i.e., $\Delta t = \frac{\langle \sigma \rangle}{\sqrt{2}}$

the other was being tested. This way less precise trigger detectors were not used for timing.

The time resolution improvement for the main pulse from 34 ps to 13 ps (factor of 2.6) can be deduced from Figure 3.15. It stems from the overall improvement of the shape of islands corresponding to the main single-MIP signal, shown in Figure 3.16. The shape for the off-the-shelf sensor shows slight anti-correlation of time-to-amplitude, while the modified version is almost perfectly symmetric in both time and amplitude planes, showing no correlation whatsoever.

3.3.3. Cross-talk tests

The MCP-PMT entrance window is 2 mm thick. It is uniform across the whole active area. This makes it the main source of optical cross-talk between channels. Also, manufacturing defects in mirror surfaces of quartz radiators and radiator misalignment would lead to optical cross-talk. The principle of optical cross-talk caused by the entrance window is visible in the right picture of Figure 3.17, where light generated by the right radiator leaks to the left-side of the photocathode.

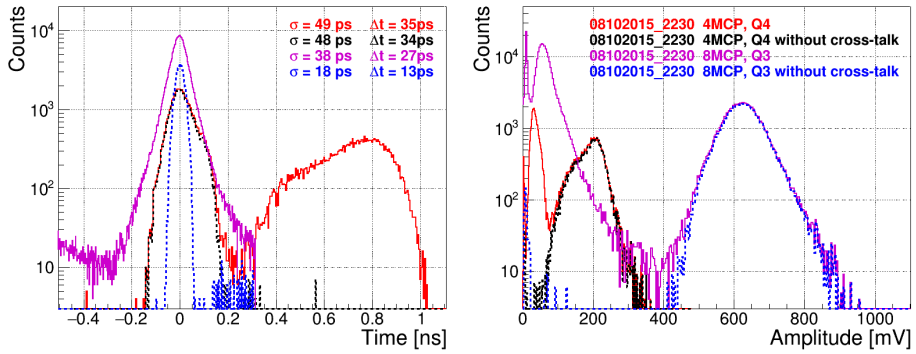


Figure 3.15.: Time (left) and amplitude (right) spectra of the FT0 detector module prototypes using off-the-shelf PLANACON[®] (4MCP) and the modified version (8MCP) including cross-talk (red and violet line respectively) and with single-quadrant selection applied (black and blue dotted curves respectively)

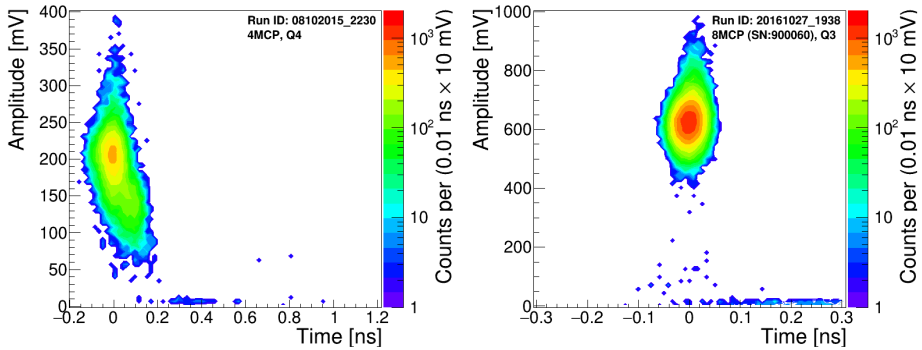


Figure 3.16.: Amplitude vs. time counting rate plot of the FT0 detector module prototypes using off-the-shelf PLANACON[®] (4MCP, left) and its modified version (8MCP, right) after applying single quadrant cuts to reduce cross-talk

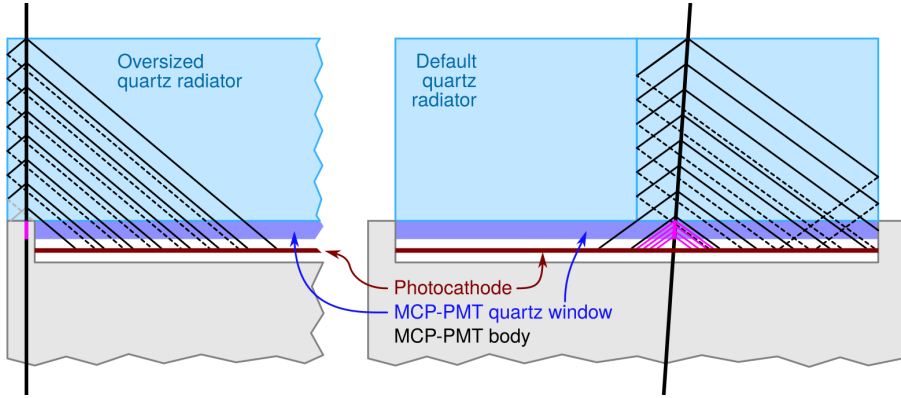


Figure 3.17.: Symbolic scheme of light propagation inside of FT0 detector module using oversized radiator (left) and default radiator (right)

The total cross-talk may be evaluated from Figure 3.15 and is of the order of $\frac{40 \text{ mV}}{200 \text{ mV}} \sim 20\%$. It is the sum of the electronic and optical cross-talk. The upper bound for the latter can be estimated based on the geometry shown in Figure 3.17 as the ratio between the area (or length) of the part of photocathode illuminated by the light coming from the neighbouring quadrant to that corresponding to the whole quadrant. It is $\frac{4 \text{ mm}}{26.5 \text{ mm}} \lesssim 15\%$. This indicates the electronic cross-talk is smaller than the optical cross-talk.

Once the origin of the cross-talk was understood, an algorithm to reduce it was developed. It is called single-quadrant cut and it has been applied, in addition to trigger cuts (see subsection 3.3.1), to analyse most of the beam test data. To study the response of a single quadrant (pixel) of the PLANACON[®] MCP-PMT, it was required that in the other three pixels the amplitude of the signal was low. This procedure reduces cross-talk-induced background. Such a cut represents the operation of the detector module at low particle fluxes and allows to understand the standalone performance of a single pixel. An example of a 2D amplitude vs. time counting rate plot, its cross-talk-reduced version, and its 1D projections is shown in Figure 3.18, Figure 3.16, Figure 3.15 respectively for both modified (see subsection 3.3.2) and off-the-shelf version of the photosensor. The single-quadrant cut efficiently removes the low-amplitude island of cross-talk, while preserving over 94% of high-amplitude pulses.

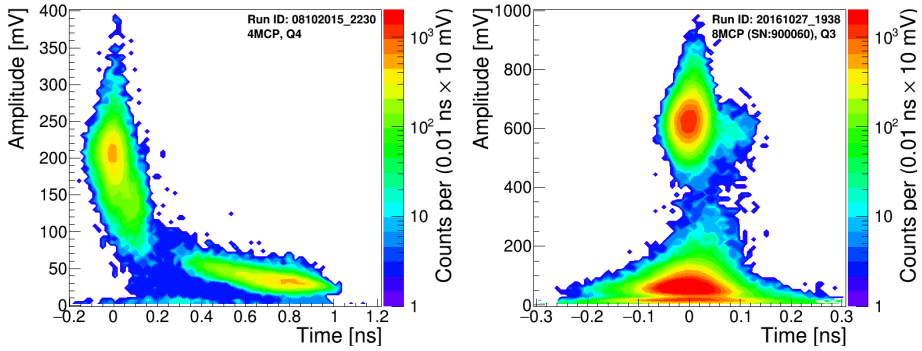


Figure 3.18.: Amplitude vs. time counting rate plot of the FT0 detector module prototypes using the off-the-shelf PLANACON[®] (4MCP, left) and its modified version (8MCP, right). The selection of shown quadrants is arbitrary, though all of them show similar behavior. Note different time and amplitude scales

3.3.4. Choice of radiator material

We have chosen the Spectrosil[®] 2000 quartz for the radiators due to good light transmission at small wavelengths, where the majority of the Cherenkov radiation spectrum lays. Additionally, the lower the cut-off wavelength is the slower the material degrades due to radiation. The absorption and refractive index of quartz are presented in Figure 3.19. The Cherenkov photons are emitted at the θ angle with respect to the direction of the incident particle:

$$\theta = \arccos\left(\frac{1}{n\beta}\right) \quad (3.3)$$

Where n is the refractive index of the radiator medium and $\beta = \frac{v}{c}$.

Based on the Equation 3.3, using the data from Figure 3.19 and assuming ultra-relativistic particle ($\beta \rightarrow 1$) the maximum Cherenkov photon emission angle inside the radiator can be estimated at $\sim 50^\circ$.

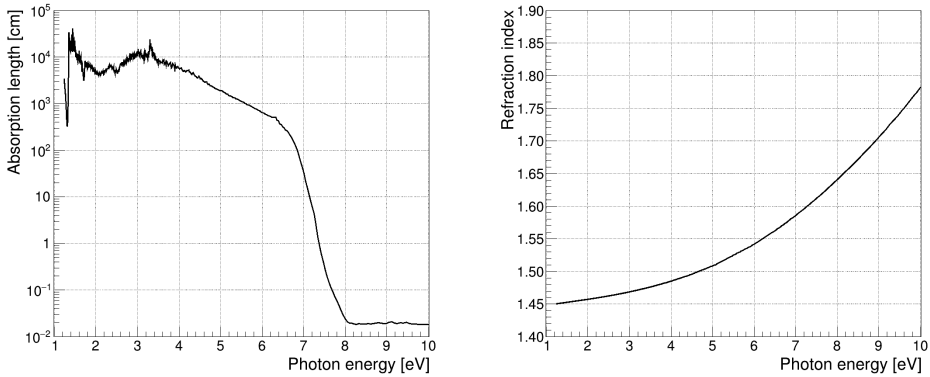


Figure 3.19.: Absorption length and refractive index of Spectrosil[®] 2000 quartz as a function of photon energy, as measured by the Heraeus [161]

3.3.5. Optimization of quartz radiators

While the modified photosensor has four channels corresponding to four quadrants, the optimal size of radiators had to be confirmed by testing a detector module assembled with various configurations of quartz radiators. Considering that about 100 photons is required for reliable detection with a time resolution of 50 ps, the thickness of the radiator was fixed at 2 cm. This thickness includes a 2-fold margin to be able to tolerate the possible reduction of quantum efficiency due to photocathode degradation.

The optimization of the size of the radiator in x and y axes (forming the surface perpendicular to the beam direction) relied on finding the right balance between the number of internal reflections and the possible negative effect of charge collection by multiple anodes. On the one hand, the reflections are undesirable because they reduce the number of photons reaching the photosensor, as the aluminium mirror has a reflectivity of 70–80% for the UV light. Therefore, the excess number of reflections leads to lowering of the sensitivity of the device. The requirements related to particle multiplicity detection (see subsection 3.1.3) exclude a scenario with multiple internal reflections. They also put considerable constraints on the acceptable level of cross-talk. On the other hand, there may be some gain in using a set of smaller radiators, to keep the light more focused, illuminating the section of the photocathode read by a smaller number of anode plates. As anode plates are not identical, their response is expected to differ as well. So limiting

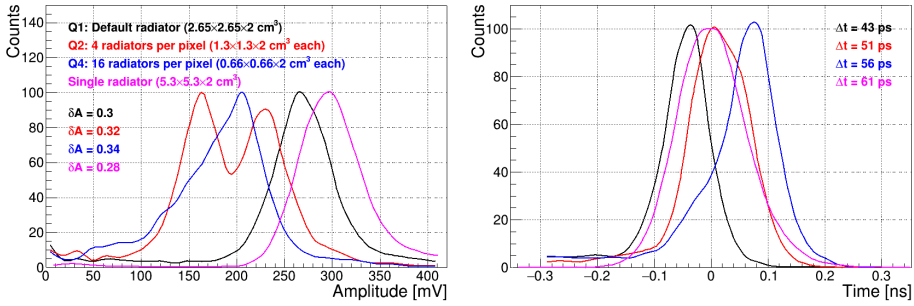


Figure 3.20.: Amplitude (left) and time (right) spectra of the FT0 detector module prototypes using different radiator sizes

the light readout to only a few anode plates could result in less amplitude and time spread of the output signal.

During early detector R&D four configurations of lateral dimensions of quartz radiators were tested. They were coupled to an off-the-shelf MCP-PMT as the modified version was not available yet. The optimal configuration is referred to as default.

- Default configuration of single radiator ($2.65 \times 2.65 \times 2 \text{ cm}^3$) covering the sensors active area corresponding to one quadrant. It is the most obvious solution, that minimizes the number of reflections and amount of cross-talk.
- Two times smaller radiators than the default size ($1.3 \times 1.3 \times 2 \text{ cm}^3$).
- Four times smaller radiators than the default size ($0.66 \times 0.66 \times 2 \text{ cm}^3$).
- A large radiator ($5.3 \times 5.3 \times 2 \text{ cm}^3$) covering the whole active area of a single sensor.

To compare the performance of different radiator sizes a special detector module was assembled using off-the-shelf sensor. Two of its quadrants (Q1 and Q3) were coupled to the default-sized radiators (26.5 mm), one quadrant (Q2) was coupled to the 4 radiators, which were two times smaller (13.2 mm), and the last quadrant (Q4) consisted of 16 even smaller radiators (6.6 mm). After the test, another module with a single radiator, covering the whole photocathode (53 mm) was assembled using the same photosensor. All tested radiators were 20 mm thick. The amplitude and time spectra of the radiator size test data are

shown in Figure 3.20. The line colours (violet, black, red, blue) correspond to the different radiator sizes. The amplitude resolution, shown in the left plot, is defined as the ratio between standard deviation and mean value of the amplitude ($\delta A \equiv \frac{\sigma_A}{\mu_A}$). In the right plot, the time resolutions (Δt) are standard deviations of the time difference between the tested detector module and the reference time (average time of trigger detectors, as explained in subsection 3.3.1). The time resolutions represent convolution of the trigger detector time resolutions and the resolutions of the tested detectors.

It is evident that Q4 and Q2 performed worse than Q1 in all measured aspects:

- Mean amplitude of Q1 is 30% bigger than that of Q4 and 18% bigger than that of the better peak of Q2
- Amplitude spectrum shape of Q4 is wider, with longer tails, while that of Q2 has two peaks that could be related to poor optical contact between two of the four radiators; this hints at the higher risk of assembly errors when more radiators are used
- Time resolution and delay also worsens with decreasing radiator size

The comparison of the default radiator size (Q1) with the single-radiator module is not straightforward. The single-radiator module performed better by 10% in terms of amplitude but had 42% worse timing. Since for this test an off-the-shelf version of the photosensor was used, the traces from 64 individual anode pads were not length-matched. Considering that the distance between the corner anode pads and the central ones is more than 30 mm, the average trace length spread of 4 mm is very likely. It would account for about 20 ps of time spread. To conclude, the worsening of time resolution, in this case, should not be attributed to the radiator but rather to the sensor, specifically to its non-uniform time response across very large area illuminated by the single radiator. The major argument against the use of a single radiator design, that would be easier to assemble, is the increased optical cross-talk between quadrants.

3.3.6. Further tests of oversized radiator

The overall detector performance improves with better detector coverage due to increased statistics. While the photosensor has a fraction of inactive area related to the 3 mm thick edges, the radiator could be enlarged to make a hermetic detector design. The left picture of Figure 3.17 shows the symbolic light propagation

scheme in the scenario with an oversized radiator and indicates the problems stemming from it. The two thick lines represent trajectories of charged particles, one vertical and one at an inclination of 4° , which is the maximum expected particle inclination angle for the FT0 (see subsection 3.3.7 for details). The thinner lines correspond the propagation paths of Cherenkov photons, at angle assumed to be 50° (see subsection 3.3.4 for justification). The dashed lines are trajectories of reflected photons. The grey lines represent those trajectories that do not contribute to signal generation because they failed to hit the photocathode. The pink lines show regions where the contribution of Cherenkov light to the output signal (or lack of it) is significant because it is generated inside the entrance window. While the amount of produced light per length of particle trajectory inside of the window is similar to that of quartz radiator, there is one less optical boundary layer, which results in much better light collection from the window, than from externally attached radiator. The effect of boundary layer between the quartz radiator and entrance window is not accounted for in Figure 3.17 for clarity.

To clear up if the oversized radiator would improve performance of FT0 module we have performed beam tests of such a prototype. The tests revealed that the design with an oversized radiator has distorted amplitude spectrum shape and worse time resolution. The reason is the worse light collection and lack of considerable fraction of light generated inside the MCP-PMT entrance window for the particles, which traverse the radiator volume above the insensitive MCP-PMT area. The signal amplitudes from such particles are smaller than amplitudes from particles crossing the central part of the radiator. This difference results in a broadening of the global amplitude spectrum, worsening amplitude resolution and timing and making it harder to separate the signal from the pedestal. The black line in Figure 3.21 shows amplitude spectrum of detector module prototype equipped with four oversized radiators ($29.5 \times 29.5 \times 20 \text{ mm}^3$). The red line is the sum of three Gaussian functions fitted to the experimental data. The first Gaussian corresponds to the main peak at 190 mV. The side peak at 126 mV corresponds to the signal from the regions at the sides of radiator that is above the insensitive area. Finally, the background peak at 29 mV originates mainly from the cross-talk. The ratio of the number of events within the side peak and the main peak of $R = 0.18$ matches the ratio of insensitive sensor area by the total sensor area ($\frac{56 \times 3 \times 4}{59 \times 59} = 0.19$).

While the separation between the side-peak and the background of 3.6σ is sufficient for reliable single-MIP operation, it is completely inadequate for the appli-

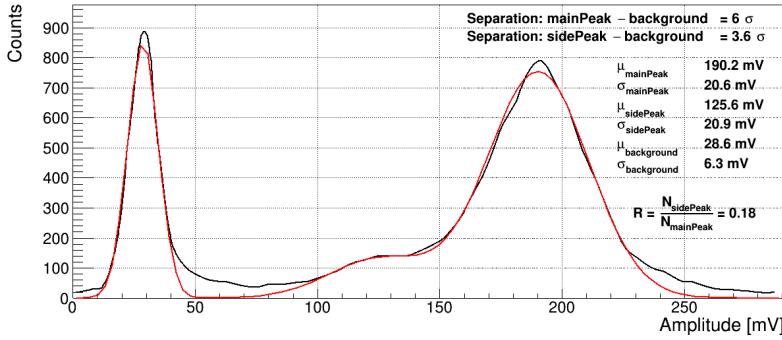


Figure 3.21.: Amplitude and time spectra of the detector module with single enlarged radiator ($59 \times 59 \times 20 \text{ mm}^3$). The red line shows fit of the sum of three Gaussian functions to the data (black line)

cation in FIT, which expects on average about 50 MIPs per pixel in the innermost regions of the array during Pb–Pb operation. In such conditions, the multiplicity resolution would be worse by 34% for fully hermetic design, than for the default one. This performance deterioration comes from the fact that the range of amplitudes reconstructed as one-MIP is wider because it needs to include the side-peak.

3.3.7. Angular response

Once assembled into an array the FT0 modules are directed towards the interaction point. The Figure 3.22 shows incident particle angles relative to the beam direction for each detector module. The maximum spread of incident angles due to the difference in the position of corners of any single module and variation of the primary vertex by $\sigma_z = 5 \text{ cm}$ (σ_z – the average longitudinal spread of beam profile) is also indicated after the ‘ \pm ’ sign. On the C-side the detector modules are tilted to reach average incident particle angle close to 0° . On the A-side the modules are planar and the particle angles reach up to 3.7° . The deviation of incident particle angle from the perpendicular direction of any module is also within the acceptable range ($< 4^\circ$) from the point of view of pulse shape affecting the charge and multiplicity reconstruction.

Higher manufacturing cost of the concave frame for the array on the C-side was

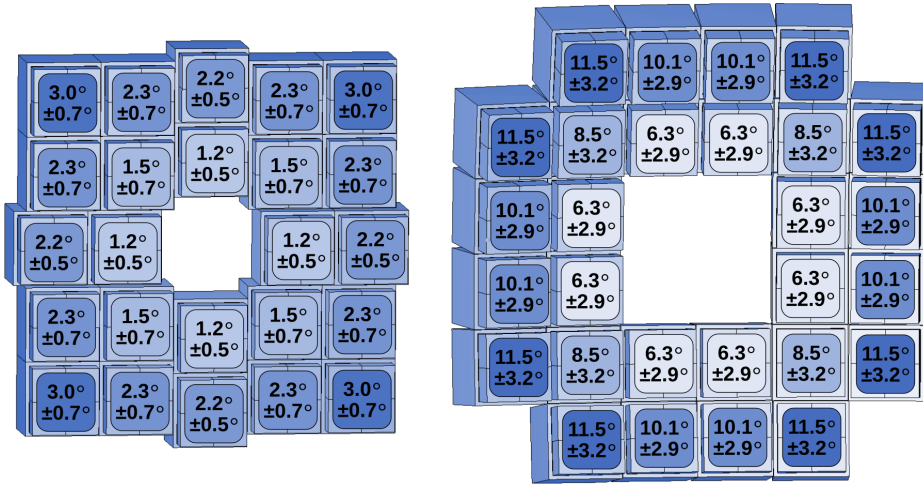


Figure 3.22.: Incident particle angle with respect to the beam direction for each FT0 detector module. Left: FT0-A; right: FT0-C

justified based on analysis of the angular response of the detector module prototype. The Figure 3.23 shows clear degradation of amplitude, amplitude resolution and time resolution when the sensor is rotated with respect to the trajectories of incident particles. If FT0-C were flat the maximum incident particle angle would reach 14.7° . This would lead to approximately 30–40% worse performance. On the other hand, the 4° rotation has minimal effect on the amplitude resolution (4%) and time resolution (5%), and manageable worsening of mean pulse amplitude by only 7%.

3.3.8. Response to the particles travelling in the opposite direction

The particles arriving from the direction different than the IP are considered background and should not be registered. The Figure 3.24 shows the angular response of the detector module prototype to particles arriving from the backward direction. The signal amplitude in this case is only 2% of the default amplitude presented in Figure 3.23 at 0° . No significant change is visible for the range of tested backward angles (180° – 165°).

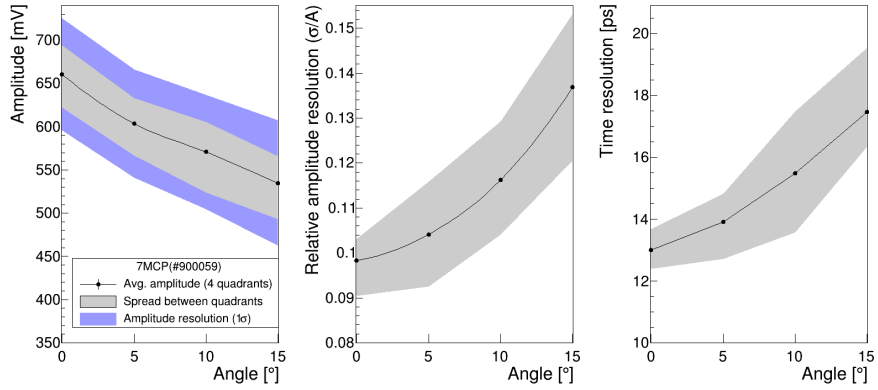


Figure 3.23.: Angular response of the detector module

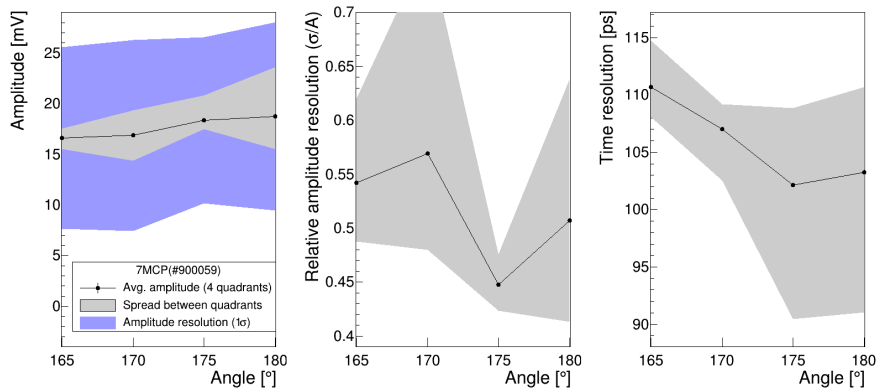


Figure 3.24.: Angular response of the detector module for backward incident angles

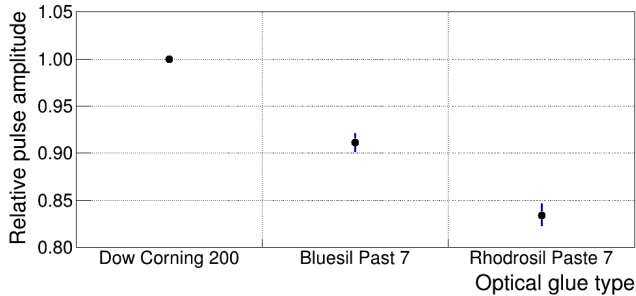


Figure 3.25.: Relative pulse amplitude for different optical grease, as measured at T10 beamline at PS at CERN

3.3.9. Optical grease

The radiators are optically coupled with the entire active surface of the entrance window of the photosensor. The quality of this interface translates directly to the amount of light transported from the radiators to the photosensor, which in turn affects pulse amplitude, amplitude and time resolution.

The results of beam tests at PS of the performance of three optical greases, applied to the FT0 detector module prototypes, are shown in Figure 3.25. Despite Bluesil Past 7 and Rhodrosil Paste 7 are generally recommended for ultraviolet applications, our beam tests (see subsection 3.3.1) revealed that the Dow Corning[®] 200 silicone yields the best results. It is more transparent to UV light in our region of interest or interfaces better with both glued quartz surfaces. Therefore, the Dow Corning[®] 200 silicone was selected. The same grease is used on the top side of radiators to attach the prisms, that belong to the laser calibration system (see subsection 3.3.17), and the black paper around them.

3.3.10. Contribution of the entrance window to signal amplitude

The contribution of the MCP-PMT entrance window, which also works as the Cherenkov radiator, to the magnitude of the signal can be judged by comparing the signal amplitude of detector module without radiators (Figure 3.26) and the default detector module (Figure 3.23). Approximately 8% of the signal recorded by the detector module comes from the entrance window of the MCP-PMT. It

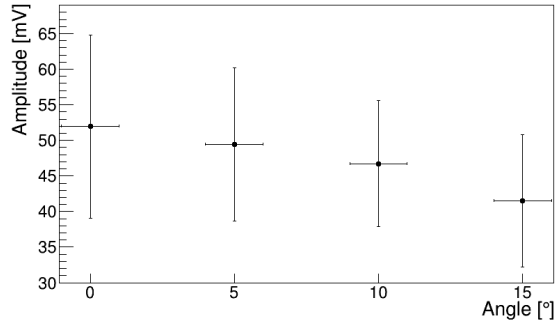


Figure 3.26.: Angular response of the detector module if no radiators are installed. The vertical error bars correspond to the width of amplitude distribution (1σ)

matches the ratio of the thickness of the entrance window of 2 mm to the total thickness of the radiator of 22 mm (sum of the thickness of window and radiator), that is $R_z = 9\%$.

While the direct comparison of these two ratios is not correct, it hints that the optical losses at the interface between the radiator and the window are rather small. To properly compare them the following two assumptions must be made. Firstly, the particle flux throughout all radiators has to be uniform. This condition is met within reasonable accuracy. Secondly, the number of registered photons has to increase linearly with the radiator thickness, which is not strictly true. While the production of Cherenkov photons is linear, their transport is not. The longer their travel distance the more likely they are to be absorbed. Additionally, this effect is wavelength-dependent. It means that the contribution to the signal of the deep-UV photons produced in the window, that is, close to the photocathode, will be greater than for those photons originating in the radiators that need to traverse far distances. To account for it the R_z should be calculated with an effective window thickness instead. The determination of this effective thickness would require a dedicated simulation which is not available.

3.3.11. Gain scan

Most of the T10 beam tests were performed with MCP-PMTs biased with the voltage corresponding to the gain of 10^6 . The main reasons for operating MCP-

PMTs at this gain are:

- At $G = 10^6$ a 1 MIP generates the mean amplitude of 150–600 mV. Such a signal could be connected directly to the digitizer, as the majority of pulse amplitudes fitted within the 10 – 80% of the working input range (0 – 1 V) of the digitizer. The spread in mean amplitude response is due to two factors. Firstly, the modified photosensor shows higher amplitude than the off-the-shelf sensor. Secondly, there is a considerable spread in individual characteristics of different specimen of the same sensor model.
- The noise conditions at the beamline and the ADC resolution of the digitizer excluded precise test runs for signals lower than 50 mV.

While sufficient to compare different configurations of detector modules, such conditions do not reflect the regime, in which the modules will ultimately operate. The gain will be set to a value of 15×10^3 that corresponds to the mean amplitude per MIP of 10 mV at the output of the photosensor. After 30 m long cable the amplitude is expected to drop to about 7 mV at the input of readout electronics. With such a setting the threshold can be set to 4 mV, which covers more than 3σ of the single-MIP amplitude spread. At the same time, it is still separated from the highest detected spikes of 3 mV in the background electronic noise, present in the ALICE cavern (see subsection 3.3.15). In such a regime the 250-MIP (see subsection 3.3.12 and Figure 3.30) signal may reach 2.5 – 3 V. If the gain of 10^6 were used the value of added amplitudes could potentially reach 170 V, which is two orders of magnitude more than the output limitations of the sensor. This would limit the dynamic range and the lifetime of the sensor significantly.

To gauge the behaviour of the detector module at the lower gain, the bias voltage scan was performed. Amplitude, amplitude resolution and time resolution as functions of bias voltage are plotted in Figure 3.27. The highest bias voltage corresponds to 10^6 gain, as declared by the manufacturer. As expected for any photomultiplier tube, the amplitude (proportional to gain) drops exponentially with decreasing voltage. The amplitude and time resolutions become worse with lower bias voltage. Although, it is worth noting that at the lowest measured amplitude of 7 mV the deficiencies of readout used at T10 start to dominate the degradation of measured quantities.

On the contrary to the general-purpose digitizer used during the T10 beam tests, the readout to be used in ALICE during Run 3 is designed to operate at full foreseen dynamic range of output levels of the detector module [162].

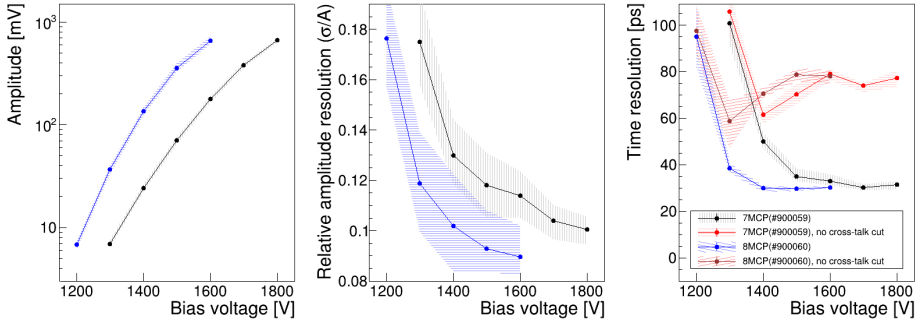


Figure 3.27.: Bias voltage scan showing amplitude (left), amplitude resolution (middle) and time resolution (right) as a function of bias voltage of two specimen of modified PLANACONS[®]

3.3.12. Simulated occupancy and dynamic range of FT0 pixels

The FIT is expected to operate with all available collision systems. The 14 TeV pp collisions are characterized by low average particle densities, reaching about 10 primary charged particles per unit of pseudorapidity, as shown in Figure 3.5. This number rises in p–Pb and for lighter ions, reaching more than 1000 during Pb–Pb collisions. The detector module and readout electronics of FT0 needs to be optimized to cope with these operational conditions differing by more than two orders of magnitude. In the pp system, the detector acceptance and single-pixel efficiency are the most important parameters to maximize trigger efficiency. In Pb–Pb system the high particle multiplicities demand high dynamic range of the detector modules.

To determine the required dynamic range of any single detector module and to quantify its expected ageing (see subsection 3.3.13) a set of simulations was performed. Two simulation frameworks exist for ALICE: the older AliRoot, that is used up to Run 2, and the modern O² that is being developed for Run 3 and beyond. More details can be found in subsection 3.6.1. The simulation results presented in this chapter are based on either one of these frameworks.

The average particle multiplicity per pixel in Pb–Pb is shown in Figure 3.28. The colour-coded z -axis shows that a significant particle density gradient should be expected in most central detector modules on the A-side. The most (least) loaded pixels will see on average ~ 50 (~ 4) charged particles per event.

The analogous information for pp collision system is shown in Figure 3.29. It is clear that during pp operation only a few charged particles in total will pass the FT0 detector per event, stressing the importance of maximizing the efficiency of single modules and acceptance of the whole detector.

The numbers shown in Figure 3.28 and Figure 3.29 are underestimated, because:

- The background is not taken into account. Depending on the final vacuum quality of the LHC, the presence of background (beam-gas and QED) could increase these numbers, especially for the most central modules and if ALICE uses the lower setting of the magnetic field of $B = 0.2$ T.
- Not all material budget was implemented in the simulation framework. This could account for up to 20% increase.

Information about the required dynamic range cannot be extracted from averages. The extrema need to be considered. The Figure 3.30 shows the distribution of the number of charged particles in one of the most loaded, inner pixels on the A-side simulated with the most demanding, central Pb–Pb collisions. Two plots, one for each magnetic field setting at ALICE, are shown. Up to 450 charged particles can be expected in extreme cases. The weaker magnetic field setting of 0.2 T allows more low-energy particles to reach the minimum radius of FT0, increasing the multiplicity there.

3.3.13. Ageing of photosensors

It is understood that MCP-PMT photosensors age mainly due to ion backflow from the anode side towards the photocathode [163–165]. The origin of ions is desorption from the MCP surfaces or the ionization of the residual gas. They drift with the electric field and ultimately they may collide and react with the photocathode degrading the quantum efficiency [166]. Neutral molecules from the residual gas, especially H_2O , O_2 and CO_2 , can also chemically react with photocathode and damage it. Gain may also drop because of the damage to MCP surfaces. The ion generation mechanism is strongest between the MCP and the anode, where the number of electrons is the highest. Ageing is commonly measured as a function of integrated anode charge (IAC) per unit area of the photosensor. The IAC defines the total, integrated over time, charge that the anode has received over the lifetime of the device.

The anode charge from a single collected MIP is:

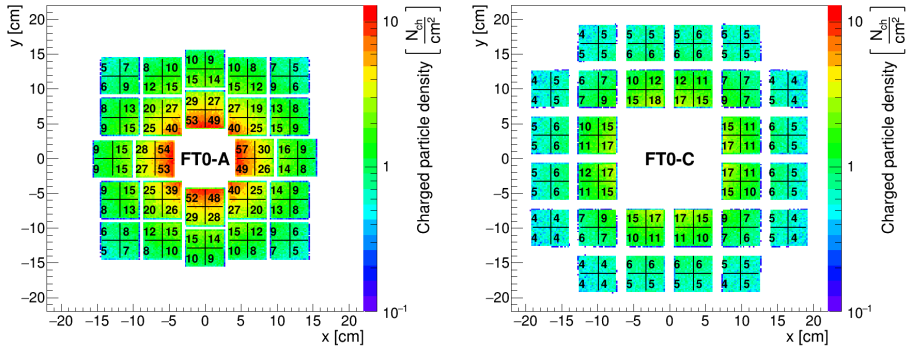


Figure 3.28.: Average number of charged particles per pixel in Pb–Pb at 5.02 TeV in FT0-A (left) and FT0-C (right) detector. Data simulated in AliRoot framework using HIJING. The simulation did not include the complete material budget

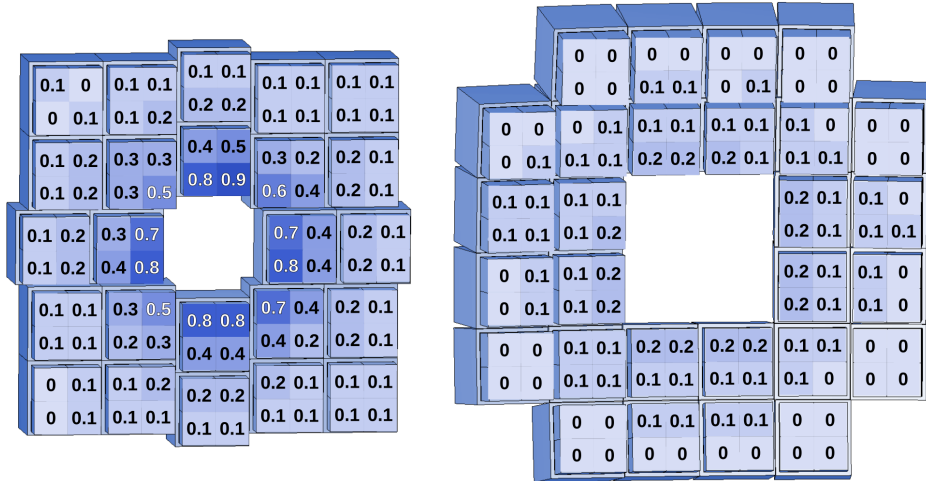


Figure 3.29.: Average number of charged particles per pixel in pp at 14 TeV. Data simulated in O^2 using PYTHIA8

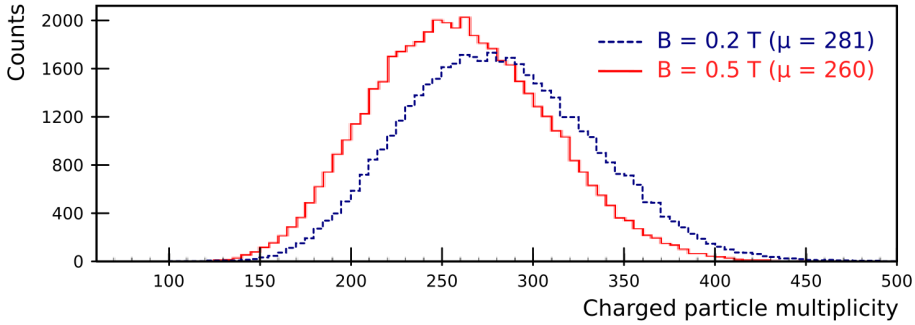


Figure 3.30.: Charged particle multiplicity of the most inner A-side pixel, simulated in AliRoot for Pb–Pb at 5.02 TeV in the centrality range 0–10%. Two settings of magnetic field in ALICE: 0.2 and 0.5 T are shown

$$Q_{\text{MIP}} = e \cdot G \cdot N_{\text{pe}}$$

As stated in subsection 3.3.11 the default gain will be set to $G = 1.5 \cdot 10^4$. A single MIP is confirmed, both experimentally and in simulations, to generate $N_{\text{pe}} \sim 250$ photoelectrons in one quadrant using the final detector module configuration. These assumptions yield $Q_{\text{MIP}} = 0.6 \text{ pC}$.

To complete the calculation of IAC the following are also needed:

- N_{part} – the average number of charged particles per event per quadrant (see subsection 3.3.12)
- $S_{\text{pixel}} = 2.65 \cdot 2.65 = 7.0225 \text{ cm}^2$ – the area of a single quadrant
- $N_{\text{events}} = \epsilon \cdot R \cdot t$ – the total number of events generated during Run 3 and Run 4, calculated as a product of the stable beam availability for physics (ϵ), collision rate (R) and running time (t)

The Table 3.5 shows the parameters needed to calculate the N_{events} . The default running scenario, that has been outlined in the ALICE Upgrade LOI [60], was used as a base to fill t and R in Table 3.5. Since the time the LOI was published, the plan has been revised and the recent proposal extends the pp and p–Pb physics programme, that requires an order of magnitude more statistics

Table 3.5.: Expected ALICE runtimes (t), collision rates (R) and stable beam availability (ϵ), used to calculate the total number of events to be collected in Run 3 and Run 4 (N_{events}) in different collision systems [60]

Parameter	Unit	Collision system		
		Pb–Pb	p–Pb	pp
t	days	90		1380
R	kHz	50	100 (1000)	
ϵ	%	41		50
N_{events}	10^{12}	0.16	0.32 (3.2)	6.0 (59.6)

in these collision systems. The values corresponding to the extended programme are indicated in the brackets. The stable beam availability for physics has been estimated based on the performance of the LHC in the last two years of Run 2. It ranged between 48% and 51% for pp and reached 41% in the Pb–Pb run at the end of 2018. Altogether, the calculated N_{events} are overestimated approximately by a factor of two and represent the upper limits, that try to take into account the contribution from the background and from the fraction of material budget missing in simulations.

The equation to calculate IAC takes the final form of:

$$\text{IAC} = \frac{N_{\text{part}} \cdot N_{\text{events}} \cdot Q_{\text{MIP}}}{S_{\text{pixel}}} \quad (3.4)$$

The N_{part} is taken from Figure 3.28 for Pb–Pb and from Figure 3.29 for pp. Because the p–Pb simulations were not available, it was assumed on average they would produce $s_{\text{p–Pb}} = 8.4$ times smaller multiplicities than Pb–Pb collisions. The value of $s_{\text{p–Pb}}$ can be justified based on the following reasoning. During a Pb–Pb collision two nuclei traverse each others volumes. The longer their overlap the higher the average collision multiplicity is. If we substitute one of the nuclei with a proton, the overlap will be shorter by approximately the ratio of the radius of Pb nucleus (r_{Pb}) to the radius of proton (r_{p}):

Table 3.6.: The contribution to the total IAC presented in Figure 3.31 and Figure 3.32 of different collision systems in the two considered running scenarios

Collision system	Running scenario	
	LOI	Extended
Pb–Pb	59%	13%
Pb–p	14%	30%
pp	27%	57%

$$s_{\text{p-Pb}} = \frac{r_{\text{Pb}}}{r_{\text{p}}} = \frac{1.2 \text{ fm} \cdot 208^{1/3}}{0.85 \text{ fm}} = 8.4 \quad (3.5)$$

The Table 3.6 presents the contribution of each collision system to the total IAC, averaged for all pixels. As the particle distribution differs between Pb–Pb and pp collisions (it is flatter in Pb–Pb but more centrally-focused in pp), the contribution of each collision system also slightly depends on the position of a pixel. Regardless of the running scenario, the pp collisions have about 4% higher contribution in the central pixels than the average and about 4% lower contribution in the outermost pixels.

The total IAC summed for the whole duration of Run 3 and Run 4, including the contribution from the three collision systems: Pb–Pb, p–Pb and pp are shown in Figure 3.31 and Figure 3.32 for the LOI and for the extended running scenario respectively. In the LOI scenario, the inner sensors on the A-side should be expected to tolerate the IAC of up to 1.3 C/cm². The tolerance of 0.4 C/cm² in the outer A-side sensors and all C-side sensors is sufficient. In the extended scenario, some sensors may require replacement during LS3, as their expected IAC reaches over 6 C/cm².

To verify how the performance of the PLANACON[®] photosensor degrades with the accumulation of the IAC a dedicated ageing test was performed at MEPhI. In our test half of the photosensor was uniformly illuminated with the LED light over the period of several weeks and pulse amplitude of the sensor was checked at regular intervals. The other half of the photosensor was covered with non-transparent black paper to block the light. The Figure 3.33 shows the results of

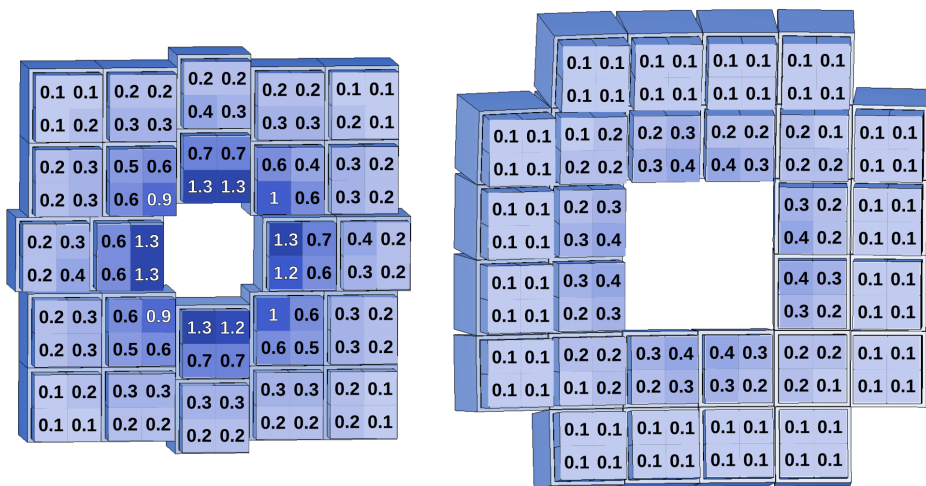


Figure 3.31.: IAC in C/cm^2 for FT0 pixels assuming LOI running scenario in Run 3 and 4

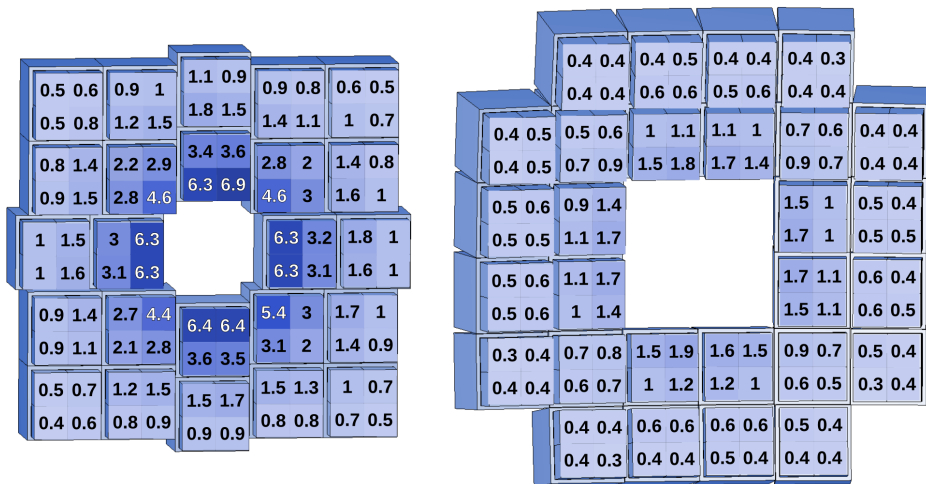


Figure 3.32.: IAC C/cm^2 for FT0 pixels assuming extended running scenario in Run 3 and 4

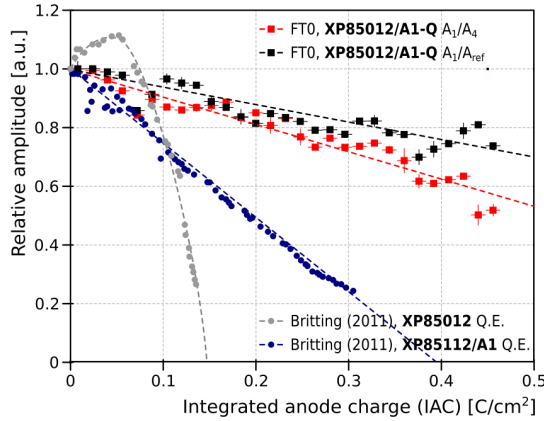


Figure 3.33.: Amplitude as a function of IAC, as a result of ageing test performed at MEPHI [167]

the test. The black FT0 plot represents the amplitude of illuminated quadrant (A_1) relative to the amplitude of non-illuminated quadrant (A_4). Additionally, the laser light intensity was monitored by an independent PMT, Philips 56 AVP, (A_{ref}), that is used as a reference for the red FT0 plot. The light reaching reference PMT was attenuated to ensure no significant ageing and deterioration of its performance during the test. Our results show a steady decrease of amplitude together with accumulation of IAC. Importantly, according to this new measurement we have seen no rapid change in this behaviour, as was reported for the earlier generation of this sensor type by Britting et al. [168].

Such a steady deterioration of the sensor can easily be compensated by increasing the bias voltage, allowing for the required 6 years of reliable operation for almost all of the sensors. Only the 8 – 12 innermost sensors on the A-side may require replacement after 3 years, during the LS3.

3.3.14. Assembly and batch tests of XP85002/FIT-Q

Testing of different sensors of the same or similar type (XP85002, XP85012) at the CERN PS made us aware of the differences between specimens, that could be crucial for the operation of FT0. An overview of the principles of operation of PMTs, that could be useful to understand this section, can be found in

Hamamatsu and Photonis handbooks [169,170]. The list of parameters, that are important for the FT0 operation and are expected to vary between units are listed below.

- **Pulse shape**

The fast-rising edge is required for good timing and the pulse should be reasonably short to allow for high-rate operation without piling up of the charge from the preceding pulses.

- **Resistance of the MCP.**

The stacks of MCPs used in PLANACONS[®] have the total resistance of a few, up to about 50 M Ω . Too high resistance limits the maximum anode current of the photosensor and consequently its ability to operate at high particle multiplicity and high-rate conditions, such as in Pb–Pb collisions. Too low resistance implies higher power consumption and heat dissipation associated with it. Other parameters of the sensor, such as gain and anode current, change with temperature as well. The lower the resistance the longer time is needed for the sensor to stabilise thermally after switching it on. The FT0 needs to be switched off during beam injection to the LHC due to safety reasons. However, it needs to be fully operational, no more than 20 minutes later and well before the stable beam is declared, to perform the functions of trigger and luminometer. This time is the factor limiting how low MCP resistance can be accepted for the use in FT0. Finally, the resistance range of 12–22 M Ω was deemed acceptable.

- **Gain and amplitude vs. bias voltage in B-field (0, 0.2, 0.5 T)**

This is the basic test confirming the correct functioning of the sensor. Adjusting of the bias voltage is the main method to compensate for the loss of amplitude or efficiency, for example, due to ageing, radiation damage or operation in a strong magnetic field.

- **Average anode current (AAC) vs. light pulse rate and intensity**

The MCP-PMT has a limited maximum output anode current. If the sensor operates with high light intensity and high pulse repetition rate the average anode current may reach the maximum leading to the decrease of gain. The FT0 will operate at such conditions especially during Pb–Pb runs, where the most loaded quadrants of A-side will see on average 50 MIPs at 50 kHz repetition rate (see Figure 3.28).

- **Quantum efficiency (QE)**

While knowledge about exact dependence of QE vs. wavelength is not

required for application in FT0, a qualitative verification of QE for each quadrant in response to Cherenkov light spectrum is helpful to reject sensors with possible serious defects of the photocathode.

- **Uniformity of response between quadrants**

Adjustment of the bias voltage is the only way to adjust the gain of the sensor once it is installed in FT0. Because the four quadrants of a single sensor are powered by a single bias voltage any change of bias voltage affects amplitudes in all four readout channels. If there is a significant non-uniformity between quadrants, greater than 50%, then the bias voltage adjustment tuned to suit the lowest-amplitude channel will result in loss of dynamic range of the channels with higher amplitudes.

- **Dark count rate**

The high dark count rate ($\gtrsim 100$ kHz) could indicate problems with manufacturing and long term reliability. The dark counts are not expected to be relevant for FT0 measurement, which operates at low default gain of $1.5 \cdot 10^4$ and relatively high detection threshold of ~ 20 photoelectrons per 0.4 MIPs. A single dark count, corresponding to a single photoelectron, is not sufficient to trigger the detector. If it happens at the time of a real single-MIP detection it will only add an insignificant amount of charge ($\sim 2\%$).

- **Afterpulses ratio**

The afterpulses are a serious problem for a trigger detector. They may cause false triggers following the real pulse after the time of the order of microseconds, i.e., after tens of bunch crossings in case of LHC. The excessive rate of afterpulses is also believed to speed up ageing [164,168]. In FT0 the probability to see an afterpulse within $1 \mu\text{s}$ after an event consisting of a single photoelectron should be less than 0.2% at sensors gain of 10^5 .

- **Long-term stability and reliability of the sensor**

During the tests at CERN PS, we have observed a tendency of some of the new units to permanently change their properties after a sudden discharge inside of the device. After such an event the bias current could start behaving erratically and lead to more discharges, tripping the high voltage power supply and rendering the sensor inoperable due to instabilities. Some units experienced a single discharge, that did not affect their long-term stability. The flawed units needed to be identified and either rejected or sent to the manufacturer for reconditioning.

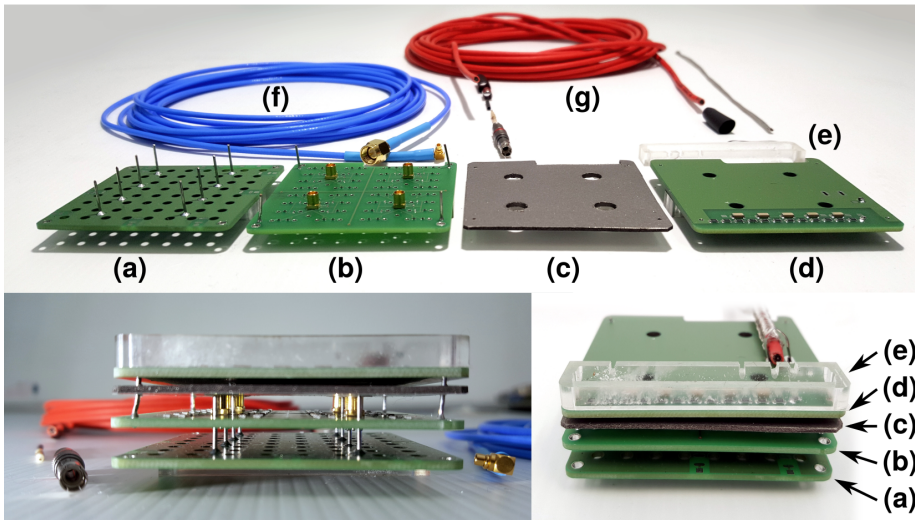


Figure 3.34.: Components for assembly of MCP-PMT arriving from the factory

Before the functional tests measuring these parameters and properties could commence the sensors required manual assembly. The top photograph in Figure 3.34 shows the elements used for assembly of a single sensor. The PCB (a) is used to connect the decoupling capacitors from the MCP electrode to the ground. The ground plane is at the top of the PCB to maximize its distance from the anode pads and minimize the anode-ground capacitance. The PCB (b) joins the 64 anodes into 4 groups connected to MMCX connectors with small form factor and suitable for high-frequency signals. Both PCBs, (a) and (b), are installed to the inner structure of the MCP-PMT at the factory. The bottom photographs in Figure 3.34 show how the elements are stacked during the assembly. The grey (c) sheet is flex EM suppressor, the PCB (d) is the high-voltage divider board (HVDB), (e) is a plastic mould for the compound protecting high voltage terminals, (f) is a coaxial signal cable with MMCX 712-3368 plug on the MCP-PMT end and with SMA 1-1478916-0 connector on the readout side, (g) is a standard high-voltage cable qualified for up to 3 kV, that needs to be fixed and soldered to the HVDB and with HV LEMO FFR.05.403.LLAE141 connector on the other end. The assembly steps required after sensor delivery included:

- Testing the resistivity of 68 resistors and solder joints in PCB (b)

- Connecting 4 solder jumpers (one per quadrant)
 - The PCB (b) is designed with solder jumpers to allow testing by the manufacturer
- Cutting the flex EM suppressor sheet into an appropriate shape (c)
- Preparation of HVDB (d)
 - Testing of the on-board resistors and circuit continuity
 - Fixing and soldering of the red high-voltage cable (g) to the HVDB (d)
 - Soldering and fixing HV plug on the other end of the high-voltage cable (g)
- Final assembly of the sensor
 - Insertion of the EM suppressor sheet (c) on the backside of the MCP-PMT
 - Placing of the HVDB (d) on the backside of the MCP-PMT and soldering the ground pins
 - Glueing the plastic mould (e) for high-voltage compound to the HVDB (d)
 - Soldering the input HV cable and the three MCP input bias voltage cables to the HVDB (d)

After the sensor passed all the tests the high-voltage compound was degassed and poured into the mould to protect high-voltage terminals from humidity and dust, thus preventing a possible increase of leakage currents or sparking. The photograph of a fully assembled sensor and scheme of the high-voltage divider circuitry is shown in Figure 3.35. In the photograph, the high-voltage terminals are properly protected as the high-voltage compound has solidified. The labelled terminals are: U_{IN} – negative input high voltage, U_{cath} – bias voltage for the cathode, U_{MCPin} – bias voltage supplied to the input of the MCP stack, U_{MCPout} – bias voltage supplied to the output of the MCP stack. The anode is not shown as it is at ground level. The highest potential difference is applied between the MCP stack, which is required to multiply electrons. The other elements are biased to a lesser extent, mainly to provide force to drift electrons.

After assembly, the sensors are placed in the 3D-printed housings and into the custom-built light-tight box, where they can be functionally tested and characterized using laser and cosmic muons. The scheme of the setup is shown in Figure 3.36. The violet lines and yellow curves represent optical signals and optical fibres respectively. The red and blue lines correspond to the output signal cable and the high-voltage cable respectively. They are only drawn for the reference

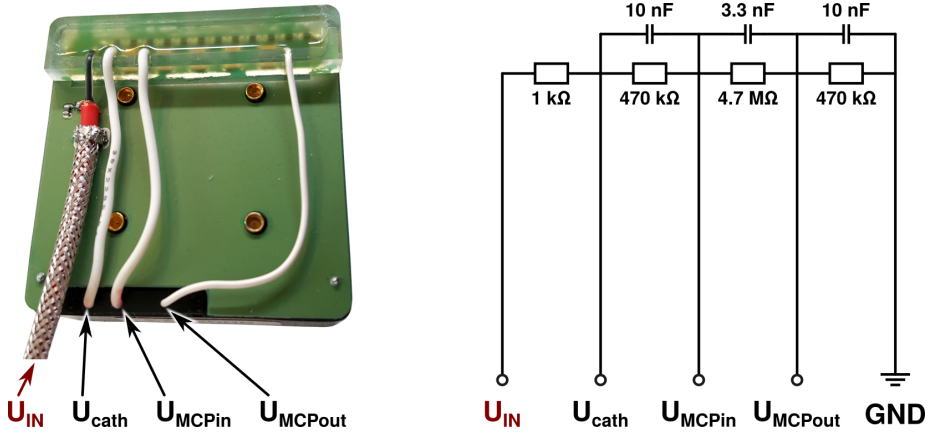


Figure 3.35.: Left: The back-side of fully assembled and tested PLANACON® XP85002/FIT-Q. Right: Circuitry of the high-voltage divider board (HVDB)

PMT in the central compartment for clarity. The 10 high voltage and 40 signal cables from MCP-PMTs (not drawn) follow the same route as yellow optical fibres. The reference PMT is used to normalize long-term instabilities of the laser. Since it is illuminated directly by the optical fibre head the attenuation required on this line is much larger than the attenuation for light delivered to MCP-PMTs, because they receive uniformly-dispersed light, reflected from the white paper attached to the top of the side compartments. The two adjustable mechanical attenuators are controlled by the RS-232 protocol using PC. The high voltage is provided by the three 4-channel high-voltage power supplies, CAEN N1470. The voltage, current and status of each channel are monitored and recorded by the PC running CAEN Gecko control software. The data from the signal of MCP-PMTs is collected either by the oscilloscope or by the digitizer, depending on the type of the measurement. The oscilloscope is more precise, especially at low amplitudes, and it has an adjustable scale extending its dynamic range. However, it only has four channels. The digitizer is less precise but it is more reliable for longer tests and it can work with up to 16 channels simultaneously.

The following measurements are taken for each MCP-PMT:

- **Gain scan and measurement of single photoelectron spectra (SPE)**
The gain scan is needed to verify that the MCP-PMT behaves as expected,

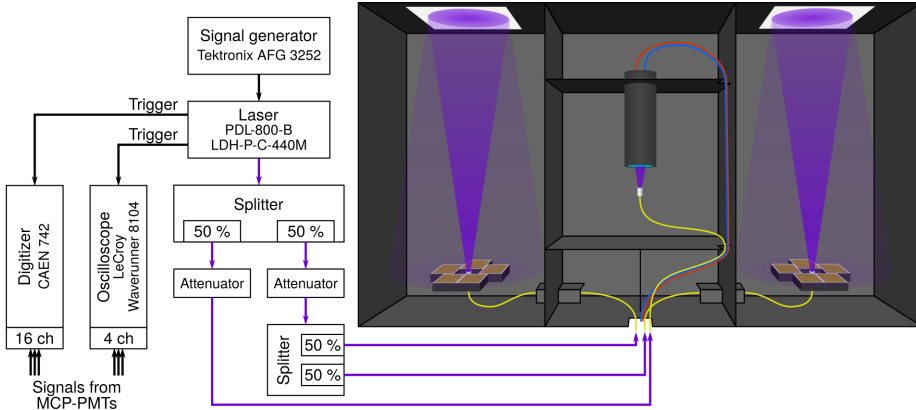


Figure 3.36.: The scheme of experimental setup to test up to 10 MCP-PMTs

especially at the bias voltage corresponding to the default gain of $1.5 \cdot 10^4$ and to the gain of 10^6 , at which some of the following tests are done. Firstly, a measurement of the pulse charge as a function of the supply voltage is taken at the constant light intensity. At the highest voltage, the light intensity is reduced to a level, at which only $\sim 10\%$ of triggers generate the signal at the MCP-PMT output. This way the $\sim 90\%$ of triggered events with a signal are caused by single photoelectrons. The mean charge of single photoelectron from the SPE spectrum ($\overline{Q_{\text{SPE}}}$) is used to translate the pulse charge obtained during the gain scan at the highest voltage ($Q_{U_{\text{max}}}$) to the number of photoelectrons following the formula: $N_{\text{pe}} = Q_{U_{\text{max}}} / \overline{Q_{\text{SPE}}}$. Consequently, the gain can be calculated. All the other measured charges (Q_i) can also be converted to gain G_i , assuming that the response of the MCP-PMT is linear, following Equation 3.6.

$$G_i = \frac{Q_i}{50e \cdot N_{\text{pe}} \cdot \frac{A_i^{\text{ref}}}{A_{U_{\text{max}}}^{\text{ref}}}} \quad (3.6)$$

The factor $\frac{A_i^{\text{ref}}}{A_{U_{\text{max}}}^{\text{ref}}}$ is meant to normalize the instabilities of the laser using independent measurements of pulse amplitude in the reference PMT. The factor 50 represents the input impedance of the oscilloscope and it is used

to convert the charge Q_i in Webers [Wb] to Coulombs. The e is the single-electron charge.

The automatic analysis software has been developed for this step. The test results from single MCP-PMT are shown in Figure 3.37. The SPE spectrum of one quadrant is shown in the top plot. The black asterisks represent the experimental data and the red curve is the result of the best fit of the sum of two Gaussian functions and an exponential function. The first Gaussian is fitted to the pedestal. The exponential function is needed to broaden the tail of the pedestal peak. The second Gaussian is fitted to the single photoelectron peak. The excess of data at the tail represents the two-photoelectron contribution, which is negligible. The mean charge ($\overline{Q_{\text{SPE}}}$) is calculated as the difference between the mean of SPE peak and the mean of pedestal peak.

The gain as a function of bias voltage is presented in the bottom plots of Figure 3.37. The left plot shows the full measured range of bias voltages. The data points are fitted with two functions: exponential for lower voltage and with the third-order polynomial for higher voltage. The fit is just to guide the eye. Because the data is plotted in logarithmic scale the differences between quadrants, represented by different colours, are not obvious. The right figure is plotted in linear scale and it focuses on the region of the default gain of $1.5 \cdot 10^4$, marked by the grey dashed line. Here the differences between quadrants in gain for the fixed voltage are clear, reaching up to 15%. The MCP-PMT #2152 behaves typically. The largest spread of gain between quadrants reaches 70% for the worst unit (#2153).

- **MCP resistance as a function of time after powering up**

The resistance of the MCP-PMT changes with time as it heats up. Many other operational parameters, including gain and current consumption, change with resistance. It is important to verify that in terms of gain all sensors used in FT0 have relatively short time constant of less than 20–30 minutes. Out of the majority of all the delivered sensors (62), time constant varies between 3.3 and 27 minutes. The example of the plot of MCP resistance and amplitude as a function of time is shown in the Figure 3.38. The MCP-PMT was powered up at the time = 0 and the light intensity was constant. The formulae used to fit the curves to the data and extract the time constants, separately for resistance and amplitude, are also shown. The two time constants are different because the amplitude depends non-linearly on the gain, which in turn depends on the voltage supplied to

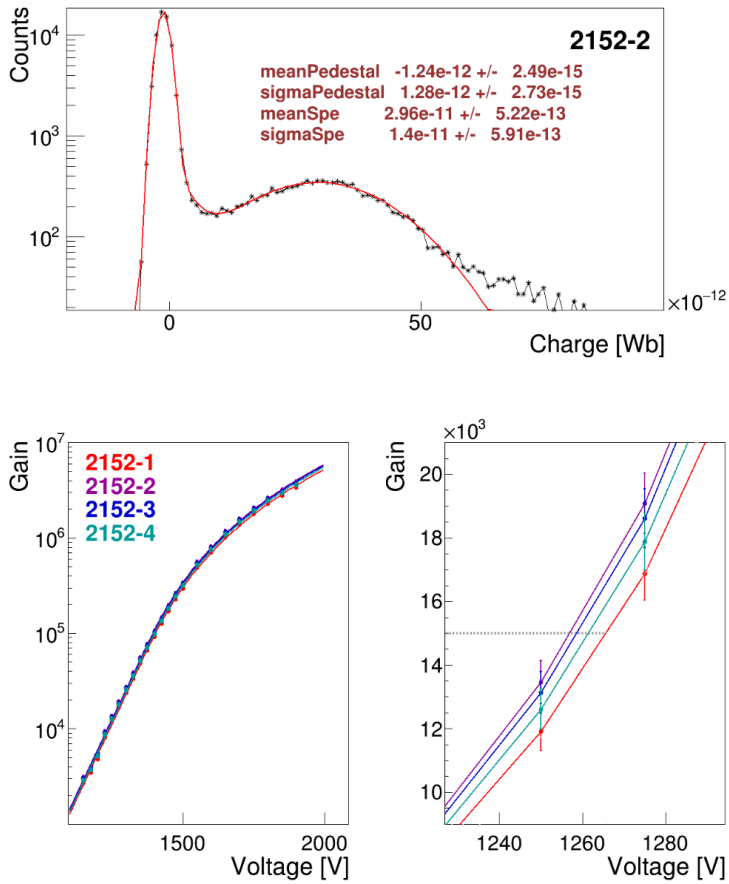


Figure 3.37.: SPE spectrum (top) and gain scan (bottom) results for the MCP-PMT #2152

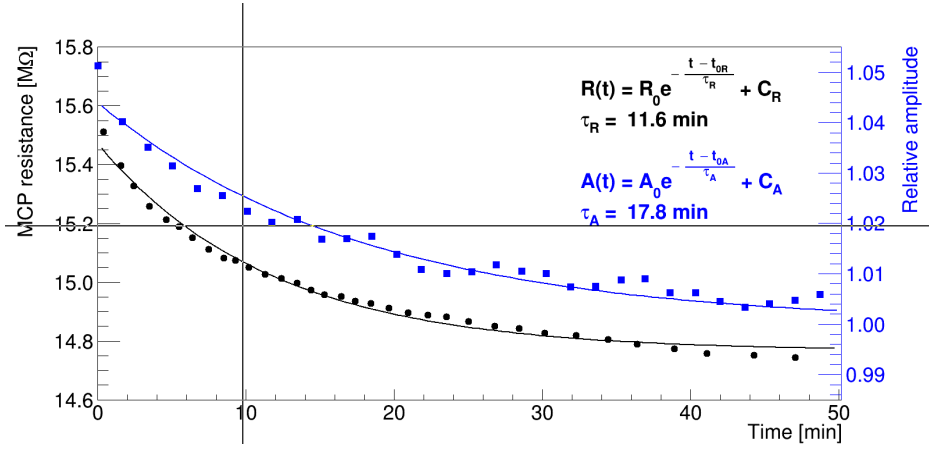


Figure 3.38.: MCP resistance and pulse amplitude as a function of time after the MCP-PMT #2125 has been powered up (at $t = 0$)

MCP. The MCP voltage depends on the high-voltage divider board shown in Figure 3.35 and on the resistance of the MCP stack (between U_{MCPin} and U_{MCPout}).

- **Anode current saturation limit**

With high incident light intensity or high pulse repetition rate, as expected in FT0, the output of MCP-PMT saturates. In such conditions, the gain decreases and linearity can no longer be guaranteed. When a large number of secondary electrons is released from the channel walls the electric field inside the channel becomes distorted and diminished, leading to suppression of further electron multiplication. The missing charge is replenished by the strip current flowing through the channel walls to the regions with a depleted number of electrons. However, this process takes a substantial amount of time because of the high resistance of the MCP. During this time the gain is decreased. A similar mechanism of weakening and distorting of the electric field by the large number of secondary electrons is also relevant for the region between the output of MCP and the anode.

The preliminary measurements of anode current as a function of repetition rate in the absence of magnetic field were performed immediately upon delivery to verify that every MCP-PMT unit is within the specifications

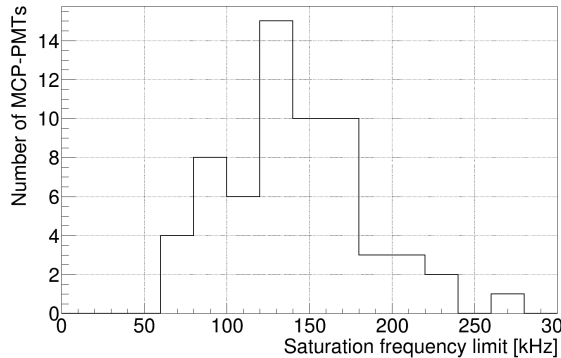


Figure 3.39.: Saturation frequency limit of a sample of 62 photosensors

requested from the manufacturer. The gain of the photosensors was set to $1.5 \cdot 10^4$ and the light intensity corresponded to about 50 MIP. In this study, the saturation limit has been defined as the frequency, at which the gain changes by more than 33%. The Figure 3.39 shows the distribution of the anode frequency saturation limit for a sample of 62 accepted MCP-PMTs.

An extended set of tests for several units was performed in the magnetic field. The results of these tests were used to select the units with the highest anode current saturation limit for the most loaded regions of FT0-A. The further discussion on the behaviour of MCP-PMTs in magnetic field is presented in subsection 3.3.16.

- **Afterpulses and dark count rate**

The ratio of afterpulses and the dark count rate were measured simultaneously at 10^6 gain. Each pulse of light delivered to the MCP-PMT was equivalent to a single MIP. The pulse repetition rate was 100 Hz to avoid any saturation effects and provide ample time for the sensor to relax between pulses. The dark count rate was extracted from the part of waveforms, that preceded the pulse. After the pulse, the acquisition window was open for about 700 ns to register possible afterpulses. The left plot in Figure 3.40 shows the distribution of the dark count rate for a sample of 62 accepted MCP-PMTs. One unit with very high dark count rate of 112 kHz can be seen in the batch of accepted sensors. While such a high rate may seem troubling, it is of little concern for the application in FT0. In FT0 single MIP generates approximately 270 photoelectrons and the detection thresh-

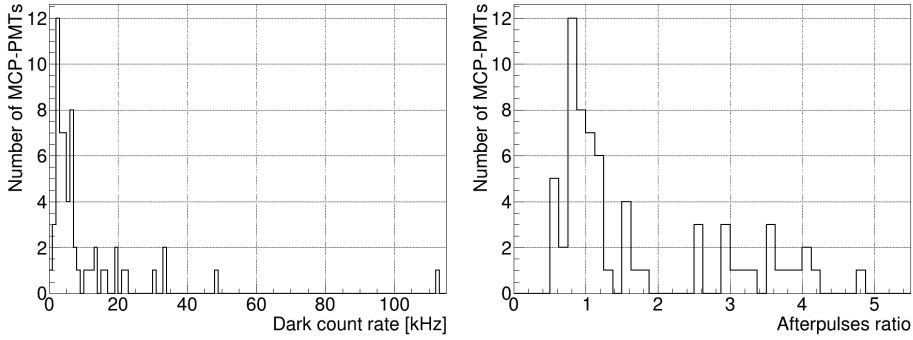


Figure 3.40.: Distributions of the dark count rate (left) and the ratio of afterpulses (right)

old is expected to be set at about 110 photoelectrons. On the other hand, a dark count event corresponds to a single photoelectron. However, higher dark count rates could affect the lifetime of the sensor.

The right plot shows the rate of afterpulses for the 66 accepted MCP-PMTs.

- **Quantum efficiency uniformity for Cherenkov light spectrum**

While the use of laser is convenient due to adjustable light intensity and repetition rate, it does not reflect the real use-case of the sensor in FT0. After installation the sensors will be illuminated by the Cherenkov light, that has a continuous spectrum peaking at ultraviolet wavelengths, not by the coherent 440 nm laser light. The main MCP-PMT parameter, that changes as a function of wavelength, is quantum efficiency. The difference between the response of the sensor when illuminated with the Cherenkov light and with the laser light may reveal issues with quantum efficiency or its uniformity in different quadrants. The estimation of the quantum efficiency uniformity is only qualitative using the method described below.

To test the response of the sensor illuminated by the Cherenkov light, the cosmogenic muons can be used. MCP-PMTs are capable of detecting Cherenkov light generated by a muon passing through their 2-mm thick entrance window. This simplifies the test as there is no need to install external Cherenkov radiators. The two MCP-PMT arrays of 5 units, shown in Figure 3.36, are mounted on top of each other, with a vertical separation of about 10 cm. The arrays are placed into one of the side compartments

of the black box. The laser system is switched off during the muon measurement. The bias voltages are set so that all sensors operate at the gain of 10^6 . The acquisition of a sufficient amount of data, corresponding to about 150 clean vertical muon events per pixel, takes at least 14 hours. The CAEN 742 digitizer is used to collect the waveforms from up to two pairs of vertically located sensors in a single run.

The obtained waveforms were analysed and the pulse amplitudes were extracted. The purity of data is enhanced by implementing two conditions. Firstly, a coincidence between the tested quadrant and the one, that is directly on top or bottom of it is required. Secondly, all other quadrants should show no signal. An average example of the amplitude distributions of four quadrants of MCP-PMT #2158 is shown in Figure 3.41. While the number of counts is still relatively low after 16 hours of data taking, the single-muon peaks are visible. They are fitted with Gaussian function drawn as a blue curve and their mean values (μ) are printed also in blue font. The shown uncertainty represents only the fitting error. The numbers of photoelectrons (N_{pe}), that correspond to the mean amplitudes are also printed. This unit shows relatively good uniformity of amplitudes for Cherenkov light between quadrants. Comparison with similar plots, but using the laser light illuminating all quadrants uniformly instead of muons, could indicate problems in quantum efficiency uniformity for Cherenkov light.

- **Long-term HV stress-test**

Because the FT0-C will not be accessible until the LS3 any replacement of a faulty sensor will be close to impossible. Therefore, the reliability of the sensors is of the utmost importance, and so the long-term stability test was performed for each unit. Because the probability for failure rises with the bias voltage, all MCP-PMTs were biased to the highest voltage recommended by the manufacturer, i.e., equivalent to 10^6 gain. The sensors were kept biased in the total darkness for a period of at least three weeks. During that time the bias voltage and current was monitored. In an event of a serious discharge, the current limits of the power supply were set to trigger an automatic shutdown of the high-voltage channel connected to the failing sensor.

The three examples of sensors behaviour during the stress-test are shown in Figure 3.42. The black line on the bottom shows a typical behaviour. The current consumption is constant across the 2 days covered by the x -

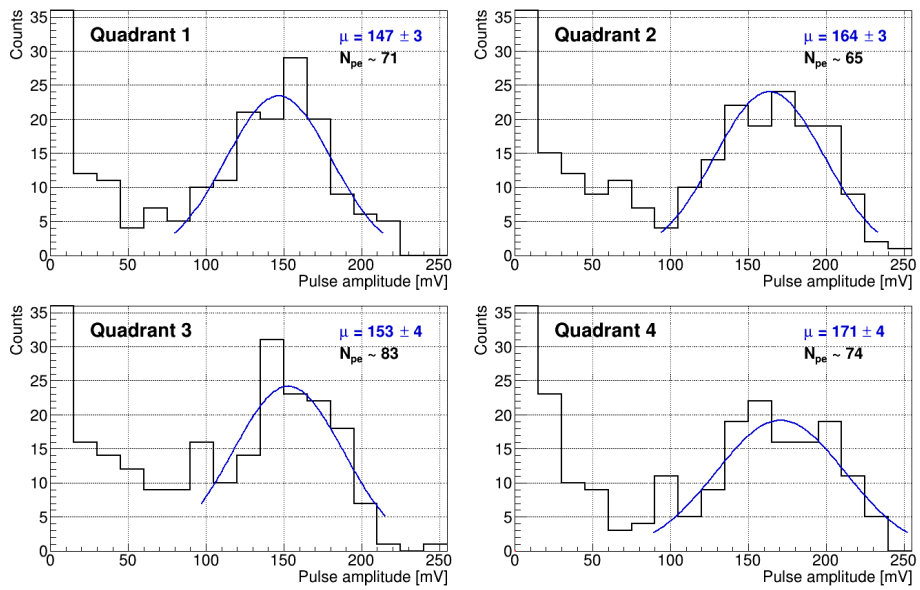


Figure 3.41.: Amplitude spectra of MCP-PMT #2158 [167] obtained using cosmogenic muons

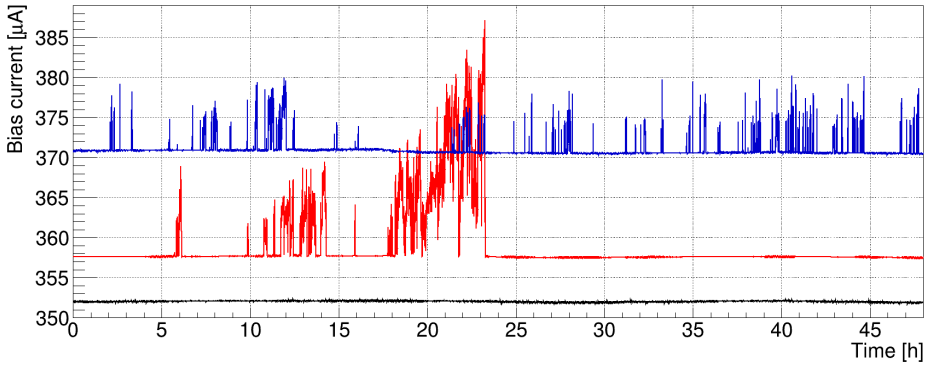


Figure 3.42.: Long-term current consumption of MCP-PMTs biased to the high voltage equivalent to 10^6 gain

axis. The red plot in the middle shows a sensor that was stable during the first 6 hours. Suddenly a set of discharges started happening. At about 23rd hour the sensor returned to a stable operation and remained that way until the test was finished. The blue plot corresponds to a sensor, that was sent to the warranty repairs.

According to the message from the manufacturer, this behaviour could be explained by discharges in the gas trapped inside pores along the edge of the MCP. Such a discharge could decrease the resistivity of the pore, changing the properties of the sensor and increasing bias current consumption permanently. Alternatively, it could have no far-reaching consequences besides the presence of spike in the bias current trend. In any case, the discharges are expected to produce light, that could accelerate photocathode degradation and contaminate detector signal. So unstable sensors, such as shown by the blue plot in Figure 3.42, cannot be accepted for application in FT0, even if their properties remain unchanged.

3.3.15. Real-life tests at ALICE

A prototype of the FT0 module was operational at ALICE from May 2016 until the end of 2018 (end of LHC Run 2 and beginning of the LS2). The module was located just below the T0-A detector, within a few centimetres from the future location of FT0-A.

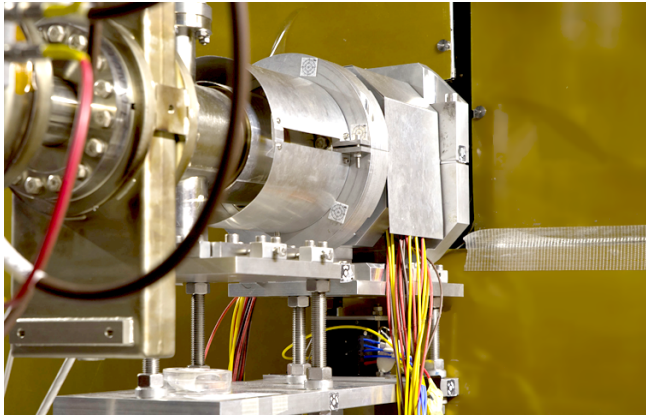


Figure 3.43.: Photograph of the prototype detector module within ALICE (black box on the bottom with 4 blue signal cables extending from it towards the right side). The cylindrical aluminium structure above is the protective cover of the T0 detector [63]

The prototype was read out by the central ALICE DAQ using special front-end electronics boards mimicking T0 timing channels. Due to technical reasons, the amplitude information could not be collected in the same way. Instead, a system similar to that used in the PS beam tests (see subsection 3.3.1), based on the CAEN digitizer, was used. The digitizer was triggered by the $0TVX$ signal. It was independent from the central ALICE DAQ and because of the dead time of CAEN digitizer and high $0TVX$ rates no synchronization between timing and amplitude is available. Additionally, the amplitude-reading system was much slower than the real trigger rate, so only a small sample of events could be recorded.

The main objective of these tests was to evaluate the stability of operation of the module. It was also possible to evaluate the realistic background conditions, the magnitude of electronic noise, interferences from other detectors and systems and infrequent but stress-inducing L3 magnet state transitions between -0.5 and 0.5 T.

Additionally, we could search for any signs of ageing of the detector module over the long-term operation in realistic conditions. The relative pulse amplitude trend recorded by the prototype is shown in Figure 3.44. The changes in running

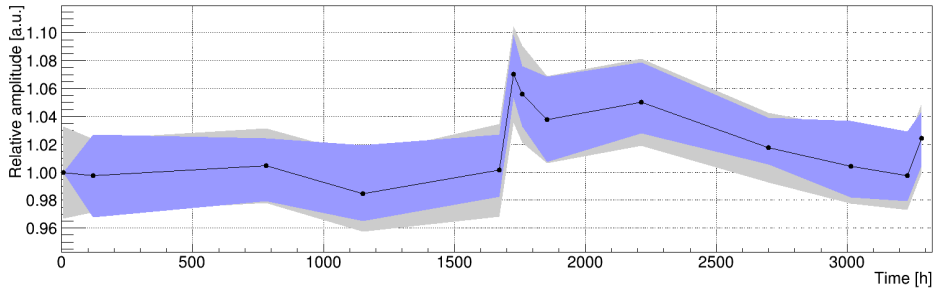


Figure 3.44.: Long-term stability of the detector module prototype installed at ALICE. The grey band marks the uncertainty of pulse amplitude, while blue band represents the spread between 4 pixels

conditions at ALICE are not corrected for, so interpretation of this trend is not straightforward. At about 1700 h there was a malfunction of the cooling of one of the high-voltage crates. It was fixed only at about 3000 h. The conclusion can be drawn that after 138 days of operation there is no visible amplitude degradation within $\pm 2\%$. The upper bound for IAC during this period is of the order of 40 mC/cm^2 .

3.3.16. Sensitivity to magnetic field

Because the response of the photosensor to the magnetic field is anisotropic, both in terms of gain and anode current saturation limit, it was important to measure it for all sensors to verify their applicability in FT0 and to optimize their placement. The Figure 3.22 shows, that on the C-side the outer sensors are tilted by up to 11.5° , so placing sensors least affected by the magnetic field direction there was preferred. On the other hand, the central sensors on the A-side have to withstand the highest particle flux (see subsection 3.3.12), translating into highest-intensity illumination, so for these locations, it is most important to select sensors with the highest anode current saturation limit.

The operation in the presence of a magnetic field of all photosensors purchased for FT0 has been tested using laser pulses [171]. The quartz radiators were not used, as the light propagation is independent of the magnetic field. We have used a 20-ton MNP17 dipole magnet available at CERN EP-DT department. A single MCP-PMT was locked inside a light-tight non-magnetic box. The box was

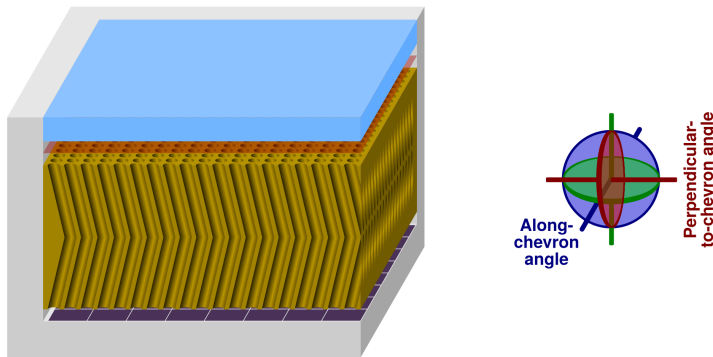


Figure 3.45.: Scheme of inner structure of MCP-PMT and the rotation angle naming convention

placed inside the magnet and rotated in two planes: along- and perpendicular-to-the-chevron angle, marked in Figure 3.45. The operation of PLANACON[®] XP85002/FIT-Q in the magnetic field of up to 0.5 T can be summarized as follows:

- The gain of the sensor changes non-monotonically with increasing magnetic field. To keep the gain constant with respect to the $B = 0$ T scenario, independently from the magnetic field direction:
 - At $B = 0.2$ T the bias voltage has to be decreased by 10–40 V
 - At $B = 0.5$ T the bias voltage has to be increased 50–80 V

The maximum differences between individual sensors in the tested sample of 62 units reach ± 14 V. This maximum spread is similar for both values of magnetic flux density.

- After swapping of the sensor upside-down with respect to the constant magnetic field the performance of the sensor does not change significantly, i.e., the maximum variation of the amplitude is less than 4% regardless of the magnetic field (in the range from 0 to 0.5 T) and bias voltage (from 1100 to 1800 V) setting.
- The response of the sensor to tilting differs depending on the rotation plane. The naming convention of angles is presented in Figure 3.45. The behaviour of two random specimen of the same sensor type is presented

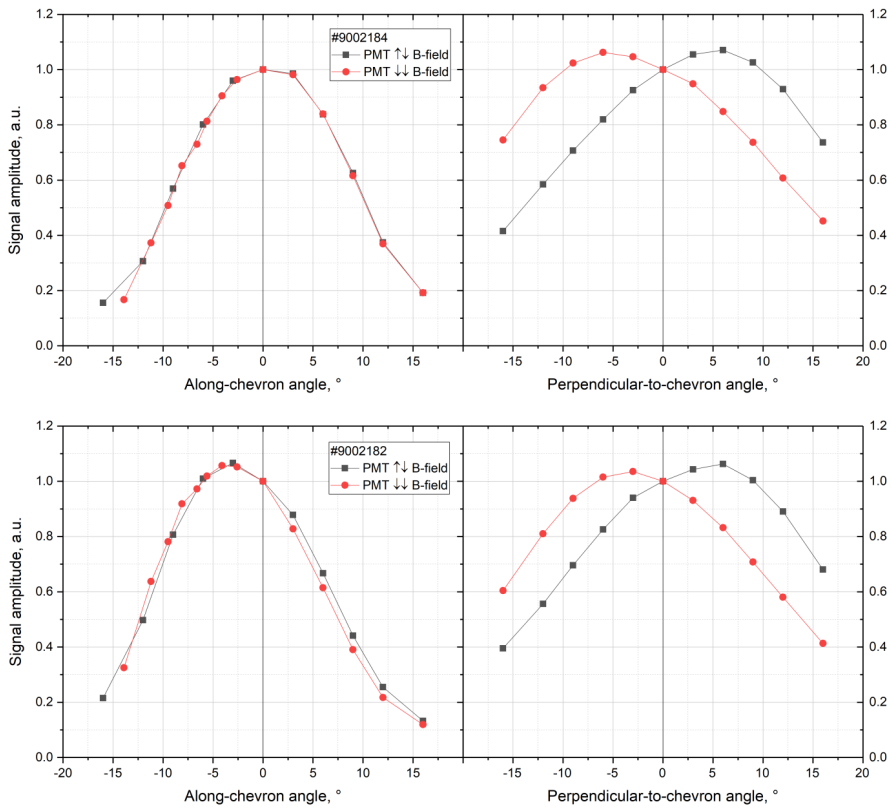


Figure 3.46.: Amplitude response of the PLANACON[®] photosensor in the uniform magnetic field as a function of both tilting angles [167]. The angle naming convention is shown in Figure 3.45

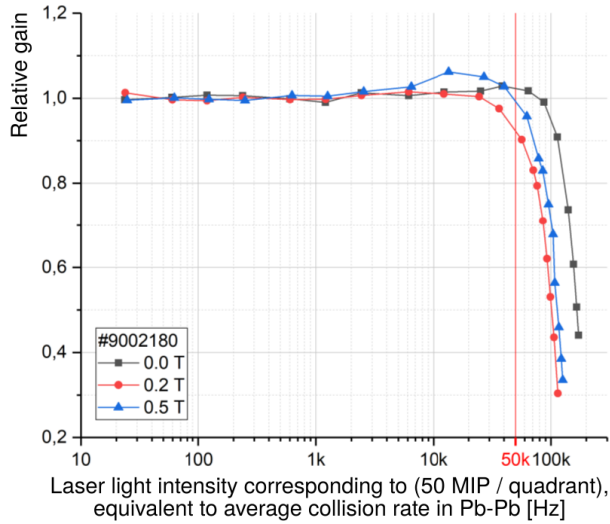


Figure 3.47.: Gain of the PLANACON[®] photosensor in different magnetic fields recalculated as a function of interaction rate. The single-interaction laser light intensity corresponds to the average multiplicity per quadrant of 50 MIP

in Figure 3.46. Tilting in along-chevron angle can yield either symmetrical or slightly shifted response depending on the specimen. The response does not depend on whether the PMT is oriented upwards or downwards. However, such dependence is true if the sensor is tilted in the perpendicular-to-chevron angle.

- Presence of magnetic field reduces the anode current saturation limit. In practice, it means that gain starts to decrease once the limit on the average particle multiplicity detected at high interaction rates is reached. An example of the MCP-PMT gain as a function of interaction rate if illuminated with a light intensity corresponding to 50 MIPs is shown in Figure 3.47. The three curves reflect different magnetic field settings.

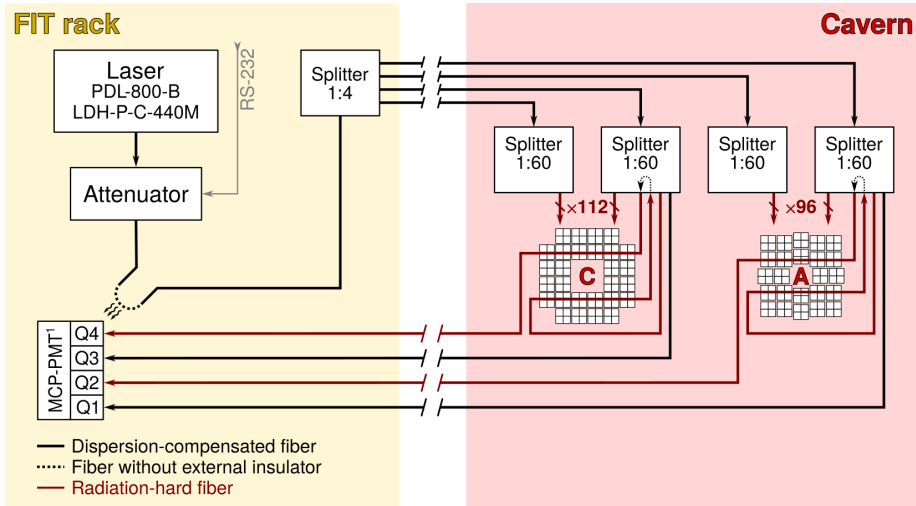


Figure 3.48.: Scheme of the FT0 laser calibration system

3.3.17. Laser calibration system (LCS)

The amplitude response to single MIP is expected to be slightly different for different detector modules. The time delay also may vary. It is caused by:

- intrinsic differences in photosensor characteristics;
- small inaccuracies during assembly, i.e., non-perfect optical grease coupling or misalignment of the radiators;
- slight differences in cable lengths.

To calibrate all sensors consistently, the laser calibration subsystem (LCS) is designed. The scheme of LCS is shown in Figure 3.48. It consists of the picosecond laser driver PDL-800-B [172], laser head LDH-P-C-440M [173], remotely controlled variable fibre optic attenuator (OZOptics DD-100-11-440-50/125-M-35-3S3S-3-1-485:1-12-MC/ RS232-OM2), multi-stage optical splitters and reference or monitoring MCP-PMT. The split laser pulses are delivered to the top faces of quartz radiators by optical fibres attached to small prisms that are used to direct the light towards the sensor. For details see the left scheme and the right photo in Figure 3.49.

The laser operates at 440 nm and it is capable of delivering short (≈ 90 ps) pulses with pulse-to-pulse jitter less than 3 ps. All of the detector pixels are illuminated simultaneously to ensure proper time calibration. The energy of the single laser pulse, according to the datasheet, is adjustable in range from 250 to 625 pJ, that corresponds to $55 \cdot 10^6 - 138 \cdot 10^6$ photons. However, our measurement shows that the maximum power output reaches only $75 \cdot 10^6$. Such power is sufficient for a single laser pulse to reach the amount of light equivalent to that produced by ~ 100 MIPs in each of over 200 detector pixels simultaneously. The light losses at the connectors, splitters, along the optical fibres, etc. amount to approximately 10 dB and they are already taken into account.

To keep the time dispersion of light pulses at the smallest possible level, special dispersion-compensated fibres should be used in the whole LCS. However, as mentioned in Section 3.2 the FT0 detectors will operate in the harsh radiation environment. Because the transparency of such fibres quickly degrades with accumulated radiation dose, the radiation-hard fibres need to be used near the detectors. Their ageing is monitored with the four quadrants (Q1–Q4) of the MCP-PMT¹ connected to a dedicated closed loop of fibre per side. The fibre for monitoring of ageing is routed through the most central region of FT0, where the expected radiation dose is the highest.

The amplitude calibration can be performed using the variable attenuator, that can be remotely adjusted to limit the number of photons reaching the detector. The possible instabilities of the laser output power are monitored by all of the reference MCP-PMT¹ quadrants, as indicated in Figure 3.48. To avoid light losses, that would be inevitably introduced by any additional splitter, we use a simpler solution. The fibre is routed in a loop close to the PMT entrance window and the external insulation of this part of the fibre is removed. It allows for small light leaks, that are proportional to the intensity of transported light, to be registered by the PMT. Additionally, quadrants of the same PMT can be used to monitor the four longer fibres. Such a simultaneous operation is possible because the laser works in the pulsed mode, the lengths of pulses are very short and the delay introduced by the light propagation in the four 80-metres long fibres is sufficient to discriminate pulses from these two different sources.

All the 240 outputs of four 1:60 splitters should be characterized by minimum pulse time and amplitude spread. Each basic building block (1:2 splitter) is designed to split the signal equally between two outputs, however, a spread between individual units of up to 10% is expected. Such a spread, after 8 stages, could result in a factor of 4 difference between the worst outputs. To reduce it, the

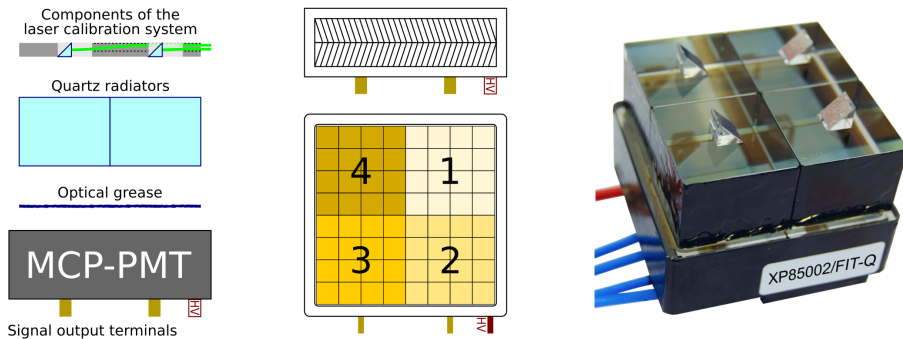


Figure 3.49.: Left and middle: scheme of FIT0 module; right: photograph of semi-assembled module with 4 radiators [167]

splitting ratio and attenuation is measured for each 1:2 splitter after manufacturing. Then, they are arranged to form 1:128 splitter in such a way, that the spread from preceding stage is compensated by the following stages.

A single 1:60 splitter consists of 6 stages (or 63 units) of 1:2 splitters. Because of the high number of splitting stages in the system, it is important to keep the light losses at each stage at a minimal level. This is achieved by splicing the outputs of one stage to the inputs of the next stage instead of using detachable optical connectors.

3.3.18. Final detector design

A FIT0 detector module (Figure 3.49) consists of the MCP-PMT PLANACON[®] XP85002/FIT-Q manufactured by Photonis and optimized by the INR team. The sensor has four outputs, each collecting charge from $1/4^{\text{th}}$ of the area of the sensor (quadrant or pixel). The entrance window of the sensor is optically coupled with four quartz radiators using the Dow Corning[®] 200 optical grease. The position and area of each radiator matches the coverage of each output, so a single radiator is the major source of photons for a single readout channel. The final dimensions of the quartz radiator ($26.5 \times 26.5 \times 20 \text{ mm}^3$) used in the FIT0 detector module, together with relatively wide Cherenkov photon emission angle means that reflections will take place. To reduce the number of absorbed photons

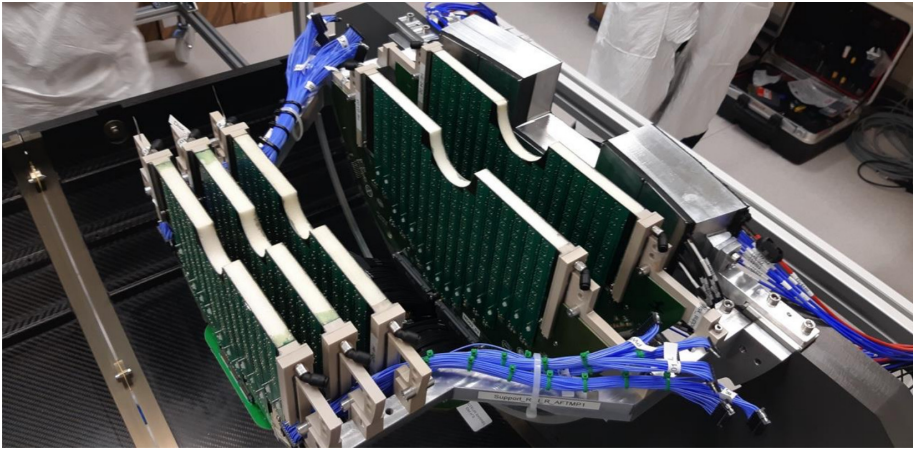


Figure 3.50.: Half of the FT0-C integrated with the MFT support [63]

and improve signal amplitude the sides of each quartz radiator are metallized with aluminium mirrors sprayed using ion-beam. The area of the side of radiator facing IP, that is not connected to the prisms of the laser calibration system, is covered with black paper coupled to the quartz by the optical grease. This is to make the detector insensitive to the photons, that propagate in the opposite direction, by increasing the probability of their absorption. It helps to improve the time resolution by eliminating delayed, back-reflected photons. It also reduces the sensitivity to the beam-gas background. The beam-gas reactions are likely to produce showers of particles not originating from the IP, as they happen with similar probability everywhere along the beam pipe, so they likely hit one arm of FT0 from backwards, in which case they are not detected there.

The modules on the C-side are arranged around the beam pipe and tilted towards the IP to minimize the incident particle angle and avoid signal quality deterioration. The C-side aluminium frame is presented in the left photograph of Figure 3.51. The right photograph shows half of the semi-assembled FT0-C detector. The Figure 3.50 shows the FT0-C integrated with the MFT.

The A-side is further away from the IP, so the incident particle angles are acceptable even if the detector modules are arranged in a planar fashion.

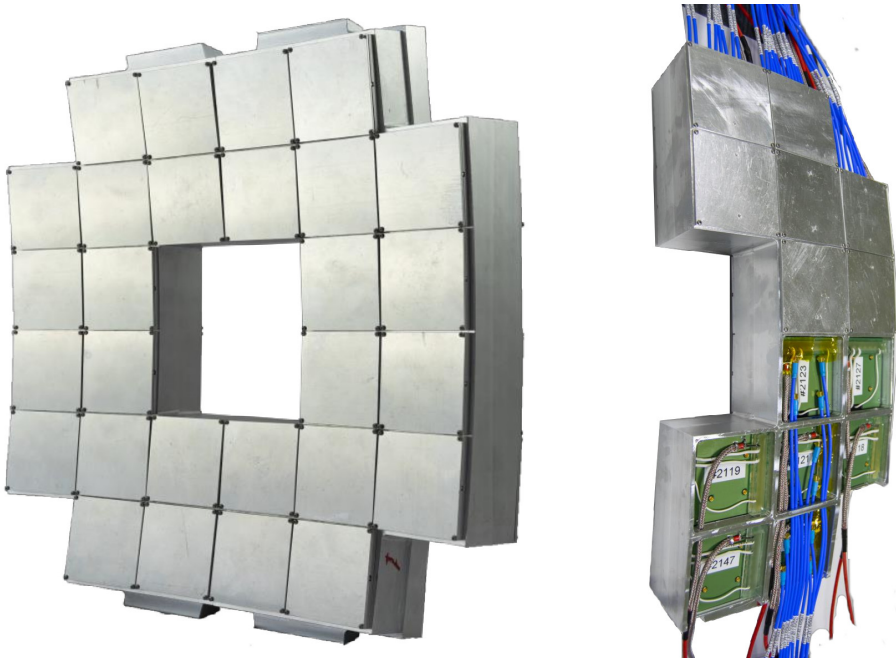


Figure 3.51.: Left: the aluminium frame of the FT0-C. Right: semi-assembled half-array of FT0-C [63]. On the uncovered bottom part the PCB backplanes of 7 MCP-PMTs are visible

3.4. The FV0

Before the LS2 ALICE was equipped with V0 detector [64, 149, 174], which consisted of two scintillator arrays. The one on the C-side was 90 cm away, just in front of the Hadron Absorber of the Muon Spectrometer, and the other one was 3.3 m from the IP on the C-side. Each V0 array was composed of BC404 scintillator cells, that were arranged in 4 rings and 8 sectors (45° each), summing up to 32 readout channels.

The V0 functioned as:

- MB and centrality trigger detector
- Beam-gas background rate monitor
- The detector reconstructing centrality and event plane in Pb–Pb collisions
- Luminometer with up to 10% precision [154].

The time resolution of each readout channel reached about 450 ns (350 ns) for V0-A (V0-C) [174]. The distribution of the sum of amplitudes from both V0 arms was fitted with the Glauber model [114] and successfully used to calculate centrality in Pb–Pb [175], p–Pb and Xe–Xe collisions. The V0 centrality resolution was the best among the ALICE detectors, reaching below 0.5% for the most central Pb–Pb collisions and about 2% for peripheral collisions belonging to 80% centrality class. The event plane resolution strongly depends on centrality with a maximum of 74% (64%) at the centrality of 25% for V0-C (V0-A). See Figure 9 and 10 in the V0 performance paper [174] for more details.

While the performance of the V0 was impressive, the detector also faced some problems, especially with the stability of operation. At the end of 2012, the amplitudes dropped by 10–40% depending on the channel. Several possible sources of slow performance deterioration of V0 were investigated, including ageing of scintillator due to received radiation dose. Finally, it was attributed to the photocathodes of the V0 PMTs ageing at a quicker rate than expected [174]. The system was recovered by increasing the PMT gain by increasing its bias voltage.

Another performance issue was related to the limited dynamic range of V0 channels. It resulted in the need to adjust the PMT gain depending on the collision system. In pp, it was considered the most important to see single-MIPs in every cell to maximize efficiency. In Pb–Pb the priority was given to high-quality reconstruction of the most central events. They are characterized by the high-

Table 3.7.: Comparison between V0 and FV0

Property	V0	FV0
Single-MIP time resolution [ps]	—	~ 200
All-events time resolution [174] [ps]	350–450	—
Amplitude resolution for a single MIP	$\sim 10\%$	
Ageing problem	Yes	Eliminated
Afterpulses	Yes	Reduced
Front-end & readout electronics suitable for Run 3	No	Yes
Number of arrays	2 (A and C)	1 (A only)
Active area in A-side [174] [cm ²]	5275	16243
Active area in C-side [174] [cm ²]	3153	0
Number of channels per side	32	48

est particle multiplicities, that would saturate the detector readout if the PMT gain was set in Pb–Pb the same way as in pp. Therefore, the gain was lowered in Pb–Pb, sacrificing single-MIP detection efficiency, and consequently, the reconstruction quality of the peripheral collisions.

3.4.1. Motivation for an upgrade

For Run 3 and 4 V0 is being replaced by FV0. The comparison between the two systems is presented in Table 3.7. The FV0 is disadvantaged compared to V0 in terms of the number of arrays, as only the A-side could be fitted within the ALICE after LS2. This is partly compensated by the larger area of FV0-A. However, a single array cannot employ effective MB trigger selection or luminosity monitoring, that are based on the coincidence between the sides. Instead, it can be treated as an auxiliary detector, that significantly increases the active area of FT0-A, with an additional benefit of the possibility to monitor the background

level.

The change in LHC running conditions after LS2 required performance improvement of FV0 compared to V0 in the following areas:

- The length of the pulse needed to be reduced down to $\lesssim 25$ ns, otherwise the signal tail could result in the pile-up of reconstructed charge in the next bunch crossing
- The rate of afterpulses had to be reduced to avoid false readings and pile-up
- Time resolution needed to be improved to make it closer to FT0 so that data from both detectors could be combined and used together
- The new front-end and readout electronics needed to be designed for the detector to be operational in the continuous readout mode
- The ageing problem needed to be solved

All of these points have been addressed during the FV0 R&D process. The result is that thanks to the significantly extended acceptance, even a single array of FV0 can reconstruct collision multiplicity well. This is useful for centrality trigger generation, and centrality and event plane reconstruction. The FV0 is located at forward pseudorapidity of $2.18 < \eta < 5.04$, so it measures quantities, which are unbiased with respect to central-rapidity detectors. While ideally, the detector should not be sensitive to the background, it is a hard requirement to achieve by a scintillation detector. Since the FV0 is sensitive to various types of background, it participates in the online and offline estimation of background conditions.

3.4.2. General design

The FV0 is an assembly of 40 optically insulated scintillator cells arranged in 8 sectors and 5 rings with progressing radii. Due to limited space between the IP and the hadron absorber of the Muon Spectrometer the FV0 is located only on the A-side, directly in front of the FT0-A. The front face of its active volume is foreseen to be at $z = 3160$ mm from the IP. All sectors have an opening angle of 45° . The ring radii are listed in Table 3.3. The sketch of FV0 is shown in Figure 3.52. The FV0 employs a novel light collection system [176] described in detail in subsection 3.4.5. The light collected from each cell of the outermost ring (r5) is split to two PMTs – the red-dashed lines indicate the approximate

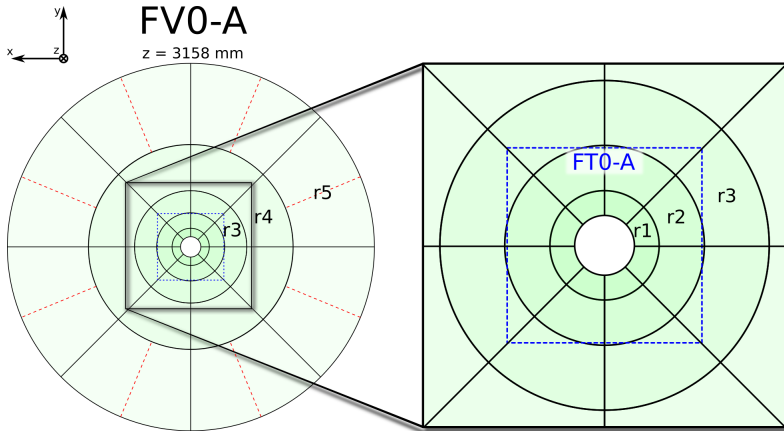


Figure 3.52.: The sketch of FV0 with visible division into 40 scintillator cells

borders between cell regions read out by a single PMT. To emphasize the scale, the envelope of the FT0-A detector is marked with the blue dashed rectangle.

A charged particle traversing a volume of 4 cm thick plastic scintillator deposits approximately 8 MeV of energy in the form of excitation of the scintillator material. It deexcites emitting photons isotropically. The timescale of this process depends on the scintillator type and it is characterized by an exponential decay with a time constant of a few ns to a few hundred ns. The photons propagate through the plastic, they may reflect from any of the white-painted faces and finally reach the clear optical fibres attached perpendicularly to the top face of the plastic scintillator. Some photons continue to propagate along the fibres and arrive at the PMT, either through a 3-mm plastic plate preventing direct contact of fibers with the entrance window (rings 1–3) or through a tapered light guide (rings 4–5). At the PMT they are converted to electrons and amplified. The macroscopic electric charge is extracted at the anode of the PMT by the readout. The schematic cross section of the FV0 detector is shown in Figure 3.53.

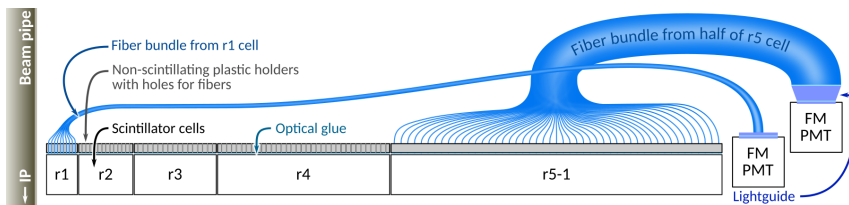


Figure 3.53.: The schematic cross section of the side of FV0 with emphasis on the light collection system

3.4.3. Detector R&D

Various FV0 prototypes have been tested in the National Autonomous University of Mexico (UNAM) with cosmic muons and at the T10 beamline at CERN PS with a particle beam. The tests at CERN were performed in parallel with FT0, so the experimental setup and trigger selection methods were similar, as described in subsection 3.3.1. The following elements of the detector were tested and their performance verified in terms of time resolution or pulse amplitude [176]:

- **Scintillator type**
Amplitude using EJ-204 is superior by nearly a factor of 2 compared to EJ-232. In principle, Bicorn's product, BC-404, performs similarly to EJ-204, however its price is 2.5 times higher. EJ-228 was also tested, but the results were inconclusive, so considering the 4 times higher price than EJ-204 it was rejected.
- **Scintillator coating**
White paint, compared to coating with Tyvek foil and black paper, yields better time resolution by 16% and 61% respectively.
- **Different types and brands of clear optical fibres**
Bicorn, Kuraray and Asahi fibres were tested. Kuraray fibres yielded about 9% better time resolution, but they are over 4 times more expensive than Asahi fibres. The prototype with white-painted Bicorn fibres show 35% worse time resolution than that with Asahi fibres. The Bicorn fibres are even more expensive than Kuraray fibres. Finally, Asahi fibres were selected for FV0.
- **Photosensors**
We intended to use either the PLANACON[®] XP85012 MCP-PMT by Pho-

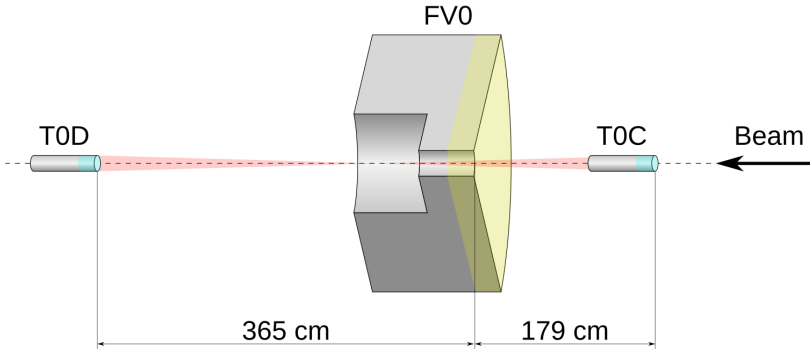


Figure 3.54.: Scheme of experimental setup of the FV0 beam test at T10 at CERN PS. Two fast Cherenkov detectors (T0C, T0D) served as a trigger determining the interaction time and defining beam profile. The FV0 prototype was placed on the movable table allowing for surface scan

tonis, or a Fine-Mesh PMT, so we have tested both options. The advantage of using the same MCP-PMT as in the FT0 would be the possibility to connect both detectors to identical readout electronics. Also, the pool of spare photosensors could be shared between the two detectors, reducing the required number of spares. Although FM PMTs, that were used by the V0, aged relatively quickly, the newest generation of Hamamatsu R5924-70 photosensors was expected to perform much better in terms of ageing. In addition, our tests included two silicon photomultipliers (SiPMs) $6 \times 6 \text{ mm}^2$: Sensl and Ketek, although they could not be considered a viable option because of their unproven reliability, quick ageing and relatively high noise levels. The same detector prototype was equipped with all of these photosensors. The time resolution was similar in all cases. We have chosen the FM-PMT because the tests revealed that it was superior to MCP-PMT in terms of dynamic range. Also, it was a 3 times less expensive option.

The final beam test of the $1/8^{\text{th}}$ of FV0, i.e., the one-sector prototype, was tested at the T10 beamline in 2018. The scheme of the experimental setup is shown in Figure 3.54. The coincidence between two Cherenkov detectors (T0C, T0D) was used as a trigger and the FV0 prototype was mounted on the movable table allowing for the uniformity scan. The photographs of FV0 prototype are shown



Figure 3.55.: Photographs of single-sector FV0 prototype installed at T10 beam-line at CERN's East Hall. The prototype is highlighted with white envelope

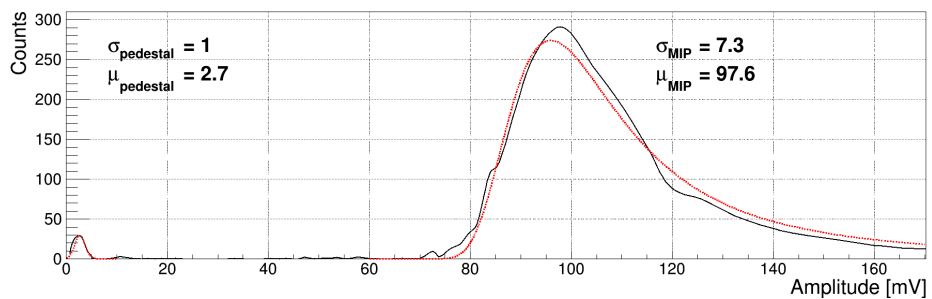


Figure 3.56.: Amplitude distribution of the FV0 prototype [177]

in Figure 3.55.

The amplitude distribution of the innermost cell (ring 1) of the FV0 prototype is shown in Figure 3.56. The position of the prototype was adjusted so that the beam particles selected by the trigger condition illuminated the central region of the cell. The black curve shows the result of the measurement and the dotted red lines correspond to the fitted function, which is a sum of:

- Gaussian function representing pedestal (mean value of 2.7 and $\sigma = 1$)
- Landau function representing the single-MIP peak (mean of 97.6 and $\sigma = 7.3$)

The single-MIP amplitude peak (μ_{MIP}) is well separated from the pedestal. The single-MIP amplitude resolution is approximately 7.5%. The trailing tail originates from Landau distribution and is expected to disappear for multiplicities higher than 10 when the distribution becomes Gaussian.

The uniformity of the whole prototype was tested in terms of amplitude response and detection efficiency. The tests show the single-MIP detection efficiency is 100%, independent from the hit position or cell number. The amplitude varies slightly, especially close to cell edges, but always stays within $\pm 10\%$ of the reference amplitude. Because ring 5 is the largest one, it has the least dense fibre pitch and it is read out by two photosensors its response is more critical and complex than that of the other rings. The left plot in Figure 3.57 shows the mean amplitude as a function of position separately for two photosensors of ring 5. It becomes clear that the ratio of two signals could be used for coarse position determination. The right plot in Figure 3.57 presents the sum of amplitudes from both photosensors for three scanned lines. The detector responds uniformly within 10%.

3.4.4. Plastic scintillator

Each cell of FV0 is machined from a block of EJ-204 plastic scintillator. The characteristic properties of this scintillator are shown in Table 3.8. The EJ-204 emission spectrum is shown in Figure 3.58. The selected scintillator material is characterized by reasonably high light yield. Thanks to it already the 4 cm thickness of plastic provides the sufficient number of photons per MIP for reliable multiplicity reconstruction and good time resolution. The emitted scintillation light lays mainly within the visible range and corresponds to the violet-blue light colour. It is much easier to handle than shorter wavelengths, with better

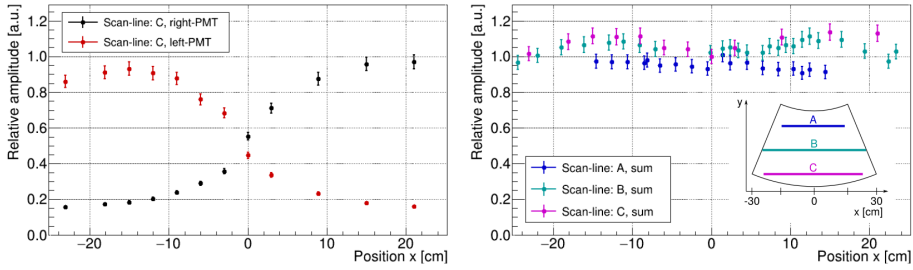


Figure 3.57.: Amplitude uniformity of ring 5 of full-size single-sector FV0 prototype. The left figure shows the relative amplitudes of two photosensors used to read the cell as a function of beam position. The right figure shows the uniformity of amplitude for x-direction swipes at three different y-positions. The inset shows the position of swipes [177]

transmission coefficients for most common materials, meaning lower light losses during light collection and transport. Also, almost the whole emission spectrum matches the plateau of high quantum efficiency of the selected photosensor, shown in Figure 3.63.

3.4.5. Light collection system

The scintillator cells are optically connected with photosensors via clear optical fibres. To hold a large number of fibres and reliably couple them with a scintillator cell an auxiliary 1 cm thick non-scintillating plastic is used. Fibres were inserted and glued into the holes drilled in the plastic. Then the plastic surface and fibre stubs extending from its other side were polished together to obtain a uniform layer. Each scintillator cell was attached to one such plastic-fibres assembly. The loose ends of fibres were bundled, glued together and polished similarly to make a suitable interface with the PMT window. Lengths of all fibres in a bundle from a single cell are equal to minimize the time dispersion of signals and worsening of the time and amplitude resolution.

Depending on the ring the area of the cell changes significantly, while that of the photosensor remains constant. To compensate cells of different rings use different fibre pitch. Moreover, two largest rings use the tapered light guides at the PMT

Table 3.8.: Properties of EJ-204 (FV0) and BC-420 (FDD) plastic scintillators, as published by the manufacturers [178, 179]

Property	Unit	EJ-204	BC-420
Light output relative to anthracene	%	68	64
Scintillation efficiency	$\frac{\text{photons}}{1 \text{ MeV } e^-}$	10400	10000
Wavelength of maximum emission	nm	408	391
Light attenuation length	cm	160	110
Rise time / decay time	ns	0.7 / 1.8	0.5 / 1.5
Pulse width (FWHM)	ns	2.2	1.3
Density	$\frac{\text{g}}{\text{cm}^3}$	1.023	1.032
Refractive index		1.58	1.58

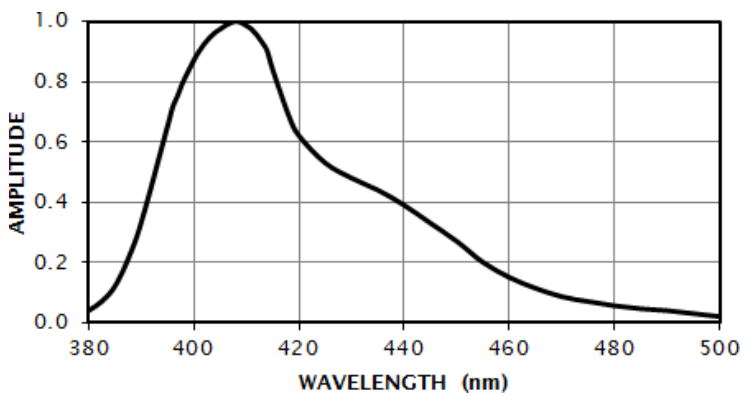


Figure 3.58.: Emission spectrum of the EJ-204 scintillator, as published by the manufacturer [178]

Table 3.9.: Features of the light collection system for cells of different FV0 rings [177]

Ring number	Pitch of fibres [mm]	Presence of light guide	Number of bundles or photosensors
1	3	no	1
2	4	no	1
3	5	no	1
4	5	yes	1
5	6.8	yes	2

Table 3.10.: Properties of Asahi fibre selected for FV0

Property	Unit	Value
Core material		Poly(methyl methacrylate)
Clad material		Fluorinated polymer
Core refractive index		1.49
Core diameter	mm	0.97 ± 0.06
Fibre diameter	mm	1.00 ± 0.06
Attenuation	dB/km	≤ 190

entrance and two PMTs per cell are used for ring 5. The individual features of each ring are summarized in Table 3.9 and presented in Figure 3.59. The optical fibres are not shown for clarity. The colour-coding of pitch grid for ring 4 and ring 5 corresponds to that at the light guides. The 6 large circles represent the PMTs.

Asahi fibres were selected, based on their good performance (see subsection 3.4.3) and very affordable price. The properties of the chosen fibre type are listed in Table 3.10. We have selected the fibre type with large core diameter to maximize the light collection efficiency and ensure a sufficient number of photons emitted by the scintillator can enter the fibre and reach the photosensors. The disadvantage of this choice is the fragility of the thin layer of cladding that is easy to damage mechanically. A small damage could result in light leakage meaning reduction of pulse amplitude and possible cross-talk between fibre bundles connected to

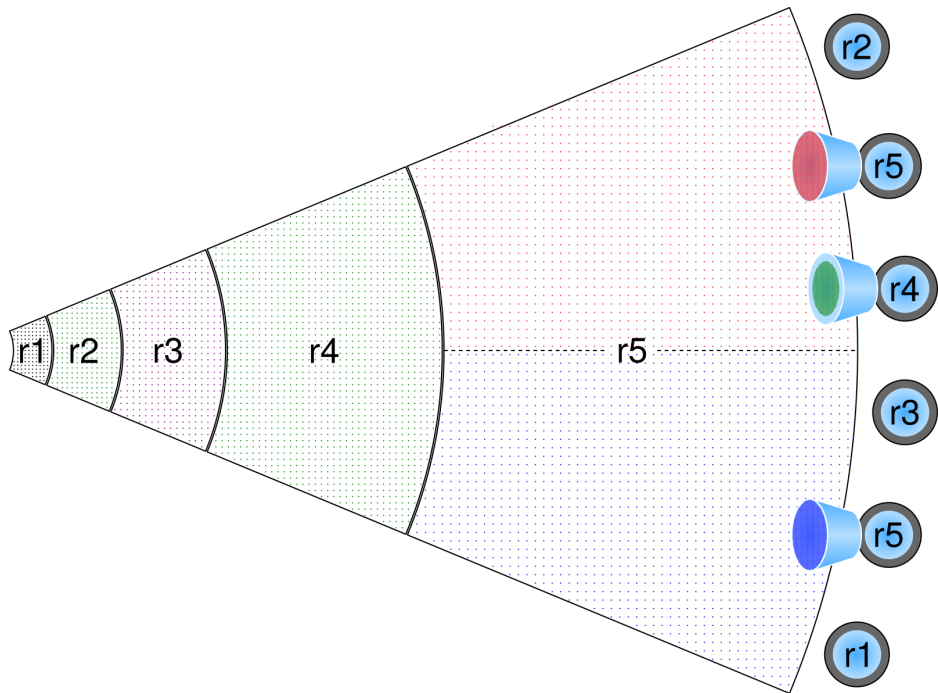


Figure 3.59.: Top view of a single sector of the FV0 with emphasis on the fibre pitch, PMT placement, presence and size of tapered light guides. The fibres are not shown for clarity



Figure 3.60.: Photograph of the semi-assembled FV0 focusing on the PMTs [63]

different readout channels. Thinner fibres would have been more flexible, but they would require denser pitch, making the detector construction and assembly excessively laborious.

The first disadvantage is mitigated by ensuring careful handling of fibres and wrapping the bundles with an additional layer of optical insulation using a black foil (see Figure 3.60). The scale of the second one appears insignificant when compared to other sources of signal time dispersion, especially the nature of the scintillation process, in which the emission of photons is time-distributed.

Moreover, any thickening of the layer of cladding would translate either to thicker fibres or to the reduction of the diameter of the core. The former means the fibres would be more rigid and have a larger bending radius, that would make the detector thicker than allowed by spatial constraints within ALICE. The latter would imply the need for denser fibre pitch and increased total number of fibres, and as a result more expensive and more complicated detector assembly.

The refractive index of the fibre core matches that of the scintillator within 6%. The Dow Corning[®] optical silicone is used to smooth the refractive index at the boundary and reduce light losses due to reflections.

The photograph showing the inner structure of half FV0 is shown in Figure 3.61 and Figure 3.62. The 4-cm white-painted scintillator layer is visible in the bottom. On top of it, there is a 1-cm layer of grey plastic holder and fibres extending from it and guiding the light outwards, towards the photosensors. The red plastic pieces on top are covers for the connectors.



Figure 3.61.: Side view cross section of the FV0 detector [63]



Figure 3.62.: Two halves of the semi-assembled FV0 detector [63]

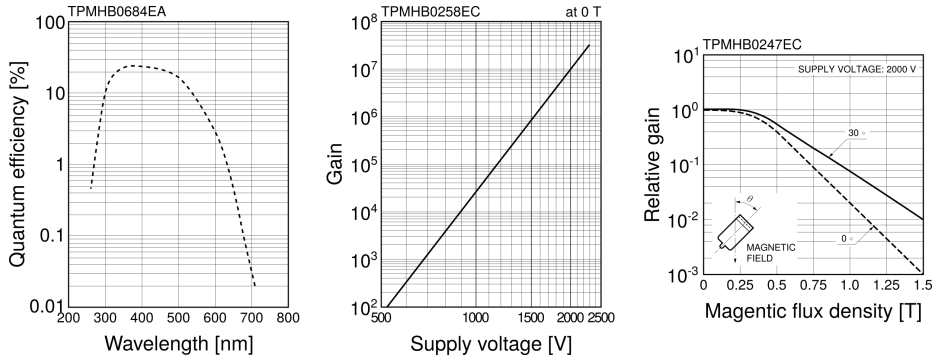


Figure 3.63.: Characteristic plots of the Hamamatsu fine-mesh PMT R5924-70: quantum efficiency as a function of wavelength (left), gain against bias voltage (middle), gain response of the photosensor in the magnetic field (right). The figure is based on [180]. The left and middle plots also apply to R7761-70 used by the FDD

3.4.6. Photosensor

The photosensors form a ring beyond the outer edge of ring 5 of scintillator cells. There is no space for the PMTs in the inner, depressed region of the FV0, because it should be thin enough to reserve a place for FT0-A and as light as possible to reduce secondary particle production. The outer location of PMTs is beneficial also because the further from the beam axis, the lower the radiation levels are during the LHC operation. The risk of radiation damage of PMTs is lower there. The same argument is valid for the fibres, which are routed from the scintillator cells outwards to reduce their radiation-related ageing and their material budget contributing to secondary particle production.

The FV0 opted to use the 2-inch model of Fine-Mesh PMT R5924-70 made by Hamamatsu. A fine mesh PMT is especially suitable to operate in a magnetic field. According to the manufacturer's specifications [180] the average gain drops to 41% of the nominal gain of 10^7 if the PMT operates within a magnetic field of 0.5 T. Compared to other types of PMTs this is a very good result. It is worth noting that the default gain in FV0 will be only $5 \cdot 10^4$. At this gain the effect of the magnetic field will be more significant, reaching an estimated factor of 5 – 10. This is still fully compatible with FV0 needs.

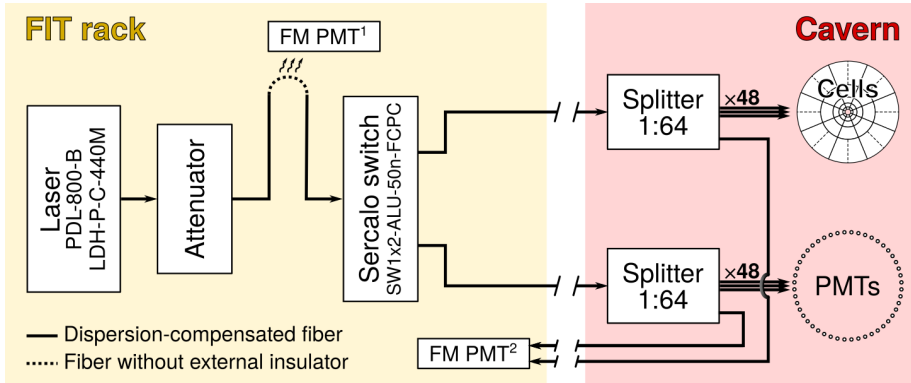


Figure 3.64.: Scheme of the possible FV0 laser calibration system

This particular model has also a relatively high average anode current allowing for wider dynamic range. This is especially important for large-area FV0, which expects to detect up to 700 MIPs in most loaded cells in central Pb–Pb collision. At the lower end of the dynamic range, it has to be capable of single-MIP detection. Such conditions are prevalent in pp runs. The characteristics of the R5921-70 are summarized in Figure 3.63.

Of no least importance is the fact that this type of photosensor has an optimal ratio of price per active area, while it remains on par with more expensive options in terms of performance figures important for FV0.

3.4.7. Laser calibration system

The FV0 will use similar laser calibration system to FT0, described in subsection 3.3.17. In the FV0 there are two possible paths for the laser pulses: (i) through a set of calibration fibres, that are directed to illuminate the central part of each scintillator cell; (ii) through the second set of calibration fibres, that illuminates the entrance window of each PMT directly. The black wires visible within the white fibre bundles on the right side of Figure 3.62 are laser calibration fibres. To select which calibration path is used, an additional optical switch (Sercalo SW1x2-ALU-50n-FCPC) is installed compared to the baseline design of FT0. The scheme of the system is presented in Figure 3.64.

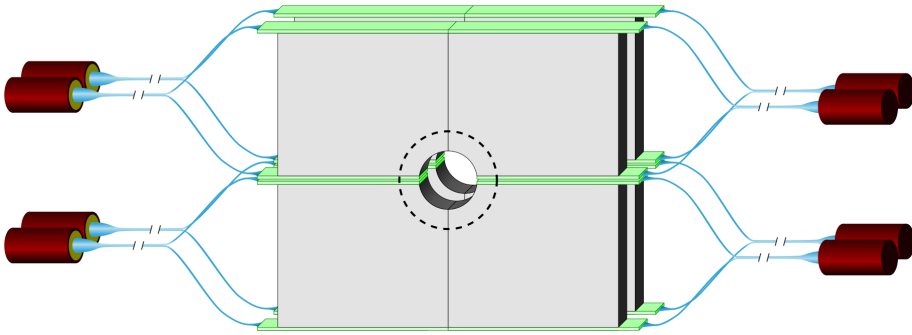


Figure 3.65.: The scheme of FDD-C. The outline of the FDD-A is shown with the dashed line. The only difference is the larger opening for the beam pipe

3.5. The Forward Diffractive Detector (FDD)

In 2019 the ALICE collaboration decided to add the Forward Diffractive Detector (FDD) as the third component of FIT. The physics goals of FDD are similar to those of Run 2 AD. The FDD will study diffractive events, especially their cross sections [140, 141]. This goal is accomplished by using the FDD to tag photon-induced or diffractive processes by monitoring the absence of activity in the forward direction. Enlarging the pseudorapidity coverage of ALICE is crucial for that. The implementation of FDD will allow us to study diffraction at higher collision energies of 14 TeV, available only after the LS2. It will extend our understanding of diffraction and the initial state of protons and lead ions as a function of energy. Moreover, the FDD will participate in the multiplicity and centrality estimation, complementing the other FIT detectors and the Zero-Degree Calorimeter (ZDC). Its contribution is important especially on the C-side, where FV0 is missing. It will also serve as auxiliary luminometer and beam quality monitor by tagging the beam-gas interactions.

3.5.1. General detector layout

The FDD has two arrays, each consisting of two layers of plastic scintillator, divided into 4 radial sectors. The FDD arrays are located at very high rapidity regions (Figure 3.6, Table 3.3), at the distances of 17 and 19.5 meters from the

IP for the A- and C-side respectively. In total the FDD will have 16 active cells, each read by individual readout channel capable of measuring charge and time.

As shown in Figure 3.65, the 8 scintillator cells arranged in 2 layers are connected through wavelength shifting bars (green blocks) and optical fibres (light blue bundles) to photosensors (brown tubes). In the figure the detector is shown as rotated by 90°; in reality, the set of 4 photosensors will be placed at the floor, below the detector, and the other 4 will be hanged at the ceiling of the cavern. The distance between the detector and sensors is not up to scale. On the A-side, the PMTs will be placed below and above through 1 and 0.57 meter long fibres respectively. On the C-side the detector array will be placed inside the LHC tunnel, however, the sensors will be located inside ALICE cavern. Therefore, 3 meter long fibres will be used to transport the light from the scintillators inside the tunnel to the PMTs placed in the cavern.

The FDD is the upgraded version of the AD detector used in ALICE before LS2. The main changes are:

- improvement in readout speed, which will make the FDD compatible with Run 3 conditions;
- upgrade to a faster plastic scintillator;
- upgrade to a faster state-of-art wavelength shifter; thanks to it the light decay time decreased from 8.5 to 1 ns;
- improved detector case to avoid contamination from outside light.

Altogether, these improvements make FDD operable after LS2 by shortening the length of light pulses to less than 25 ns, which is the shortest bunch spacing foreseen for pp runs. Also, the time resolution is improved.

3.5.2. Plastic scintillator and light collection system

Because particle detection in the FDD relies on scintillation effect, its operation is similar to that of FV0. Each arm of FDD uses two adjacent scintillator layers compared to a single layer used by the FV0. The discrimination of single-MIP signal for a single layer does not have to be as clear as in FV0, because a coincidence between layers can be required, thus reducing the background considerably. Thanks to relaxing of the noise immunity requirement, the scintillator layers of FDD can be thinner.

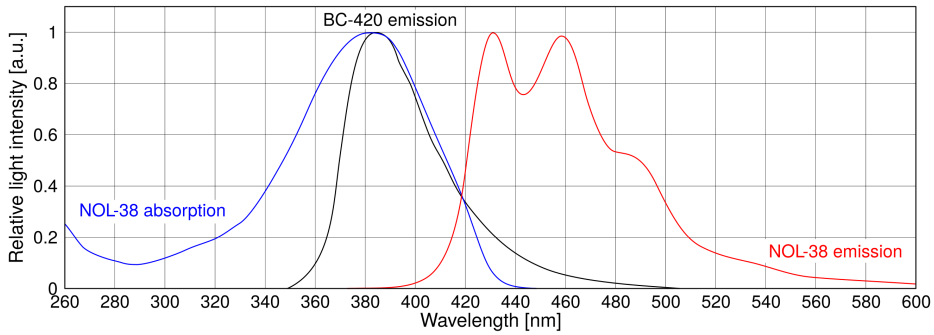


Figure 3.66.: Emission spectrum of the BC-420 scintillator (*black line*), based on figure published by the manufacturer [179]. Emission (*red*) and absorption (*blue*) spectrum of NOL-38 wavelength shifter are also shown

A single MIP deposits approximately 5 MeV of energy while crossing the 2.5 cm thickness of a single scintillator layer in the FDD. The scintillation photons propagate within the scintillator cell until some of them reach the wavelength shifting (WLS) bars attached to two narrow sides of the cell. They may be absorbed there, exciting molecules of the wavelength shifter, that shortly deexcite emitting photons of longer wavelength. The wavelengths of some of the photons emitted by the wavelength shifter overlap with its absorption spectra. Such photons can be absorbed by the wavelength shifter itself and reemitted. This mechanism can extend the tail of the signal by introducing late photons. The photons emitted by the WLS bars propagate along them until they reach the entrance to the bundle of optical fibres attached to end caps of the bars. The fibres are of Clear-PS type, made by Kuraray [181]. They are non-scintillating and non-wavelength shifting. The bundles of fibres from two WLS bars of a single cell transport light towards a remote photosensor. The scheme of FDD-A, including all of its functional elements is shown in Figure 3.65.

The FDD uses BC-420 plastic scintillator, the characteristics of which are listed in Table 3.8. The BC-420 is slightly faster than the EJ-204, used by FV0, at the expense of shorter attenuation length and shorter emission wavelengths. The shorter attenuation length does not significantly affect the total number of photons reaching the bars because of the compact size of the FDD. On the other hand, the emitted photons enter the near-ultraviolet regime, which increases the

losses during light transport and detection in most common materials. To offset this shortcoming WLS bars BC-499-90, that use the wavelength shifter NOL-38, are introduced to convert close-UV light into blue light. The Figure 3.66 shows the emission spectrum of the BC-420 scintillator and the absorption and emission spectra of the NOL-38 wavelength shifter. The range of wavelengths absorbed by NOL-38 completely covers the emission range of BC-420 scintillator. Thanks to that the wavelength conversion efficiency is optimized.

Such a design is simpler than the light collection system of FV0, at the cost of slightly worse time resolution and longer signal tail. In the FDD there are two consecutive absorptions and emissions, one in the scintillator and the other one in the WLS bar, each with a characteristic time constant, that smears the timing signals. The timing properties of BC-420 scintillator are listed in Table 3.8, while the decay time of the NOL-38 is relatively short, at 0.95 ns. On the other hand, this design is compact enough to allow for more closely detection layers. It is also less expensive and less laborious to build.

3.5.3. Photosensor

The FDD uses Hamamatsu PMT assembly H8409-70, that incorporates FM-PMT R7761-70. This PMT belongs to the same family of Fine-Mesh PMTs as FV0's R5924-70, but it has 1.5' photocathode instead of 2'. The corresponding active area of the photosensor is sufficient for the size of the fibre bundle, that, on the other end, needs to cover only the small-area face of the wavelength-shifting bar. The PMT selected for FDD is, therefore, less expensive than the FV0 model. Other characteristics, presented in Figure 3.63, remain the same as for FV0 PMT.

The photosensors are at some distance from the active scintillator cells, as shown in Figure 3.65. All dimensions in this figure are proportional, except the length of optical fibres, which in reality are much longer, at 2.5 m on the C-side and 1 (0.57) m on the bottom (top) of A-side. This separation is needed due to the following items.

- Very high radiation dose expected at high pseudorapidities, that would deteriorate performance by accelerating ageing of the photosensor.
- High flux of charged particles, that would contribute to background signals detected in the PMTs by hitting the sensors directly. The effect is mainly caused by the secondary particles and it generates early component of the signal. To mitigate the similar issue in Run 2 the AD detector installed

shielding blocks in front of the photocathodes of the sensors on the A-side. A similar approach is considered for FDD.

- Different location of the C-side detector and sensors required by safety regulations. The FDD-C detector is located in the LHC tunnel, where it is not allowed to place active components. The sensors had to be placed in the ALICE cavern and the fibres had to be routed through a hole that separates the cavern and the tunnel.

The plateau of highest quantum efficiency of the selected PMT matches well with the emission spectrum of NOL-38 wavelength shifter, except perhaps the third, smaller emission peak at wavelengths longer than 480 nm. At this wavelength, the quantum efficiency already starts dropping below 20%, but the vast majority of light is produced within the larger two peaks, so the losses compared to shorter wavelengths are not significant.

3.5.4. Laser calibration system

The FDD is expected to apply similar laser calibration methods as the FV0 (subsection 3.4.7). One significant difference will be that FDD will use shorter wavelengths of 405 nm, so the models of optical components will have to be adjusted to cope with that, but the general scheme will remain similar. The finer details of the system are not fixed at the time of writing of this manuscript.

3.6. Detector performance

FIT is expected to perform at least as well as its predecessors. The following performance simulations have been done to test if the proposed design fulfils the requirements (see Section 3.1):

- Centrality resolution
- Event plane resolution
- QED background study
- Trigger efficiency

After an introduction to the used software tools, the following subsections focus on the first three studies from this list.

3.6.1. Simulation environment

For the early upgrade performance studies the AliRoot environment, normally used for data analysis and simulation in Run 1 and Run 2, was adapted to Run 3 conditions. The AliRoot is a software package developed by ALICE Collaboration, which is based on the ROOT [182] analysis package created and maintained by CERN. The AliRoot [147, 148] includes the ALICE detector geometry description and interfaces with various particle collision generators (PYTHIA [144], HIJING [183, 184], DPMJET [185], etc.) and GEANT3 [186] particle transport code.

Ultimately for Run 3, the new O² [187, 188] software package is being developed, but its maturity was insufficient at the time most of these studies were performed. Therefore, the results presented in this chapter were obtained using AliRoot unless otherwise noted.

3.6.2. Centrality resolution

Centrality describes the geometry of a nuclear collision [175], which affects the energy density within the collision region available for particle production. During a collision, an overlap region is formed by two colliding nuclei. Its shape and size is determined by the impact parameter (\vec{b}) and by the local fluctuations

of positions of nucleons within nuclei. The other collision parameters include the number of nucleons participating in a collision (N_{part}) and the number of binary collisions (N_{coll}). All of them are described by the Glauber model [114].

Accurate determination of centrality is important for two reasons. Firstly, the dependence of various observables on centrality can be used to constrain theoretical models. Secondly, the centrality is a good estimator for the actual amount of energy that was used for particle production and did not escape with the remaining momentum of colliding nuclei. This allows for comparison of experimental results, between collision systems of different particle species and energies.

Centrality determination is often one of the main tasks of forward detectors in a heavy-ion experiment. Usually, precise central-rapidity tracking detectors are used to measure various observables as a function of centrality. To avoid self-bias a different set of forward detectors looks at the different subset of the produced particles to measure the centrality. Therefore, the resolution of centrality is the key parameter describing the performance of a forward detector. Before the Run 3 ALICE used the charged particle multiplicity (N_{ch}) in different detectors (V0, SPD, TPC) and energy deposited in the Zero Degree Calorimeter to reconstruct centrality [175]. In Run 3 this will remain the same with the V0 being replaced by FIT and SPD – by the new ITS.

Experimentally, centrality is reconstructed by collecting a sample of events and ordering them by the observable, which correlates well with the centrality. The chosen observable is assumed to change monotonically as a function of centrality. All events are then grouped into centrality classes according to their order. In this study the centrality resolution is defined as the width of the distribution of differences between the *true* centrality and centrality measured by a detector. Unfortunately, the *true* centrality can be measured neither in simulation nor in experiment. It can only be estimated with some uncertainty. In the simulation aiming to study the centrality resolution of the FIT the total number of primary particles produced during the collision was used as the estimator for the *true* centrality. The correlation graphs of the centralities calculated using three selected observables with reference centrality are shown in Figure 3.67. The left plot of Figure 3.67 represents the realistic performance of the combination of the FV0 and both FT0 arrays. For comparison, the middle plot in Figure 3.67 shows centrality calculated based on the number of primary particles vs. the total number of particles. The total number of particles is a sum of primaries and secondaries, so auto-correlation is expected in this plot. As the separation to primaries and secondaries is only available in simulations, this plot represents

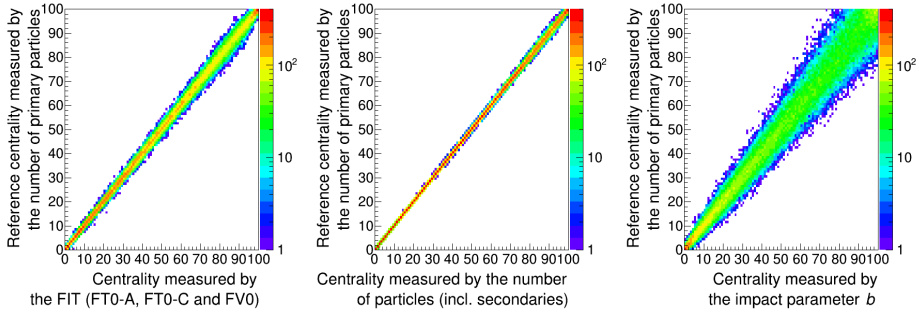


Figure 3.67.: Correlation of centralities reconstructed using different observables

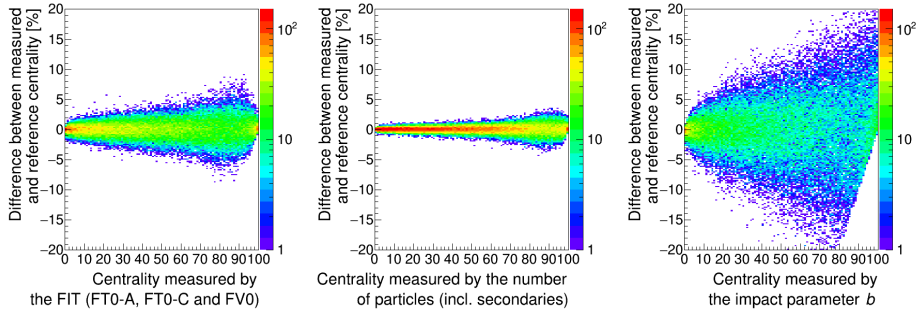


Figure 3.68.: Difference between centralities reconstructed using three different observables

the best experimentally achievable performance, that could only be reached by a hypothetical 4π detector, capable of detecting all particle species with 100% efficiency. The right plot in Figure 3.67 presents the correlation between the centralities calculated based on the impact parameter and the number of primaries. While the correlation is still clear, its resolution is worse. This is because the impact parameter and the number of particles are independent observables, as opposed to the cases shown in the other plots in this figure, where one observable is a subset or derivative of the other. Additionally, the fluctuations in nucleons positions and momenta influence the multiplicity, but information about them is not carried by the single number of impact parameter.

The Figure 3.68 shows differences between centralities reconstructed using one

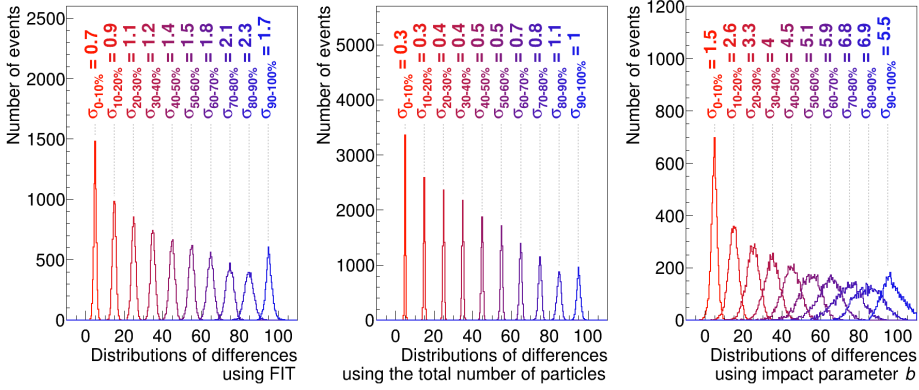


Figure 3.69.: Difference between centralities reconstructed using various observables when grouped into 10% wide centrality classes. Each distribution is shifted so that its mean value matches the middle of the corresponding centrality class

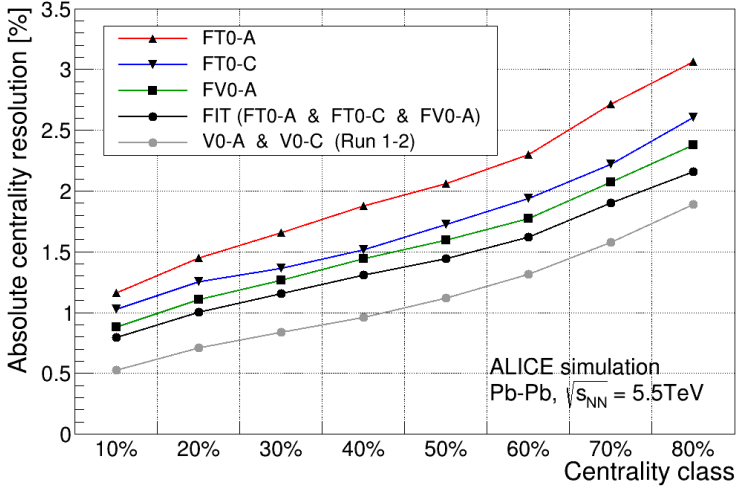


Figure 3.70.: Centrality resolution of the FIT components

of three observables (number of particles detected by FIT, the total number of particles and impact parameter) and the reference centrality. The layout of the plots follows that of Figure 3.67. For centralities other than the extremes the distribution of differences is Gaussian, but for the extreme centralities, the shape becomes asymmetric because of the edge-effect. The difference of two values, neither of which can exceed 100% or drop below 0% is less likely to be close to these extremes. The asymmetry is clear also in Figure 3.69 which presents the same data as Figure 3.68, but with events grouped into 10%-wide centrality classes and the resolutions calculated for each class. The trend of resolution deterioration with increasing centrality can be mainly attributed to the decreasing number of produced particles and the statistical fluctuations.

The centrality resolution of different components of FIT is shown in Figure 3.70. The FV0 performs better than each of the FT0 arrays. When data from FV0 and FT0 are combined, there is a further performance improvement. The centralities above 80% are not shown, because the beam-gas and QED backgrounds were not simulated. In the experiment, these backgrounds contaminate the classes of low-multiplicity events and they are hard to distinguish from very peripheral hadronic events. The performance of V0A and V0C from Run 1 and 2 is also shown for reference [175]. It is better by about 30%. This is because in Run 3 the C-side has reduced area compared to Run 2.

3.6.3. Event plane resolution

The event plane resolution is introduced in subsection 2.4.4 and defined in Equation 2.17. The FT0 focuses on clean online trigger, vertex position and luminosity determination, so the timing and spatial constraints, availability of suitable sensor on the market and its size were the major factors defining its granularity. For the FV0, the major factors that needed balancing were price per channel vs. performance. The main FV0 performance figures are the centrality and event plane resolution. As is shown in subsection 3.6.2, the granularity is irrelevant for the estimation of centrality as long as the total number of detected particles is correctly reconstructed by the FV0. Quite the opposite is the case for the event plane resolution because its reconstruction requires information on the azimuth angle of the detected particles. In reality the flow coefficients also weakly depend on rapidity (see Figure 25 in [189]) and on p_T [190–192]. However, in this study, they are considered second-order effects and are not taken into account.

A set of toy Monte Carlo (ToyMC) simulations was performed to gauge how the

event plane resolution changes with the number of sectors of FV0. The ToyMC is divided into two stages: simulation and reconstruction. The simulation stage uses two inputs:

- The plot showing charged particle density distribution as a function of pseudorapidity [193, 194] is used to extract the total number of charged particles passing through the pseudorapidity of FV0.
- Experimentally measured flow coefficients [192, 195] are used to simulate the azimuth angle of each particle.

The p_T , pseudorapidity and type of particle is not simulated. The reconstruction stage transports the simulated particles through a detector with defined granularity and uses the reconstructed particle angles to calculate the flow vectors and \mathcal{R}_n (see subsection 2.4.4).

The effect of FV0 granularity on the event plane resolution is shown in Figure 3.71. The second harmonics (\mathcal{R}_2) and the subset of mid-central events (30–40%) was selected for this study. The \mathcal{R}_2 for the ideal detector, i.e., fully efficient and capable of perfect azimuth angle determination for each particle, is shown with the red dashed line and equals to 0.945. Following the Equation 2.17, the perfect \mathcal{R}_2 value would be 1. The maximum $\mathcal{R}_2 = 0.945$ corresponds to an average difference of 9.5° between the simulated-*true* and reconstructed reaction plane. The resolution of the reconstructed event plane is limited by the number of detected particles, i.e., by the event multiplicity and by the detector acceptance and efficiency.

For the FV0, the \mathcal{R}_2 saturates relatively quickly. Once the number of FV0 sectors reaches 8 the \mathcal{R}_2 is already within 1% of the maximum value. Therefore, the baseline FV0 design consists of 8 sectors (the same as in V0 before LS2).

As v_2 is generally larger than any other harmonics, especially for the mid-centralities, the \mathcal{R}_2 is also maximized. This makes it most sensitive to any changes. While the \mathcal{R}_2 can be considered a reasonable baseline for such a simplified approach, it is worth noting that the trend for higher harmonics ($\mathcal{R}_{n \geq 3}$) is expected to saturate at higher number of sectors.

3.6.4. QED background study

The QED background has been described in subsection 2.5.6. In FIT the QED background will affect both the purity of the MB trigger, especially for peripheral

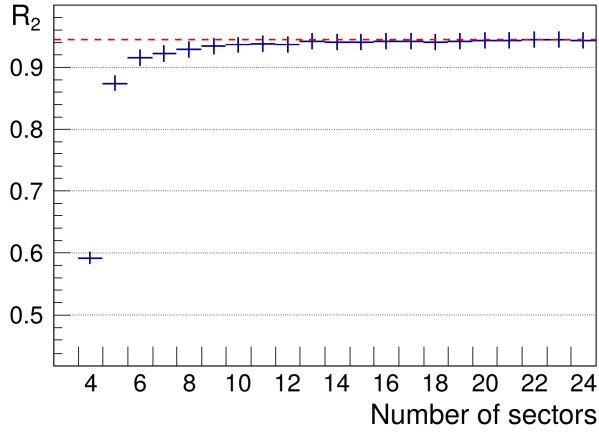


Figure 3.71.: Event plane resolution (\mathcal{R}_2) of FV0 as a function of the number of sectors

Table 3.11.: Assumptions used to evaluate the effect of QED background in FT0

Parameter	Unit	Value
LHC revolution frequency	kHz	11.2455
Pb–Pb hadronic interaction rate	kHz	50
Number of bunch crossings per revolution		576

events, and the data rate associated with QED-only triggers. It was important to verify how the detector would perform in high QED-background conditions, especially considering ALICE will operate at two magnetic field values during Run 3. The operation in the magnetic field reduces the visible QED cross section with respect to Equation 2.19, because low-energy or low- p_T electrons follow the spiral trajectories along the beam pipe. Many of them get trapped within the beam pipe until they exit the region of L3 magnet without interacting with our detectors.

The rate of QED-only triggers can be reduced by increasing the amplitude threshold. At the time of this study, the simulation framework was not yet mature.

The FV0 was not implemented and charge or amplitude reconstruction of FT0 was missing. Therefore, the number of Cherenkov photons reaching the photocathode of the photosensors was used as a proxy to amplitude. In the simulation, the threshold was set on the sum of Cherenkov photons from all detectors. The ADC noise was not simulated, so there is no need to subtract it for each channel. While the application of the threshold helps in reducing the QED-only triggers, it also lowers the efficiency for hadronic triggers, especially those corresponding to peripheral collisions. The range of studied thresholds is sufficient to eliminate QED-only triggers and, at the same time, it results in a negligible change in hadronic trigger efficiency for centralities $\leq 80\%$. On the other hand, ultraperipheral events with centrality 90–100% are characterized by small particle multiplicity and for them, the trigger efficiency drops rapidly due to limited acceptance and detector efficiency. Therefore, the peripheral class of Pb–Pb collisions with the centrality of 80–90% was selected for this study.

Two sets of simulations were performed for each magnetic field setting. The first one consisted of a combination of the hadronic and QED signals. The Hijing generator was used to simulate the Pb–Pb collisions [183] and the QED event generator [196] was applied on top of it. The obtained dataset represents the hadronic interaction contaminated with the QED background. Approximately 1200 minimum-bias events were simulated for each magnetic field setting. The second simulation set consisted of only the QED interactions. Around 500000 QED-only events were simulated for each magnetic field setting. The parameters, used to calculate the event and trigger rates based on these two sets of simulations, are shown in Table 3.11.

The simulated QED rates, detected by the FT0, are plotted for the two values of magnetic flux densities expected in ALICE (0.2 T and 0.5 T), together with the hadronic trigger efficiency, as a function of amplitude threshold in Figure 3.72. The shown uncertainties are only statistical. The uncertainty of rate is calculated as for the Gaussian distribution, i.e., \sqrt{n} and the uncertainty of efficiency ($\Delta\epsilon$) is calculated as for the binomial distribution:

$$\Delta\epsilon = \sqrt{T \left(1 - \frac{T}{N}\right)} \quad (3.7)$$

The T represents the number of detected triggers, N is the number of simulated events, where the efficiency is calculated as $\epsilon = \frac{T}{N}$.

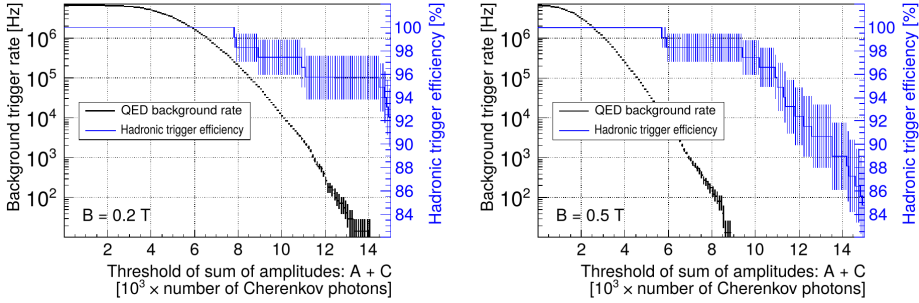


Figure 3.72.: Simulated trigger efficiency for peripheral hadronic events (centrality 80–90%) and rate of QED events as a function of threshold in FT0-A and FT0-C in two magnetic fields foreseen for ALICE: 0.2 T (left) and 0.5 T (right)

The plots show, that in the worse case of the lower magnetic field of 0.2 T it could be possible to tune the thresholds to achieve $\sim 100\%$ efficiency for centralities 80%-90% at the cost of QED trigger rates of the order of 300 kHz. This is only 6 times higher than the nominal Pb–Pb interaction rate and 3 times lower than the pp interaction rate in the extended running scenario (see subsection 3.3.13). Such a trigger rate is well within the capabilities of the readout, though some efforts will have to be considered to suppress this background before the data is permanently stored.

4. Summary and outlook

This thesis focused on the description of the R&D, design and functional tests of subcomponents of the ALICE Fast Interaction Trigger, especially these related to the FT0 subdetector. The scope ranged from single-component tests aimed to determine the response of the photosensors and optical properties of applied materials, through prototype assemblies, that proved the detector modules can deliver relevant data, ending with the selection of simulations of the detector performance.

Different tools and methods have been utilized for various tests. Whenever applicable the tabletop laboratory equipment was used as a substitute for the expensive and laborious beam tests. Nevertheless, the beam tests were performed after every major design iteration to verify the effect of modifications. The characterization of photosensors was done with a simplified version of the laser calibration system. This also helped to validate the idea behind this system. As for the performance simulations, each simulation was done at different point in time and so different framework versions were used. Usage of different framework versions is not expected to affect the results as the frameworks are continually tested and validated with every new version.

The results presented in this thesis show that the FIT design has been successfully optimized to reach its technical and physics goals within the existing constraints and expected operational regime. Additionally, the procedure for assembly, tests and characterization of the most crucial FT0 detector component, i.e., the MCP-PMT photosensor, is described. The individual characterization of all of the sensors allowed us to reject the units of inferior quality. It helped to reduce the risk of sensor failure after the installation of FIT.

The scope of the thesis does not provide exhaustive coverage of the subject of FIT. The significant topics of readout electronics, detector control system and their integration with ALICE central systems have been omitted. The FV0 and FDD subdetectors are also presented in a limited scope. The description of the laser calibration system is slightly simplified and it does not provide full information on all of the challenges, that we have encountered.

Nevertheless, this thesis can be considered a reasonable first step in understanding the composition, principles of operation and the expected performance of the FIT detector.

A. List of presentations and publications

Most relevant publications

Maciej Slupecki. Upgrade of ALICE forward detectors. *PoS*, ICHEP2018:255, 2019.

Maciej Slupecki. ALICE forward rapidity upgrades. *PoS*, EPS-HEP2017:519, 2017.

W. H. Trzaska [ALICE Collaboration]. New Fast Interaction Trigger for ALICE. *Nucl. Instrum. Meth. A* **845** (2017) 463.

D.A. Finogeev et al. Performance study of the fast timing Cherenkov detector based on a microchannel plate PMT. *J. Phys. Conf. Ser.*, 798(1):012168, 2017.

E. V. Antamanova et al. Anode current saturation of ALD-coated Planacon[®] MCP-PMTs. *JINST*, 13(09):T09001, 2018.

International conferences

- XIX JINR Annual Young Scientists and Specialists Conference (AYSS-2015)
Dubna, Russia, 2015.02.16–20
URL: <http://omus.jinr.ru/conference2015>
Talk: *Simulation of performance of the Fast Interaction Trigger in ALICE*
- Quark Matter QM-2015
Kobe, Japan, 2015.09.21–10.03
URL: <https://qm2015.riken.jp/>
Poster (co-authored): *Performance of the Fast Interaction Trigger for the ALICE upgrade*
- The XX International Scientific Conference of Young Scientists and Specialists (AYSS-2016)
Dubna, Russia, 2016.03.14–18

URL: <https://indico-new.jinr.ru/event/73/>

Best talk in session: *Challenges and progress in the design of the Fast Interaction Trigger*

- EPS Conference on High Energy Physics (HEP-EPS)
Venice, Italy, 2017.07.05–12
URL: <https://indico.cern.ch/event/466934/>
Talk and proceedings [73]: *ALICE forward rapidity upgrades*
- XXXIX International Conference on High Energy Physics (ICHEP 2018)
Seoul, Korea, 2018.07.04–11
URL: <http://www.ichep2018.org/>
Talk and proceedings [74]: *Upgrade of ALICE forward detectors*

National conferences

- Particle Physics Day 2014, Jyvaskyla, 2014.10.24
Talk: *Fast Interaction Trigger for ALICE*
- Physics Days 2015, Helsinki, 2015.03.17–19
Poster: *Performance studies of the new Fast Interaction Trigger in ALICE*
- Physics Days 2016, Oulu, 2016.03.29–31
URL: <https://www.fp2016.fi/>
Poster: *The new Fast Interaction Trigger for ALICE*
- Physics Days 2017, Helsinki, 2017.03.22–24
URL: <http://fp2017.physics.aalto.fi/>
Poster: *The Fast Interaction Trigger for ALICE*
- Particle Physics Day 2018, Jyvaskyla, 2018.11.23
URL: <http://users.jyu.fi/~tulappi/hitupva18.html>
Talk: *Upgrade of ALICE forward trigger detectors*
- Physics Days 2019, Helsinki, 2019.03.05–07
URL: <https://www.helsinki.fi/en/conferences/physics-days-fysiikan-paivat-2019>
Poster: *ALICE Upgrade for LHC Run 3 and Run 4*

Bibliography

- [1] J. Beringer et al. Review of Particle Physics (RPP). *Phys. Rev.*, D86:010001, 2012.
- [2] M. Aker et al. Improved Upper Limit on the Neutrino Mass from a Direct Kinematic Method by KATRIN. *Phys. Rev. Lett.*, 123(22):221802, 2019, 1909.06048.
- [3] Georges Aad et al. Observation of a new particle in the search for the Standard Model Higgs boson with the ATLAS detector at the LHC. *Phys. Lett.*, B716:1–29, 2012, 1207.7214.
- [4] Serguei Chatrchyan et al. Observation of a New Boson at a Mass of 125 GeV with the CMS Experiment at the LHC. *Phys. Lett.*, B716:30–61, 2012, 1207.7235.
- [5] Simon Hands. The Phase diagram of QCD. *Contemp. Phys.*, 42:209–225, 2001, physics/0105022.
- [6] Richard P. Feynman. Very high-energy collisions of hadrons. *Phys. Rev. Lett.*, 23:1415–1417, Dec 1969.
- [7] E. D. Bloom et al. High-Energy Inelastic $e - p$ Scattering at 6° and 10° . *Phys. Rev. Lett.*, 23:930–934, Oct 1969.
- [8] M. Breidenbach et al. Observed behavior of highly inelastic electron-proton scattering. *Phys. Rev. Lett.*, 23:935–939, Oct 1969.
- [9] Yu. M. Antipov et al. Search for the particles with fractional charges (quarks) at i h e p 70 gev accelerator. *Phys. Lett.*, 29B:245–248, 1969.
- [10] G. Gallinaro and G. Morpurgo. Preliminary Results in the Search for Fractionally Charged Particles by the Magnetic Levitation Electrometer. *Phys. Lett.*, 23:609–613, 1966.
- [11] R. P. Feynman. The behavior of hadron collisions at extreme energies. *Conf. Proc.*, C690905:237–258, 1969.
- [12] Bruno R. Stella and Hans-Jurgen Meyer. $Y(9.46 \text{ GeV})$ and the gluon discovery (a critical recollection of PLUTO results). *Eur. Phys. J.*, H36:203–243, 2011, 1008.1869.

-
- [13] D. P. Barber et al. Discovery of Three Jet Events and a Test of Quantum Chromodynamics at PETRA Energies. *Phys. Rev. Lett.*, 43:830, 1979.
- [14] David J. Griffiths. *INTRODUCTION TO ELEMENTARY PARTICLES. Feynman rules for Chromodynamics*, chapter 9.1, pages 279–284. NEW YORK, USA: WILEY (1987) 392p, 1987.
- [15] D. J. Gross. The discovery of asymptotic freedom and the emergence of QCD. *Proc. Nat. Acad. Sci.*, 102:9099–9108, 2005. [Int. J. Mod. Phys.A20,5717(2005); Rev. Mod. Phys.77,837(2005)].
- [16] O. W. Greenberg. Spin and unitary-spin independence in a paraquark model of baryons and mesons. *Phys. Rev. Lett.*, 13:598–602, Nov 1964.
- [17] M. Y. Han and Y. Nambu. Three-Triplet Model with Double SU(3) Symmetry. *Phys. Rev.*, 139:B1006–B1010, Aug 1965.
- [18] Christian S. Fischer and Richard Williams. Probing the gluon self-interaction in light mesons. *Phys. Rev. Lett.*, 103:122001, 2009, 0905.2291.
- [19] Kenneth G. Wilson. Confinement of Quarks. *Phys. Rev.*, D10:2445–2459, 1974. [,45(1974); ,319(1974)].
- [20] C. T. H. Davies et al. High precision lattice QCD confronts experiment. *Phys. Rev. Lett.*, 92:022001, 2004, hep-lat/0304004.
- [21] A. M. Green. Bridges from lattice qcd to nuclear physics. *Hadronic Physics from Lattice QCD*, page 249–367, Oct 2004.
- [22] J. C. Collins and M. J. Perry. Superdense matter: Neutrons or asymptotically free quarks? *Phys. Rev. Lett.*, 34:1353–1356, May 1975.
- [23] Edward V. Shuryak. Correlation functions in the QCD vacuum. *Rev. Mod. Phys.*, 65:1–46, 1993.
- [24] Dirk H. Rischke. The Quark gluon plasma in equilibrium. *Prog. Part. Nucl. Phys.*, 52:197–296, 2004, nucl-th/0305030.
- [25] John R. Ellis. From little bangs to the Big Bang. *J. Phys. Conf. Ser.*, 50:8–21, 2006, astro-ph/0504501.
- [26] A. Vilenkin. Creation of Universes from Nothing. *Phys. Lett.*, 117B:25–28, 1982.
- [27] J. Allday. *Quarks, leptons and the big bang*. Bristol, UK: IOP (1998) 315 p, 1998.
- [28] C. Knobel. An introduction into the theory of cosmological structure formation, 8 2012, 1208.5931.

-
- [29] Dominik J. Schwarz. The first second of the universe. *Annalen Phys.*, 12:220–270, 2003, astro-ph/0303574.
- [30] Yasuyuki Akiba et al. The hot qcd white paper: Exploring the phases of qcd at rhic and the lhc, 2 2015, 1502.02730.
- [31] Y. Aoki, Z. Fodor, S. D. Katz, and K. K. Szabo. The QCD transition temperature: Results with physical masses in the continuum limit. *Phys. Lett.*, B643:46–54, 2006, hep-lat/0609068.
- [32] John W. Harris and Berndt Muller. The Search for the quark - gluon plasma. *Ann. Rev. Nucl. Part. Sci.*, 46:71–107, 1996, hep-ph/9602235.
- [33] John Adams et al. Experimental and theoretical challenges in the search for the quark gluon plasma: The STAR Collaboration’s critical assessment of the evidence from RHIC collisions. *Nucl. Phys.*, A757:102–183, 2005, nucl-ex/0501009.
- [34] Ulrich Heinz and Raimond Snellings. Collective flow and viscosity in relativistic heavy-ion collisions. *Ann. Rev. Nucl. Part. Sci.*, 63:123–151, 2013, 1301.2826.
- [35] Sourendu Gupta. A short introduction to heavy-ion physics. In *Proceedings, 2nd Asia-Europe-Pacific School of High-Energy Physics (AEP SHEP 2014): Puri, India, November 04–17, 2014*, pages 219–238, 2017, 1508.01136.
- [36] M. M. Aggarwal et al. An experimental exploration of the qcd phase diagram: The search for the critical point and the onset of de-confinement, 7 2010, 1007.2613.
- [37] Y. Aoki, G. Endrodi, Z. Fodor, S. D. Katz, and K. K. Szabo. The Order of the quantum chromodynamics transition predicted by the standard model of particle physics. *Nature*, 443:675–678, 2006, hep-lat/0611014.
- [38] Andras Laszlo et al. Na61/Shine at the CERN SPS. *PoS*, CPOD07:054, 2007, 0709.1867.
- [39] T. Abyazimov et al. Challenges in QCD matter physics –The scientific programme of the Compressed Baryonic Matter experiment at FAIR. *Eur. Phys. J.*, A53(3):60, 2017, 1607.01487.
- [40] Kh. U. Abraamyan et al. The MPD detector at the NICA heavy-ion collider at JINR. *Nucl. Instrum. Meth.*, A628:99–102, 2011.
- [41] Mark G. Alford, Andreas Schmitt, Krishna Rajagopal, and Thomas Schäfer. Color superconductivity in dense quark matter. *Rev. Mod. Phys.*, 80:1455–1515, 2008, 0709.4635.
- [42] Elias R. Most, L. Jens Papenfort, Veronica Dexheimer, Matthias Hanauske,

- Stefan Schramm, Horst Stöcker, and Luciano Rezzolla. Signatures of quark-hadron phase transitions in general-relativistic neutron-star mergers. *Phys. Rev. Lett.*, 122(6):061101, 2019, 1807.03684.
- [43] E. Annala, T. Gorda, A. Kurkela, and A. Vuorinen. Gravitational-wave constraints on the neutron-star-matter Equation of State. *Phys. Rev. Lett.*, 120(17):172703, 2018, 1711.02644.
- [44] B. P. Abbott et al. Observation of Gravitational Waves from a Binary Black Hole Merger. *Phys. Rev. Lett.*, 116(6):061102, 2016, 1602.03837.
- [45] J. Adam et al. Measurement of transverse energy at midrapidity in Pb-Pb collisions at $\sqrt{s_{NN}} = 2.76$ TeV. *Phys. Rev.*, C94(3):034903, 2016, 1603.04775.
- [46] Peter Koch, Berndt Müller, and Johann Rafelski. From strangeness enhancement to quark-gluon plasma discovery. *Int. J. Mod. Phys. A*, 32(31):1730024, 2017, 1708.08115.
- [47] P. Huovinen, P. F. Kolb, Ulrich W. Heinz, P. V. Ruuskanen, and S. A. Voloshin. Radial and elliptic flow at RHIC: Further predictions. *Phys. Lett.*, B503:58–64, 2001, hep-ph/0101136.
- [48] Laszlo P. Csernai, Joseph. I. Kapusta, and Larry D. McLerran. On the Strongly-Interacting Low-Viscosity Matter Created in Relativistic Nuclear Collisions. *Phys. Rev. Lett.*, 97:152303, 2006, nucl-th/0604032.
- [49] Chun Shen. Studying QGP with flow: A theory overview. In *28th International Conference on Ultrarelativistic Nucleus-Nucleus Collisions (Quark Matter 2019) Wuhan, China, November 4-9, 2019*, 2020, 2001.11858.
- [50] Katarína Křížková Gajdošová. Collectivity in small and large collision systems at the LHC with ALICE. *J. Phys. Conf. Ser.*, 1271(1):012002, 2019.
- [51] Miklos Gyulassy and Michael Plumer. Jet quenching as a probe of dense matter. *Nucl. Phys.*, A527:641–644, 1991.
- [52] Xin-Nian Wang and Miklos Gyulassy. Gluon shadowing and jet quenching in A + A collisions at $s^{*}(1/2) = 200$ -GeV. *Phys. Rev. Lett.*, 68:1480–1483, 1992.
- [53] J. Adam et al. Measurement of jet suppression in central Pb-Pb collisions at $\sqrt{s_{NN}} = 2.76$ TeV. *Phys. Lett.*, B746:1–14, 2015, 1502.01689.
- [54] P. Koch, Berndt Muller, and Johann Rafelski. Strangeness in Relativistic Heavy Ion Collisions. *Phys. Rept.*, 142:167–262, 1986.
- [55] B. Abelev et al. Multi-strange baryon production at mid-rapidity in Pb-Pb collisions at $\sqrt{s_{NN}} = 2.76$ TeV. *Phys. Lett.*, B728:216–227, 2014, 1307.5543. [Erratum: *Phys. Lett.*B734,409(2014)].

-
- [56] B. I. Abelev et al. Enhanced strange baryon production in Au + Au collisions compared to p + p at $\sqrt{s(NN)} = 200$ -GeV. *Phys. Rev.*, C77:044908, 2008, 0705.2511.
- [57] Charles Gale and Kevin L. Haglin. Electromagnetic radiation from relativistic nuclear collisions, 6 2003, hep-ph/0306098.
- [58] Chun Shen, Ulrich W. Heinz, Jean-Francois Paquet, and Charles Gale. Thermal photons as a quark-gluon plasma thermometer reexamined. *Phys. Rev.*, C89(4):044910, 2014, 1308.2440.
- [59] Wit Busza, Krishna Rajagopal, and Wilke van der Schee. Heavy Ion Collisions: The Big Picture, and the Big Questions. *Ann. Rev. Nucl. Part. Sci.*, 68:339–376, 2018, 1802.04801.
- [60] B. Abelev et al. Upgrade of the ALICE Experiment: Letter Of Intent. *J. Phys.*, G41:087001, 2014.
- [61] C. Zhang. FoCal – A high granularity electromagnetic calorimeter for forward direct photon measurements. *Nucl. Instrum. Meth.*, A845:542–547, 2017.
- [62] T. Peitzmann. Prototype studies for a forward EM calorimeter in ALICE. In *Proceedings, International Conference on Calorimetry for the High Energy Frontier (CHEF 2013): Paris, France, April 22-25, 2013*, pages 341–347, 2013, 1308.2585.
- [63] W. H. Trzaska. personal communication.
- [64] K. Aamodt et al. The ALICE experiment at the CERN LHC. *JINST*, 3:S08002, 2008.
- [65] J. Allen et al. ALICE DCal: An Addendum to the EMCal Technical Design Report Di-Jet and Hadron-Jet correlation measurements in ALICE. Technical Report CERN-LHCC-2010-011. ALICE-TDR-14-add-1, CERN, Jun 2010.
- [66] D. Blau. Performance of the ALICE electromagnetic calorimeters in LHC Runs 1 and 2 and upgrade projects. In *3rd Conference on Calorimetry for the High Energy Frontier (CHEF 2019) Fukuoka, Japan, November 25-29, 2019*, 2020, 2001.02928.
- [67] K. Oyama. The transition radiation detector for ALICE at the LHC. *Nucl. Instrum. Meth.*, A623:362–364, 2010.
- [68] A. Velure. Upgrades of the ALICE TPC front-end electronics for LS1 and LS2. *IEEE Trans. Nucl. Sci.*, 62(3):1040–1044, 2015.
- [69] L. Betev, A. Gheata, M. Gheata, C. Grigoras, and P. Hristov. Performance

- optimisations for distributed analysis in ALICE. *J. Phys. Conf. Ser.*, 523:012014, 2014.
- [70] P. Antonioli, A. Kluge, and W. Riegler. Upgrade of the ALICE Readout & Trigger System. Technical Report CERN-LHCC-2013-019. ALICE-TDR-015, CERN, Sep 2013.
- [71] mcpCharacterization. <https://github.com/mslupeck/mcpCharacterization>. Accessed: 2020-04-10.
- [72] plotCaenGeckoLogs. <https://github.com/mslupeck/plotCaenGeckoLogs>. Accessed: 2020-04-10.
- [73] Maciej Slupecki. ALICE forward rapidity upgrades. *PoS*, EPS-HEP2017:519, 2017.
- [74] Maciej Slupecki. Upgrade of ALICE forward detectors. *PoS*, ICHEP2018:255, 2019.
- [75] CERN Geographic Information System - Map CERN. <https://maps.cern.ch>. Accessed: 2019-09-16.
- [76] Facts and figures about LHC. <https://home.cern/resources/faqs/facts-and-figures-about-lhc>. Accessed: 2019-09-16.
- [77] R. Harrison, F. Bernard, P. Dahlen, J. Mariethoz, B. Puccio, R. Schmidt, and M. Zerlauth. Powering interlock systems at CERN with industrial controllers. *Conf. Proc.*, C051010:PO2.036–3, 10 2005.
- [78] O. S. Brüning, P. Collier, P. Lebrun, S. Myers, R. Ostojic, J. Poole, and P. Proudlock. *LHC Design Report*. CERN Yellow Reports: Monographs. CERN, Geneva, 2004.
- [79] John Poole. Beam requirements and fundamental choices. In *LHC Design Report*, CERN Yellow Reports: Monographs, chapter 2 v4. CERN, Geneva, 2004.
- [80] Reyes Alemany, Mike Lamont, and Stephen Page. Functional specification: Lhc modes. Technical Report LHC-OP-ES-0005 rev 1.0, CERN, 11 2007.
- [81] Taking a closer look at LHC. https://www.lhc-closer.es/taking_a_closer_look_at_lhc/0.lhc_running. Accessed: 2019-09-14.
- [82] Longer term LHC schedule. <https://lhc-commissioning.web.cern.ch/lhc-commissioning/schedule/LHC-long-term.htm>. Accessed: 2019-09-17.

- [83] Roberto Losito. The Large Hadron Collider: status and plans. LHCP 2017. https://indico.cern.ch/event/517784/contributions/2482089/attachments/1459194/2253397/LHC_Status_and_Plans.-.LHCP_2017.pdf, 2017.
- [84] Accelerator performance and statistics — LHC. <http://acc-stats.web.cern.ch/acc-stats/#lhc/overview-panel>. Accessed: 2019-09-14.
- [85] Elena Shaposhnikova et al. LHC Injectors Upgrade (LIU) Project at CERN. In *Proceedings, 7th International Particle Accelerator Conference (IPAC 2016): Busan, Korea, May 8-13, 2016*, page MOPOY059, 2016.
- [86] Francesco Noferini. ALICE Highlights. *MDPI Proc.*, 13(1):6, 2019, 1906.02460.
- [87] K. Aamodt et al. Two-pion Bose-Einstein correlations in central Pb-Pb collisions at $\sqrt{s_{NN}} = 2.76$ TeV. *Phys. Lett.*, B696:328–337, 2011, 1012.4035.
- [88] B. Abelev et al. Centrality dependence of π , K, p production in Pb-Pb collisions at $\sqrt{s_{NN}} = 2.76$ TeV. *Phys. Rev.*, C88:044910, 2013, 1303.0737.
- [89] B. Abelev et al. K_S^0 and Λ production in Pb-Pb collisions at $\sqrt{s_{NN}} = 2.76$ TeV. *Phys. Rev. Lett.*, 111:222301, 2013, 1307.5530.
- [90] Jaroslav Adam et al. Enhanced production of multi-strange hadrons in high-multiplicity proton-proton collisions. *Nature Phys.*, 13:535–539, 2017, 1606.07424.
- [91] S. Acharya et al. Anisotropic flow of identified particles in Pb-Pb collisions at $\sqrt{s_{NN}} = 5.02$ TeV. *JHEP*, 09:006, 2018, 1805.04390.
- [92] Jonah E. Bernhard, J. Scott Moreland, and Steffen A. Bass. Bayesian estimation of the specific shear and bulk viscosity of quark-gluon plasma. *Nature Phys.*, 15(11):1113–1117, 2019.
- [93] Jonah E. Bernhard. *Bayesian parameter estimation for relativistic heavy-ion collisions*. PhD thesis, Duke U., 2018-04-19, 1804.06469.
- [94] Miklos Gyulassy and Michael Plumer. Jet Quenching in Dense Matter. *Phys. Lett.*, B243:432–438, 1990.
- [95] B. Abelev et al. Transverse momentum distribution and nuclear modification factor of charged particles in p-Pb collisions at $\sqrt{s_{NN}} = 5.02$ TeV. *Phys. Rev. Lett.*, 110(8):082302, 2013, 1210.4520.
- [96] S. Acharya et al. Transverse momentum spectra and nuclear modification factors of charged particles in Xe-Xe collisions at $\sqrt{s_{NN}} = 5.44$ TeV. *Phys. Lett.*, B788:166–179, 2019, 1805.04399.

-
- [97] S. Acharya et al. Measurement of D^0 , D^+ , D^{*+} and D_s^+ production in Pb-Pb collisions at $\sqrt{s_{NN}} = 5.02$ TeV. *JHEP*, 10:174, 2018, 1804.09083.
- [98] Grazia Luparello. Measurement of D-meson production in p-Pb collisions with the ALICE detector. *J. Phys. Conf. Ser.*, 509:012101, 2014, 1310.1714.
- [99] S. Acharya et al. Production of ${}^4\text{He}$ and ${}^4\overline{\text{He}}$ in Pb-Pb collisions at $\sqrt{s_{NN}} = 2.76$ TeV at the LHC. *Nucl. Phys.*, A971:1–20, 2018, 1710.07531.
- [100] J. Adam et al. Production of light nuclei and anti-nuclei in pp and Pb-Pb collisions at energies available at the CERN Large Hadron Collider. *Phys. Rev.*, C93(2):024917, 2016, 1506.08951.
- [101] Wladyslaw Henryk Trzaska. New ALICE detectors for Run 3 and 4 at the CERN LHC. *Nucl. Instrum. Meth.*, A958:162116, 2020.
- [102] B. Abelev et al. Technical Design Report for the Upgrade of the ALICE Inner Tracking System. Technical Report CERN-LHCC-2013-024. ALICE-TDR-017, CERN, Nov 2013.
- [103] Jaroslav Adam et al. Technical Design Report for the Muon Forward Tracker. Technical Report CERN-LHCC-2015-001. ALICE-TDR-018, CERN, Jan 2015.
- [104] B. Abelev et al. Upgrade of the ALICE Time Projection Chamber. Technical Report CERN-LHCC-2013-020. ALICE-TDR-016, CERN, Oct 2013.
- [105] T. L. Karavicheva, A. B. Kurepin, and W. H. Trzaska. Status of Fast Interaction Trigger for ALICE Upgrade. In *Proceedings, 30th International Workshop on High Energy Physics: Particle and Astroparticle Physics, Gravitation and Cosmology: Predictions, Observations and New Projects (IHEP 2014): Protvino, Russia, June 23-27, 2014*, pages 69–74, 2015.
- [106] Edmundo Garcia-Solis. The Fast Interaction Trigger Upgrade for ALICE. *PoS*, ICHEP2016:241, 2016.
- [107] Wladyslaw Henryk Trzaska. New Fast Interaction Trigger for ALICE. *Nucl. Instrum. Meth.*, A845:463–466, 2017.
- [108] T. L. Karavicheva. The Fast Interaction Trigger detector for the ALICE Upgrade. *J. Phys. Conf. Ser.*, 798(1):012186, 2017.
- [109] A. I. Maevskaya. Fast Interaction Trigger for the upgrade of the ALICE experiment at CERN: design and performance. *EPJ Web Conf.*, 204:11003, 2019, 1812.00594.
- [110] P. Buncic, M. Krzewicki, and P. Vande Vyvre. Technical Design Report for the Upgrade of the Online-Offline Computing System. Technical Report CERN-LHCC-2015-006. ALICE-TDR-019, CERN, Apr 2015.

-
- [111] W. Herr and B. Muratori. Concept of luminosity. In *CAS - CERN Accelerator School: Intermediate Course on Accelerator Physics*, 2006.
- [112] Michaela Schaumann. Heavy Ions in 2018. Evian Workshop, 2017.
- [113] M. Tanabashi et al. Review of particle physics. *Phys. Rev. D*, 98:030001, Aug 2018.
- [114] Michael L. Miller, Klaus Reygers, Stephen J. Sanders, and Peter Steinberg. Glauber modeling in high energy nuclear collisions. *Ann. Rev. Nucl. Part. Sci.*, 57:205–243, 2007, nucl-ex/0701025.
- [115] Sergei A. Voloshin, Arthur M. Poskanzer, and Raimond Snellings. Collective phenomena in non-central nuclear collisions. *Landolt-Bornstein*, 23:293–333, 2010, 0809.2949.
- [116] V. P. Konchakovski, V. D. Toneev, W. Cassing, E. L. Bratkovskaya, S. A. Voloshin, and V. Voronyuk. Collective properties of nucleus-nucleus collisions from AGS to LHC energies. *J. Phys. Conf. Ser.*, 389:012015, 2012, 1207.3272.
- [117] Hans P. Dembinski. LHCb: Recent results related to cosmic ray interactions. *EPJ Web Conf.*, 208:15005, 2019. [EPJ Web Conf.208,05003(2019)].
- [118] George Coombs, Massimiliano Ferro-Luzzi, and Rosen Matev. Beam-Gas Imaging Measurements at LHCb. In *Proceedings, 7th International Beam Instrumentation Conference (IBIC 2018): Shanghai, Cina, September 9-13, 2018*, page WEPB13, 2019.
- [119] Manuela Boscolo, Oscar Blanco-García, Helmut Burkhardt, Francesco Collamati, Roberto Kersevan, and Marian Lueckhof. Beam-gas Background Characterization in the FCC-ee IR. *J. Phys. Conf. Ser.*, 1067(2):022012, 2018.
- [120] K. Hencken, Yu. Kharlov, and S. Sadovsky. Ultraperipheral Trigger in ALICE. Technical Report ALICE-INT-2002-11, CERN, Nov 2002.
- [121] Adrian Alscher, Kai Hencken, Dirk Trautmann, and Gerhard Baur. Multiple electromagnetic electron positron pair production in relativistic heavy ion collisions. *Phys. Rev.*, A55:396–401, 1997, nucl-th/9606011.
- [122] K. Hencken, Yu. Kharlov, and S. Sadovsky. Ultraperipheral Trigger in ALICE. Technical report, CERN, 11 2002.
- [123] A. J. Baltz. The Physics of Ultraperipheral Collisions at the LHC. *Phys. Rept.*, 458:1–171, 2008, 0706.3356.
- [124] J. G. Contreras and J. D. Tapia Takaki. Ultra-peripheral heavy-ion collisions at the LHC. *Int. J. Mod. Phys. A*, 30:1542012, 2015.

- [125] F. Costa, A. Kluge, and P. Vande Vyvre. The detector read-out in ALICE during Run 3 and 4. *J. Phys. Conf. Ser.*, 898(3):032011, 2017.
- [126] D. Evans, A. Jusko, M. Krivda, L. Lietava, and L. A. Pérez Moreno. Trigger system. Design review. Technical report, CERN, Geneva, July 2017. Also available as <https://twiki.cern.ch/twiki/pub/ALICE/EngineeringDesignReview%28June2016%29/CTPLTU18.pdf>.
- [127] M. Krivda et al. The ALICE trigger system performance for p-p and Pb-Pb collisions. *JINST*, 7:C01057, 2012.
- [128] M. Krivda et al. The ALICE central trigger processor (CTP) upgrade. *Journal of Instrumentation*, 11(03):C03051–C03051, mar 2016.
- [129] M. Krivda et al. The ALICE trigger system for LHC Run 3. *PoS*, TWEPP-17:149, 2017, 1711.01200.
- [130] M. Krivda et al. ALICE trigger system for LHC Run 3. *PoS*, TWEPP2018:119, 2019.
- [131] ALICE trigger system for newcomers. <http://www.ep.ph.bham.ac.uk/twiki/bin/view/ALICE/AliceTriggerIntroduction>. Accessed: 2020-01-12.
- [132] A. Fernández et al. ACORDE a Cosmic Ray Detector for ALICE. *Nucl. Instrum. Meth.*, A572:102–103, 2007, physics/0606051.
- [133] A. Bhasin et al. Implementation of the ALICE Trigger System. In *Proceedings, 15th IEEE NPSS Real Time Conference 2007 (RT 07): Batavia, Illinois, April 29-May 4, 2007*, 2007.
- [134] M. Gallio, W. Klempt, L. Leistam, J. De Groot, and Jürgen Schükraft. *ALICE Zero-Degree Calorimeter (ZDC): Technical Design Report*. Technical Design Report ALICE. CERN, Geneva, 1999.
- [135] B. Abelev et al. Measurement of visible cross sections in proton-lead collisions at $\sqrt{s_{NN}} = 5.02$ TeV in van der Meer scans with the ALICE detector. *JINST*, 9(11):P11003, 2014, 1405.1849.
- [136] J. Adam et al. ALICE luminosity determination for pp collisions at $\sqrt{s} = 13$ TeV. Technical report, CERN, Jun 2016.
- [137] S. van der Meer. Calibration of the effective beam height in the ISR. Technical Report CERN-ISR-PO-68-31. ISR-PO-68-31, CERN, Geneva, 1968.
- [138] Vladislav Balagura. Notes on van der Meer Scan for Absolute Luminosity Measurement. *Nucl. Instrum. Meth.*, A654:634–638, 2011, 1103.1129.

- [139] B. Abelev et al. Measurement of inelastic, single- and double-diffraction cross sections in proton–proton collisions at the LHC with ALICE. *Eur. Phys. J., C*73(6):2456, 2013, 1208.4968.
- [140] Sergey Evdokimov. Diffraction physics with ALICE at the LHC. In *Proceedings, 30th International Workshop on High Energy Physics: Particle and Astroparticle Physics, Gravitation and Cosmology: Predictions, Observations and New Projects (IHEP 2014): Protvino, Russia, June 23-27, 2014*, pages 83–90, 2015, 1412.7300.
- [141] Abraham Villatoro Tello. AD, the ALICE diffractive detector. *AIP Conf. Proc.*, 1819(1):040020, 2017.
- [142] S. Acharya et al. Coherent J/ψ photoproduction at forward rapidity in ultra-peripheral Pb-Pb collisions at $\sqrt{s_{NN}} = 5.02$ TeV. *Phys. Lett.*, B798:134926, 2019, 1904.06272.
- [143] P. Betev, L. Chochula. Definition of the ALICE Coordinate System and Basic Rules for Sub-detector Components Numbering. Technical Report ALICE-INT-2003-038, CERN, Geneva, 2003.
- [144] Torbjorn Sjostrand, Stephen Mrenna, and Peter Z. Skands. PYTHIA 6.4 Physics and Manual. *JHEP*, 05:026, 2006, hep-ph/0603175.
- [145] Torbjorn Sjostrand, Stephen Mrenna, and Peter Z. Skands. A Brief Introduction to PYTHIA 8.1. *Comput. Phys. Commun.*, 178:852–867, 2008, 0710.3820.
- [146] S. Acharya et al. Radiation Dose and Fluence in ALICE after LS2. Technical report, CERN, Oct 2018.
- [147] R. Brun, P. Buncic, F. Carminati, A. Morsch, F. Rademakers, and K. Safarik. Computing in ALICE. *Nucl. Instrum. Meth.*, A502:339–346, 2003.
- [148] Federico Carminati and Andreas Morsch. Simulation in ALICE. *eConf*, C0303241:TUMT004, 2003, physics/0306092.
- [149] P. Cortese et al. ALICE technical design report on forward detectors: FMD, T0 and V0. Technical report, CERN, 2004.
- [150] J. Adam et al. Determination of the event collision time with the ALICE detector at the LHC. *Eur. Phys. J. Plus*, 132(2):99, 2017, 1610.03055.
- [151] A. Maevskaya. Start and trigger detector t0 of the ALICE experiment. *PoS, Baldin-ISHEPP-XXI*:110, 2012.
- [152] T. Malkiewicz et al. Luminosity determination in ALICE with T0 and V0 detectors. *Indian J. Phys.*, 85:965–970, 2011.

- [153] M. Bondila et al. ALICE T0 detector. *IEEE Trans. Nucl. Sci.*, 52:1705–1711, 2005.
- [154] Y. Zoccarato et al. Front end electronics and first results of the ALICE V0 detector. *Nucl. Instrum. Meth.*, A626-627:90–96, 2011.
- [155] B. Cheynis, L. Ducroux, J. Y. Grossiord, A. Guichard, P. Pillot, B. Rapp, R. Tieulent, W. Tremeur, and Y. Zoccarato. Radiation effects on ALICE V0 detector components. *Nucl. Instrum. Meth.*, A569:732–736, 2006.
- [156] C. H. Christensen, J. J. Gaardhoje, K. Gulbrandsen, B. S. Nielsen, and C. Sogaard. The ALICE Forward Multiplicity Detector. *Int. J. Mod. Phys.*, E16:2432–2437, 2007, 0712.1117.
- [157] Maxime Guilbaud. Pseudorapidity density of charged particles and its centrality dependence in Pb-Pb collisions at $\sqrt{s_{NN}}=2.76$ -TeV. *Nucl. Phys.*, A904-905:381c–384c, 2013.
- [158] Secondary Beams & Areas.
<http://sba.web.cern.ch/sba/BeamsAndAreas/East/East.htm>. Accessed: 2020-02-15.
- [159] E. V. Antamanova et al. Anode current saturation of ALD-coated Planacon® MCP-PMTs. *JINST*, 13(09):T09001, 2018, 1807.03804.
- [160] Yu. A. Melikyan. Performance of Planacon MCP-PMT photosensors under extreme working conditions. *Nucl. Instrum. Meth.*, A952:161689, 2020.
- [161] Heraeus Group. <https://www.heraeus.com/>. Accessed: 2020-04-22.
- [162] D. A. Finogeev. Fully integrated digital readout for the new Fast Interaction Trigger for the ALICE upgrade. *Nucl. Instrum. Meth.*, A952:161920, 2020.
- [163] A. Lehmann et al. Latest improvements of microchannel-plate PMTs. *Nucl. Instrum. Meth.*, A:162357, 2019.
- [164] A. Lehmann et al. Recent progress with microchannel-plate PMTs. *Nucl. Instrum. Meth.*, A952:161821, 2020.
- [165] M. Yu. Barnyakov and A. V. Mironov. Photocathode aging in MCP PMT. *JINST*, 6:C12026, 2011.
- [166] T. Jinno et al. Lifetime-Extended MCP-PMT. *Nucl. Instrum. Meth.*, A629:111–117, 2011, 1010.1057.
- [167] Yu. Melikyan. personal communication.
- [168] A. Britting, W. Eyrich, A. Lehmann, and F. Uhlig. Lifetime-issues of MCP-PMTs. *JINST*, 6:C10001, 2011.

- [169] Hamamatsu. *Photomultiplier tubes. Basics and applications*. Hamamatsu Photonics K. K., 3rd (3a) edition, 2007. Accessed: 2020-04-03.
- [170] PHOTONIS. *Photomultiplier tubes: Principle and Applications*. Photonis, 2002. Accessed: 2020-04-03.
- [171] Yu. A. Melikyan et al. Performance of the cost-effective Planacon[®] MCP-PMTs in strong magnetic fields. to be published, 2020.
- [172] PicoQuant PDL-800-B.
<https://www.picoquant.com/products/category/picoquant-pulsed-driver/pdl-800-b-picoquant-pulsed-diode-laser-driver#specification>. Accessed: 2020-02-28.
- [173] PicoQuant LDH-P-C-440M.
<https://www.picoquant.com/products/category/picoquant-pulsed-sources/ldh-series-picoquant-pulsed-diode-laser-heads#custom1>. Accessed: 2020-02-28.
- [174] E. Abbas et al. Performance of the ALICE VZERO system. *JINST*, 8:P10016, 2013, 1306.3130.
- [175] B. Abelev et al. Centrality determination of Pb-Pb collisions at $\sqrt{s_{NN}} = 2.76$ TeV with ALICE. *Phys. Rev.*, C88(4):044909, 2013, 1301.4361.
- [176] Varlen Grabski. New fiber read-out design for the large area scintillator detectors: providing good amplitude and time resolutions, 2019, 1909.01184.
- [177] V. Grabski. personal communication.
- [178] Eljen technology. general purpose ej-200, ej-204, ej-208, ej-212. <https://eljentechnology.com/products/plastic-scintillators/ej-200-ej-204-ej-208-ej-212>. Accessed: 2019-11-14.
- [179] BC-418, BC-420, BC422 Premium plastic scintillators.
<https://www.crystals.saint-gobain.com/sites/imdf.crystals.com/files/documents/bc418-420-422-data-sheet.pdf>. Accessed: 2019-11-27.
- [180] Photomultiplier tubes.
https://www.hamamatsu.com/resources/pdf/etd/PMT_TPMZ0002E.pdf. Accessed: 2019-11-22.
- [181] Kuraray. Plastic Scintillating Fibers.
https://www.kuraray.co.jp/uploads/5a717515df6f5/PR0150_psf01.pdf. Accessed: 2020-05-01.
- [182] R. Brun and F. Rademakers. ROOT: An object oriented data analysis framework. *Nucl. Instrum. Meth.*, A389:81–86, 1997.
- [183] Xin-Nian Wang and Miklos Gyulassy. HIJING: A Monte Carlo model for

- multiple jet production in pp, p–A and A–A collisions. *Phys. Rev.*, D44:3501–3516, 1991.
- [184] Zi-Wei Lin, Che Ming Ko, Bao-An Li, Bin Zhang, and Subrata Pal. A Multi-phase transport model for relativistic heavy ion collisions. *Phys. Rev.*, C72:064901, 2005, nucl-th/0411110.
- [185] Stefan Roesler, Ralph Engel, and Johannes Ranft. The Monte Carlo event generator DPMJET-III. In *Advanced Monte Carlo for radiation physics, particle transport simulation and applications. Proceedings, Conference, MC2000, Lisbon, Portugal, October 23-26, 2000*, pages 1033–1038, 2000, hep-ph/0012252.
- [186] R. Brun, F. Bruyant, M. Maire, A. C. McPherson, and P. Zancarini. *GEANT 3: user’s guide Geant 3.10, Geant 3.11; rev. version*. CERN, Geneva, 1987.
- [187] O2 software project for the ALICE experiment at CERN. <https://github.com/AliceO2Group/AliceO2>. Accessed: 2020-03-11.
- [188] Ananya et al. O²: A novel combined online and offline computing system for the ALICE Experiment after 2018. *J. Phys. Conf. Ser.*, 513:012037, 2014.
- [189] B. B. Back et al. The PHOBOS perspective on discoveries at RHIC. *Nucl. Phys.*, A757:28–101, 2005, nucl-ex/0410022.
- [190] K. Aamodt et al. Elliptic flow of charged particles in Pb-Pb collisions at 2.76 TeV. *Phys. Rev. Lett.*, 105:252302, 2010, 1011.3914.
- [191] B. Abelev et al. Long-range angular correlations of π , K and p in p-Pb collisions at $\sqrt{s_{NN}} = 5.02$ TeV. *Phys. Lett.*, B726:164–177, 2013, 1307.3237.
- [192] J. Adam et al. Anisotropic flow of charged particles in Pb-Pb collisions at $\sqrt{s_{NN}} = 5.02$ TeV. *Phys. Rev. Lett.*, 116(13):132302, 2016, 1602.01119.
- [193] Centrality dependence of the pseudorapidity density distribution for charged particles in Pb-Pb collisions at $\sqrt{s_{NN}} = 5.02$ TeV. <https://www.hepdata.net/record/78365>. Accessed: 2020-03-24.
- [194] J. Adam et al. Centrality dependence of the pseudorapidity density distribution for charged particles in Pb-Pb collisions at $\sqrt{s_{NN}} = 5.02$ TeV. *Phys. Lett.*, B772:567–577, 2017, 1612.08966.
- [195] Anisotropic flow of charged particles in Pb-Pb collisions at $\sqrt{s_{NN}} = 5.02$ TeV. <https://www.hepdata.net/record/72886>. Accessed: 2020-03-24.
- [196] Source of AliRoot QED generator. <https://github.com/alismw/AliRoot/blob/master/TEPEMGEN/AliGenQEDBg.h>. Accessed: 2020-03-11.